ROMA TRE
UNIVERSITÀ DEGLI STUDI

DEGREE OF DOCTOR OF PHILOSOPHY IN
CIVIL ENGINEERING

XXXI CYCLE

R-Funicularity: a new concept for evaluating the behavior of form-found shell structures

GIULIA TOMASELLO
Candidate

STEFANO GABRIELE
Advisor: Prof.

FABRIZIO PAOLACCI
Advisor: Prof.

GIANMARCO DE FELICE
Coordinator: Prof.

ii

Dedicated to my grandmother

Abstract

Shells have a structural behavior characterized by their curved geometry. They are generally designed pursuing criteria of structural efficiency and minimization of the employed material. Among efficient and optimized structural systems, funicular ones adopt the "right" shape in accordance with the applied load and are ideally able to resist external loads using membrane forces only, without introducing bending. To find the "right" shape, many form finding techniques have been developed and used by designers. However due to multiple design constraints, an ideal funicular behavior is sometimes impossible to achieve. When this is the case and bending moments cannot be avoided, a shell structure can still be considered "more or less funicular". In fact, a quantification of the funicularity may contribute to selection of the most appropriate and efficient shell shape.

This dissertation presents an effective and easy-to-read method to study and quantify the funicularity, named Relaxed Funicularity Ellipse Method. In order to formulate the new method, the classical funicularity concept has been extended and the definition of Relaxed Funicularity (R-Funicularity or RF) introduced. The parameter used to define the funicularity is the eccentricity and a structural shell is called R-Funicular when the eccentricity is included into an admissibility interval. The new method has been applied to structural shells obtained using a form finding approach, and analyzed under different static loads.

During the shell form finding process, gravity loads are considered, while the role of horizontal loading is ignored. Today shells with complex geometries are being designed and built, and are used to shelter people during extreme events such as earthquakes, but the dynamic behavior of civil thin shells has always been subjected to limited research.

In response to this issue, this dissertation investigates the effects of dynamic loading on the behavior of civil thin shells form-found under gravity loads. A two-phased methodology is presented. In the first phase a modal analysis of the shell is performed and the RF- Ellipse Method is applied to the modal stress distribution obtained to observe which modes show a more funicular behavior. In the second phase, the structure is analyzed performing a time-history analysis under multi frequencies spectrum defined using ad hoc functions based on the outputs of phase one.

The results of such a phased approach applied to benchmark studies, show that the frequency content of the different areas of the shell can give insights onto its membrane behavior. Moreover the form-found shell is analyzed under the action of the L'Aquila Earthquake (Italy, 2009) to prove how the methodology proposed can help to identify the vulnerable area of a shell form-found under gravity loading under a real seismic event.

Finally, to allow a quick and accessible application of the RF-Ellipse Method, and consequently of the proposed two-phased methodology, a new Matlab-based software named r-Fun integrated with a Finite Element analysis package has been implemented.

Acknowledgments

This dissertation would not have seen its final form without the support of many.

First of all, I would like to thank my advisor, Prof. Stefano Gabriele, for guiding my research with patience, knowledge, and contagious enthusiasm. I appreciated the freedom he gave me to pursue my interests and I would like to express my gratitude because over the past three years he has been not only my guide, but also my friend. I never took for granted the opportunity to work with him.

I am also grateful to my second advisor, Prof. Fabrizio Paolacci, for his precious help and comments along the way. I am grateful to Prof. Gianmarco De Felice, coordinator of the PhD programme, and to the Department of Civil Engineering at Roma Tre University.

A great number of people, professors and fellow graduate students contributed to my Roma Tre experience offering their advice and help. Especially I would like to thank Prof. Valerio Varano, for his fundamental contribution in developing the new Relaxed Funicularity Ellipse Method and for introducing me to the concepts of differential geometry. I am also grateful to Gianluca Acunzo for his invaluable contribution in implementing the software r-Fun and for reminding me how teamwork can be both fun and productive.

I am truly grateful to Prof. Sigrid Adriaenssen. It has been a privilege to collaborate with her through this 3-year journey. I would like to thank her for our many conversations on my research and for her precious suggestions. I am thankful to her for hosting and guiding me as a VSRC at Princeton University. All the Form Finding Lab colleagues helped me in their own way and made my experience extraordinary in the United States. Especially I would like to acknowledge Dr. Tim Michiels for the discussion about the funicularity and the dynamic behavior of shell structures, and for his famous Spritz.

I would like to thank Prof. John Ochsendorf and, again, Prof. Sigrid Adriaenssen who have accepted to review this dissertation providing their extremely valuable feedback.

I am grateful to Ross Harvey, Technical Director at WSP. He has been my mentor during the years spent in London before starting my PhD. The practical experience I gained there has been extremely helpful to contextualize and sharpen my research. I am thankful to him for reading my papers and my dissertation. He provided his opinion and reviewed my English, even when the British spelling gave way to the American one.

Furthermore, my deepest gratitude goes to my parents, my brother and my family. They always encourage me to pursue my aspirations and support me in everything I do.

Thanks to my closest friends, the ones in Rome and the ones scattered around the world. They are my second family and are always ready to listen and make me smile.

Finally, I want to thank Diego for the unique life we are building together. Part of this work has been done on the dozens of flights between Rome and Asmara. We have been often apart, but I can always count on his love and endless support.

Contents

List of Figures

List of Tables

Symbols and abbreviations

Below a list of the frequent symbols:

R Radius of curvature

k Curvature

K Gaussian curvature

H Mean curvature

h Thickness

E Young's Modulus

ν Poisson's Ratio

ρ Density

e Eccentricity

λ Admissibility coefficient

q Force density

$N_{\mathbf{x}}, N_{\mathbf{y}}$ Normal forces

$N_{\mathbf{xy}}, N_{\mathbf{yx}}$ Tangential forces

$M_{\mathbf{x}}, M_{\mathbf{y}}$ Bending moments

$M_{\mathbf{xy}}, M_{\mathbf{yx}}$ Twisting moments

$Q_{\mathbf{x}}, Q_{\mathbf{y}}$ Normal shear-stress resultants

$\sigma_{\mathbf{x}}, \sigma_{\mathbf{y}}$ Normal stresses

$\tau_{\mathbf{xy}}, \tau_{\mathbf{yx}}, \tau_{\mathbf{xz}}, \tau_{\mathbf{yz}}$ Tangential stresses

x Scalar

$\mathbf{x}$ Vector

$\mathbf{X}$ Matrix

$\mathbf{C}$ Branch-node matrix

$Sph(\mathbf{X})$ Matrix spherical component

$Dev(\mathbf{X})$ Matrix deviatoric component

$Tr(\mathbf{X})$ Matrix trace

$\mathbf{I}$ Identity matrix

∇ Nabla

f Frequency

ω Angular frequency

Φ_j Modal vector

Below a list of the frequent acronyms:

API Application Programming Interface

CAD Computer aided design

DR Dynamic relaxation

FFT Fast Fourier Transform

FD Finite Difference

FE Finite Element

GUI Graphical User Interface

FDM Force density method

LFDM Linear Force density method

NLFDM Non Linear Force density method

MAC Modal Assurance Criterion

NURBS Non-Uniform Rational Basis Splines

PS Particle-spring method

RF Relaxed Funicular or Funicularity

TNA Thrust network analysis

Chapter 1

Introduction

The first chapter introduces the core topic and contextualizes the study. Section 1.1 illustrates the motivations of this research through a critical review of the design approach intended as a combination of architectural and engineering principles. Section 1.2 identifies the significance of the research formulating the objectives of the presented study. Section 1.3 is devoted to outline how the dissertation is structured. Finally, the journal and conference papers in which portions of this dissertation have appeared are listed in Section 1.4.

1.1 Motivation

Traditionally, says Peter Rice (1935-1992), structural engineers are expected to play the role of Shakespeare's Iago, who undermined the love of Othello and Desdemona by reducing to reason their every unreasonable act or feeling. In terms of building, this means the engineer is seen to reduce every unreasonable and soaring idea an architect might have. However the engineer's true role is not to reduce, but to explore structures [38, 92].

When designing a structure, different solutions may be explored trying to combine multiple disciplines and knowledge since the early stages of a project. Architecture and structural engineering can merge to conceive a work that meets criteria of aesthetics, architectural program, economy, buildability, and last but not least, structural efficiency. No more famous slogan is appropriate for the essential components of designing values than the words of the Roman architect and engineer Vitruvius (ca. 80-15 BC) "*Firmitas, Utilitas et Venustas*", that may be translated to "*Strength, Utility and Beauty*" [109].

Sometimes the structural principles of a work of architecture may even contribute to the aesthetics, making buildings, and structures in general, more elegant. Referring to a structure, the term elegant often implies a simple and direct handling of the forces, a logic inherent in the load path [91]. This approach leads to a minimum use of material and, sometimes, to a structural system that is easy to read.

Pursuing criteria of structural efficiency and elegance, the designer is invited to consider the inherent interrelation of form and structure, perfectly expressed by the words of Eladio Dieste (1917-2000):

> "The resistant virtues of the structures that we seek depend on their form; it is through their form that they are stable, not because of an awkward accumulation of material. There is nothing more noble and elegant from an intellectual viewpoint than this: to resist through form." (Dieste, 1996) [85]

Since their shape directly derives from their flow of forces defining their behavior, shell structures play a special role for designers. They represent a perfect example of structures

that may be conceived equally combining architectural and engineering principles. Jörg Schlaich goes as far as to state that:

> "The more the form of a building or structure develops from its flow of forces, the more it is under the responsibility of the engineer." (J. Schlaich, 2014) [1]

Nowadays shells with complex geometries are being designed and built. Software and technological development allows us to conceive more and more bold shapes with the aim to create eye-catching structures. However principles of efficiency and economy should always be respected. Underlying this belief, there are two main motivations. The first one refers directly to Dieste's quote and to the work of many famous designers such as Pier Luigi Nervi (1891-1979) or Eduardo Torroja (1899-1961), who saw in the economy principle a way to reach a result that is aesthetically pleasing. Nervi states that, together with stability and functionality, economy is a fundamental requirement of every work of architecture [78] and affirms:

> "In a broad sense related to the final purpose of the project, economy is almost always - not seem too bold statement - reason for aesthetic success." (Nervi, 1945) [78]

The second motivation is related to today's awareness of the anthropogenic impact on the environment. The construction industry is largely responsible for Carbon dioxide (CO_2) emissions [49]. This aspect not only involves the *operational* carbon due to the building use phase, but also the *embodied* carbon, due to material quantities, transport to site, construction, and demolition [29, 30]. There is an urgent need to reduce the latter in order to avoid extreme climate disruptions. Hence innovative structural design needs to play a role targeting efficient structural behavior and reduction of construction materials.

When designing shell structures, efficiency can be accomplished by aiming toward a funicular behavior where bending moments are minimized and a maximum exploitation of the material is guaranteed.

The word *funicular* originates from the Latin word "*funiculus*" meaning "rope, cord". In fact a hanging inelastic rope under self-weight is a specific funicular shape known as catenary. Shapes are defined funicular if the external loads are sustained only by membrane stresses (tension or compression). Many different techniques, named form finding methods, have been developed to find funicular surface geometries and are extensively employed by designers. However a shell behaves as fully funicular only under strict conditions that cannot always be guaranteed when designing and constructing a shell structure. As a result bending moments, even if minimal, arise and quantifying the degree of funicularity becomes fundamental to select the most appropriate shape to adopt.

An evaluation of the funicularity may help to assess the structural performance of shells under the acting loads. These can be classified between gravitational and horizontal loads. Among the possible horizontal actions that need to be considered, seismic loading takes on great relevance.

Earthquakes represent catastrophic events that may cause failures of built structures and consequent fatalities. Shells are constructed in many seismic regions and are often used to shelter people during these extreme events [97]. Hence a deeper understanding of their dynamic and seismic response that leads to design safe, cost-effective and environmentally friendly structures is crucial.

1.2 Significance of research

The current study aims to present a new method to evaluate to what extent a shell responds with a funicular stress state to external loads. This method, named Relaxed Funicularity

Ellipse Method, broadens the classical funicularity concept using a generalized definition of the eccentricity. It defines a shell as Relaxed Funicular (R-Funicular) when its behavior is not ideally funicular but is characterized by a contribution of the bending moments much smaller than the one given by the membrane forces. The goal is to help designers to select the most appropriate shape to adopt when conceiving a shell surface.

Moreover, the proposed method is applied to investigate the effects of dynamic loading on the behavior of civil form-found shells. In order to help designers to identify the vulnerable area of a shell structure under the action of a seismic event, a new two-phased methodology is presented.

Finally, in order to allow a quick and accessible application of the Relaxed Funicularity Ellipse Method, and consequently of the proposed two-phased methodology, a new Matlab-based software named r-Fun integrated with a Finite Element analysis package has been implemented.

Summarizing, the specific research objectives are listed below:

- Quantify the funicularity of shell structures providing insights into the structural efficiency of the selected shape;

- Investigate the structural performance of form-found shell structures under the action of vertical and horizontal loads;

- Study the dynamic behavior of shell structures form-found under self-weight to obtain an improved performance not only under gravity loading but also under dynamic loading.

1.3 Outline

This dissertation is organized into eight chapters. The first one introduces the core topic of the dissertation explaining the motivation and the significance of the research. In order to provide a detailed overview of the overall contents and structure of this study, the following chapters are introduced as follows.

Chapter 2: Shell structures

This chapter presents key concepts related to the design of shell structures. Since they are characterized by a strong relationship with space geometry, in order to better understand their structural behavior, basic notions of differential geometry are given in Section 2.2. The theory of shell structures is then discussed in Section 2.3 distinguishing between membrane and bending theories. Section 2.4 is devoted to an overview of roof shell structures designed and constructed during the years.

Chapter 3: Funicularity and form finding

In this chapter the concept of funicularity and the form finding techniques developed during the years to achieve a "funicular" structural geometry are presented. The historical development of the concept of funicularity is reviewed in Section 3.1. An overview and classification of the form finding methods are given in Section 3.2, distinguishing between physical models, graphic and numerical methods, and digital tools available nowadays. A brief definition of structural optimization, to differentiate it from form finding, is given in Section 3.3. Section 3.4 is devoted to the presentation of the numerical form finding technique known as Force density method that has been implemented by the author in the numerical computing environment and proprietary programming language Matlab.

Chapter 4: Musmeci and the Basento bridge

This chapter presents the Italian engineer Sergio Musmeci, his design philosophy and his work. Musmeci is noteworthy for his ability to design continuous shells with unprecedented shapes well ahead of his time. His goal was trying to minimize the shell area while maximizing the structural behavior. Musmeci's most famous project is the bridge over the Basento river. Section 4.1 investigates Musmeci's education and experience, leading to the project of the bridge. Section 4.2 reviews the design steps of the Basento bridge and discusses the different modeling and testing techniques adopted by Musmeci. Section 4.3 revisits the shape generation of the surface structure using resources available nowadays and applying the Force density method as form finding technique. Finally the form-found shape is validated with the support of a Finite Element model.

Chapter 5: Relaxed Funicularity Ellipse Method

This chapter presents a new method to study and quantify the funicularity. Funicular systems adopt the "right" shape in accordance with the applied load and are ideally able to act without introducing bending. As a result their thickness can be minimized and the amount of material reduced. However an ideal funicular behavior is sometimes impossible to achieve due to multiple design constraints. When this is the case and bending moments cannot be avoided, a shell can still be considered "more or less funicular". In fact in term of stresses and structural performance, there is a substantial difference if the bending moments give a contribution much smaller than that of the membrane forces or if the two contributions are comparable. This topic is extensively discussed in Section 5.1. Section 5.2 presents the new method, know as Relaxed Funicularity Ellipse Method, that extends the classical funicularity concept to the one of Relaxed Funicularity generalizing the definition of eccentricity. The rationale of the method proposed, together with the mathematical formulation and a proper graphical representation, is discussed. The method has been applied to form-found shell structures analyzed under different static loads. In Section 5.3 the form finding approach and the numerical model used are detailed. Section 5.4 is devoted to the discussion of the parametric numerical study and the observed results.

Chapter 6: Dynamic behavior of form-found shells

During the shell form finding process, gravity loads are generally considered, while the role of horizontal loading is ignored. Today civil shell structures with complex geometries are being designed and built, and are used to shelter people during extreme events such as earthquakes, but their dynamic behavior has always been subjected to limited research. In this chapter, a two-phased methodology to investigate the effects of dynamic loading on the behavior of civil thin shells form-found under gravity loads is proposed. The methodology applies the Relaxed Funicularity Ellipse Method to introduce the concepts of Modal and Dynamic Funicularities. A literature overview on the dynamic behavior of shell structures is presented in Section 6.1. The rationale of the methodology proposed is illustrated in Section 6.2. In Section 6.3 the form-found and numerical models used are detailed. Section 6.4 is dedicated to the presentation of the results obtained applying the methodology to two different form-found shell structures. Moreover one of the two shells is analyzed under the action of a real seismic event.

Chapter 7: r-Fun

The Relaxed Funicularity Ellipse Method has been implemented in a Matlab-based software environment integrated with a Finite Element analysis package. The proposed software is named r-Fun and presented in this chapter. The system environment and architecture

are presented in Section 7.1. Section 7.2 shows the results obtained applying r-Fun to a form-found shell.

Chapter 8: Conclusions

The final chapter intends to draw conclusions. Section 8.1 summarizes the key contributions of the study undertaken in this dissertation. Section 8.2 is devoted to analyze the limitations of the developed approaches and presents directions for future work.

1.4 Publications

Sections of this dissertation have appeared in the peer-reviewed journal and conference papers listed below:

- Adriaenssens S., Gabriele S., Varano V., Tomasello G., Magrone P., Revisiting the form finding techniques of Sergio Musmeci: the bridge over the Basento river, in ICSA2016 Portugal, Structures and Architecture Beyond their limits, Taylor&Francis Group, London, 2016.

- Gabriele S., Adriaenssens S., Varano V., Tomasello G., Alfonsi D., Modal Funicularity of form-found shell structures, in Proceedings of the International Association for Shell and Spatial Structures (IASS) symposium 2017: Interfaces, Hamburg, Germany, September 25-28, 2017.

- Gabriele S., Varano V., Tomasello G., Alfonsi D., R-Funicularity of form-found shell structures, Engineering Structures, 157, 157-169, 2018.

- Tomasello G., Gabriele S., Adriaenssens S., R-Funicularity of shell structures under dynamic load: the influence of the shape, in Proceedings of the International Association for Shell and Spatial Structures (IASS) symposium 2018: Creativity in Structural Design, MIT, Boston, USA, July 16-20, 2018.

- Tomasello G., Gabriele S., Adriaenssens S., Dynamic behavior of form-found shell structures according to Modal and Dynamic Funicularity, Submitted, 2018.

These sections have been extended and edited for continuity. They are included with permission of the other authors.

Chapter 2

Shell structures

Shell structures find a multitude of applications in different branches of engineering (civil, mechanical, aeronautical, etc.). Since they are characterized by a strong relationship with space geometry, the basic concepts of differential geometry are given in Section 2.2. The theory of shell structures is then discussed in Section 2.3, while Section 2.4 is devoted to a brief overview of shell design during the years.

2.1 What is a shell?

The dictionary states that the word *shell* indicates the thin hard outer case of a mollusc or a crustacean, of an animal's egg or a tortoise (Fig. 2.1). The same term is largely used in the engineering world to refer to man-made structures described by three-dimensional (3D) curved surfaces that, as in the previous definition, can be considered *thin*, in fact one dimension is significantly smaller compared to the other two, and *hard*, in fact a relatively rigidity is implied. Specifically, a shell can be classified as a thin shell if the thickness is less than 1/20 of the span.

A shell is defined as a form-passive structure, because its shape does not adjust under different loading conditions, unlike a cable or a net that are form-active structures [1]. A shell is characterized by two fundamental aspects: structural *continuity*, in the sense that it can transmit forces in different directions along its surface (even if composed of separate elements), and *curvature*. A shell might be curved in one direction, as a cylinder, or in two directions as a dome.

Figure 2.1: Shell structures commonly found in nature [Images in the public domain]

As a beam is represented by a line, a shell is modeled as a surface of zero thickness. The mechanics of shell structures and the theory that describes their structural behavior is, in principle, similar to the one used to describe other kind of structures such as beams or arches, but it is complicated by the geometrical aspects related to curved surfaces. As any other

structure, shells carry external loadings using membrane forces (compression or tension) and bending moments, but while in the theory of beams there is virtually no interaction between bending and stretching actions, this aspect is crucial in the theory of shells [14].

2.2   Geometry of curved surfaces

A shell is characterized by its curvature, just as its behavior is dominated by the geometry of the shell surface. The geometric properties of curved surfaces are studied by the differential geometry.

The differential geometry of curves and surfaces developed from mathematicians of the 18th and 19th centuries. Principal contributors were Euler (1707-1783), Monge (1746-1818), Gauss (1777-1855) and Riemann (1826-1866).

A surface may be defined as the boundary between two distinct regions of 3D Euclidean space [14]. According to Gauss [36], a curved surface can be described as a 3D object or as a two-dimensional (2D) object. In fact the position of any point on a surface can be specified by two coordinates, as shown in Figure 2.2. A surface in the Euclidean space $\mathbb{R}^3$ which is defined by a parametric equation with two parameters $f : \mathbb{R}^2 \to \mathbb{R}^3$ is defined *parametric surface* [25].
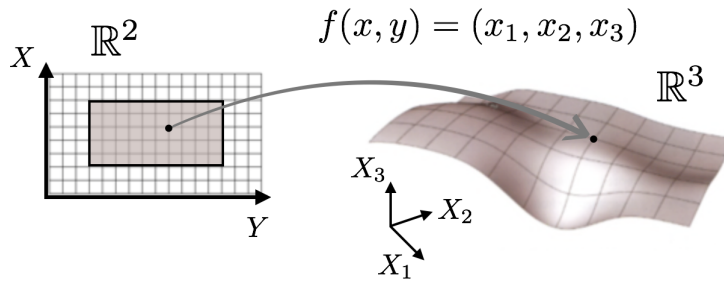
Figure 2.2: Parametric surface

A surface can have *local* and *global* properties. The first ones are the properties that hold in a small neighborhood of a surface point, such as the curvature. The second ones affect the overall surface, such as holes or boundaries. The properties of a surface can be also classified as *intrinsic*, which depend only on measurements of surface length, or *extrinsic*, which involve measurements in the 3D space. The Gaussian curvature is an intrinsic property, while the normal to a surface in a given point is an extrinsic property.

Some of the key concepts of differential geometry are summarized in this section. The discussion is more qualitative than rigorous. For a full discussion please refer to [14, 39, 82].

2.2.1   Plane curves

In order to study a surface and its properties, it is important to start from the notion of plane curve. Given a smooth curve Γ in a plane, as the one shown in Figure 2.3a, a point A and the osculating circle of the curve at the point can be drawn. The length of the segment normal to the surface connecting A to the center of curvature 0 is defined *radius of curvature R*. The inverse to the radius of curvature is defined *curvature k*.

Taking a section γ of the plane curve Γ (Fig. 2.3b), two points A and B can be located using the coordinate s. The distance ds between the two points approaches zero and the angle
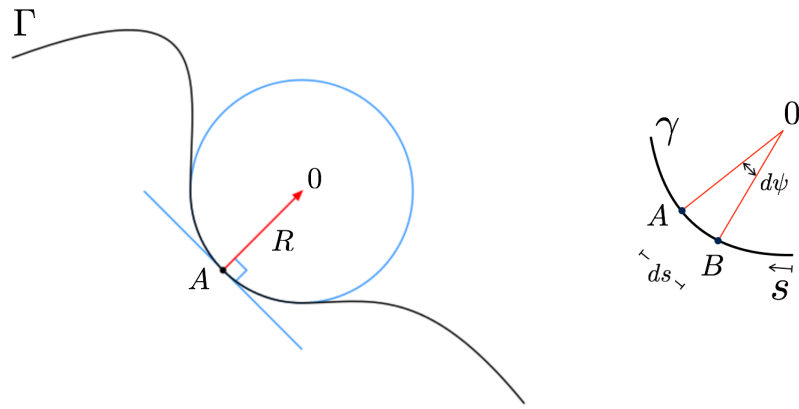
(a) *Osculating circle (blue) of the curve Γ at the point A*   (b) *Section γ of the curve Γ*

Figure 2.3: Plane curve Γ with center of curvature 0 and radius of curvature R, arc-length coordinate s and angle ψ

between the radii of curvature of the two point is defined $d\psi$. At this point the curvature can be defined as follows:

$$R = \frac{ds}{d\psi} \rightarrow k = \frac{1}{R} \tag{2.1}$$

As drawn in Figure 2.4, a coordinate z can be defined perpendicular to s in order to designate a positive and negative side. The curvature is positive when the radius of curvature (R) lies on the negative z side of Γ and positive when the radius of curvature (R') lies on the negative z side of Γ.
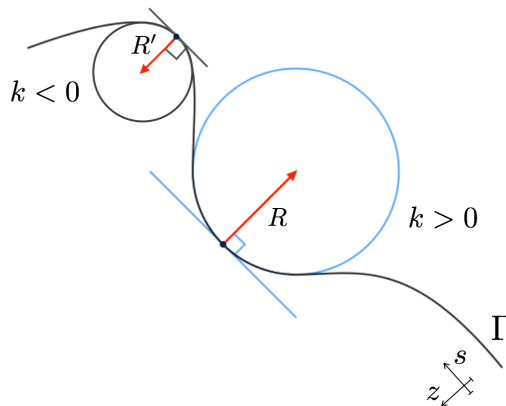
Figure 2.4: Plane curve Γ with positive and negative curvature k

The curvature value varies along the curve Γ changing from positive to negative. Hence there is a point where the curvature is equal to zero and the osculating circle becomes a straight line.

2.2.2   Surfaces

A smooth surface, continuous and without discontinuities, is represented in Figure 2.5. While for the plane curve only one radius of curvature is defined, for a surface two radii of curvature are defined.
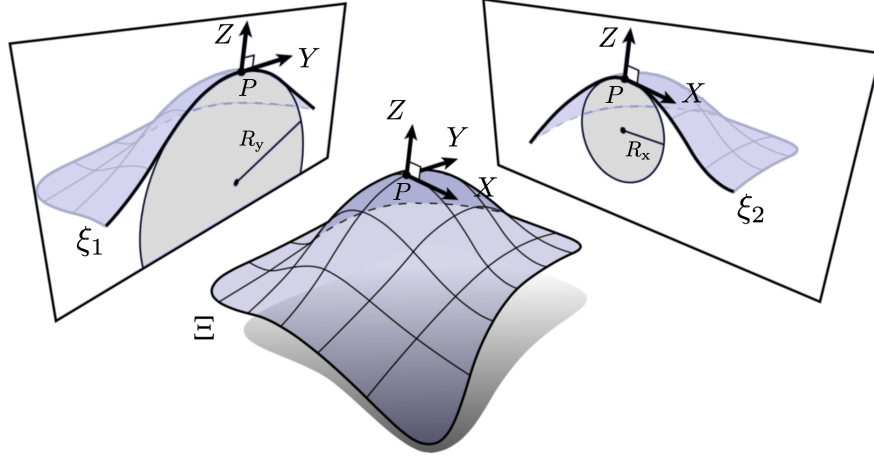
Figure 2.5: Surface Ξ with radii of curvature R_x and R_y [25]

Located a point P on the surface Ξ, a local Cartesian coordinate system has been set up. The plane XY is tangential to Ξ at the point P and the Z axis is defined perpendicular to the plane. The X and Y axes may be rotated about Z and two planes, XZ and YZ respectively, can be defined for every direction. Drawing an osculating circle in each vertical plane, the corresponding radius of curvature R and curvature k can be defined. The sign convention for the curvature is equal to the one taken for the plane curve.

At each point on the given surface, a minimum and a maximum radius of curvature can be found. These two radii of curvature are defined principal radii of curvature and the corresponding curvatures are defined *principal curvatures* k_1 and k_2. The directions in the normal planes where the curvature takes its maximum and minimum values are called *principal directions* and are always perpendicular. A spherical surface represents a special case where all directions are principal directions.

The *Gaussian curvature* K of the surface at the considered point is the product of the two principal curvatures: $K = k_1 k_2$. The Gaussian curvature is positive if the principal curvatures are of the same sign and negative if they are of opposite sign. Examples of surfaces with zero, positive and negative Gaussian curvature are given in Figure 2.6. As anticipated at the beginning of Section 2.2, K is an intrinsic property of the surface because does not change when inextensional deformations of the surface occur (even if k_1 and k_2 change). A deformation is defined inextensional when the surface is bent preserving unchanged the length of each line element.

The *mean curvature* H of the surface at the considered point is equal to half of the sum of the two principal curvature: $H = \frac{k_1 + k_2}{2}$. Surfaces with zero mean curvature are called *minimal surfaces* because they minimize surface area.

2.3   Theory of shell structures

As stated in Section 2.1, the behavior of a shell is highly influenced by its geometry. This key aspect can be better understood observing the following. In the mechanics of solids,
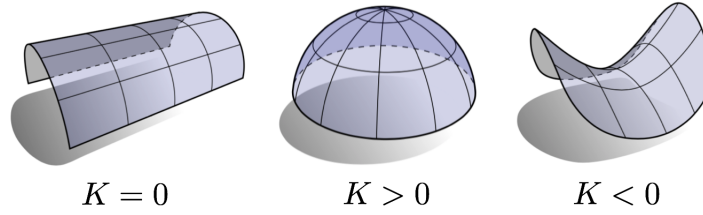
Figure 2.6: Surfaces with zero, positive and negative Gaussian curvature [25]

three sets of differential equations (equilibrium, compatibility and constitutive), together with the boundary conditions, describe mathematically the problem. The character of this mathematical formulation is sometimes determined by the form of the material properties, hence by the constitutive equations. As a consequence, while the governing equations for an elastic material are always elliptic, if we move to the theory of plasticity they can be hyperbolic. However in the theory of shells, the governing differential equations can be hyperbolic as a direct consequence of geometrical properties [14].

In Figure 2.7, a typical shell element in a Cartesian coordinate system is shown. The directions X and Y are principal directions and the corresponding curvatures are represented by $1/R_x$ and $1/R_y$ respectively. The shell thickness is equal to h. The stress resultants can be divided between normal and tangential forces $(N_x, N_y, N_{xy}, N_{yx})$, bending and twisting moments $(M_x, M_y, M_{xy}, M_{yx})$ and normal shear-stress resultants (Q_x, Q_y).
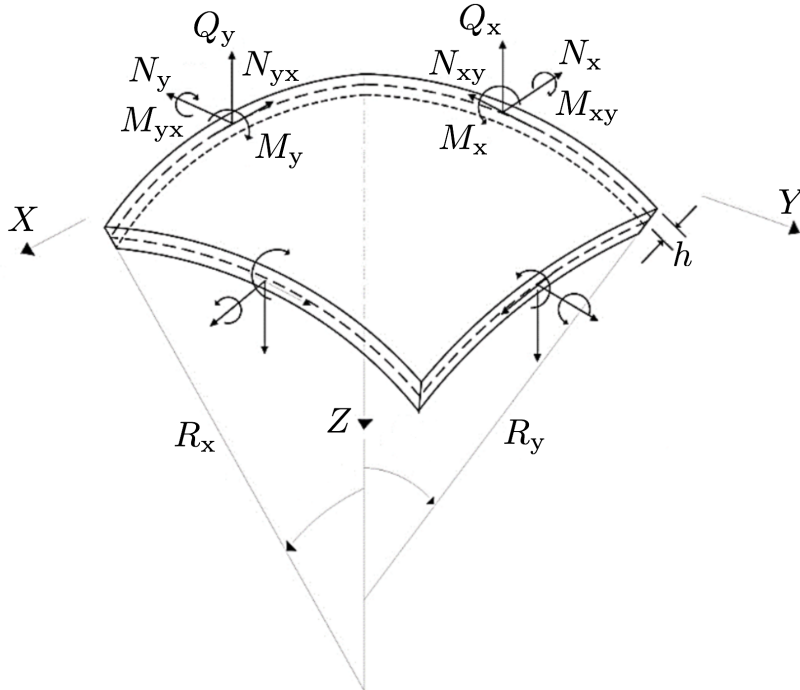
Figure 2.7: Stress resultants of a shell element in a Cartesian coordinate system X, Y, Z

The stress resultants can be written as follows, integrating the normal and tangential

stresses $(\sigma_x, \sigma_y, \tau_{xy}, \tau_{yx}, \tau_{xz}, \tau_{yz})$ through the shell thickness:

$$N_x = \int_{-h/2}^{+h/2} \sigma_x (1 - \frac{z}{R_y}) dz \qquad\qquad N_y = \int_{-h/2}^{+h/2} \sigma_y (1 - \frac{z}{R_x}) dz \qquad (2.2)$$

$$N_{xy} = \int_{-h/2}^{+h/2} \tau_{xy} (1 - \frac{z}{R_y}) dz \qquad\qquad N_{yx} = \int_{-h/2}^{+h/2} \tau_{yx} (1 - \frac{z}{R_x}) dz \qquad (2.3)$$

$$Q_x = \int_{-h/2}^{+h/2} \tau_{xz} (1 - \frac{z}{R_y}) dz \qquad\qquad Q_y = \int_{-h/2}^{+h/2} \tau_{yz} (1 - \frac{z}{R_x}) dz \qquad (2.4)$$

$$M_x = \int_{-h/2}^{+h/2} \sigma_x z (1 - \frac{z}{R_y}) dz \qquad\qquad M_y = \int_{-h/2}^{+h/2} \sigma_y z (1 - \frac{z}{R_x}) dz \qquad (2.5)$$

$$M_{xy} = -\int_{-h/2}^{+h/2} \tau_{xy} z (1 - \frac{z}{R_y}) dz \qquad\qquad M_{yx} = \int_{-h/2}^{+h/2} \tau_{yx} z (1 - \frac{z}{R_x}) dz \qquad (2.6)$$

Since $\tau_{xy} = \tau_{yx}$, we have $N_{xy} = N_{yx}$ and $M_{xy} = M_{yx}$. The stress resultants are obtained respecting the following hypothesis:

- the displacements of the shell are small enough to set up the equilibrium equations for the undistorted configuration;

- the material is linear-elastic;

- the normal to the average surface plane sections remain plane and those are still normal to the deformed average surface;

- the shearing deformations are negligible.

The aim of this section is to summarize the basic concepts of the theory of shells which are fundamental to understanding the key aspects of the thesis. It is not intended to be exhaustive. For a more detailed discussion of this complicated topic please refer to [7, 14, 39].

2.3.1   Membrane theory

If twisting and bending moments are small enough to be negligible and the load is considered to be carried by the stretching actions, the shell can be analyzed uniquely following the membrane theory. In other words, the shell is considered to possess in-plane stiffness and zero flexural stiffness. The in-plane stiffness can be defined as follows:

$$D_{in-plane} = \frac{Eh}{1 - \nu^2} \qquad (2.7)$$

where E is the Young's Modulus and ν the Poisson's Ratio.

Looking at Figure 2.8, a small shell element under the action of normal (p) and tangential (q_x, q_y) loading is shown, where $M_x, M_y, M_{xy}, Q_x, Q_y$ are set equal to zero throughout the shell. The limit $dx, dy \to 0$ is set.

Unlike the full formulation, in the membrane theory the equilibrium equations are reduced to three [14]:

$$\frac{\delta N_x}{\delta x} + \frac{\delta N_{xy}}{\delta y} = -q_x \qquad (2.8)$$

$$\frac{\delta N_y}{\delta y} + \frac{\delta N_{xy}}{\delta x} = -q_y \qquad (2.9)$$

$$\frac{N_x}{R_x} + \frac{N_y}{R_y} = p \qquad (2.10)$$

(a) *Shell element*   (b) *View normal to the shell element*
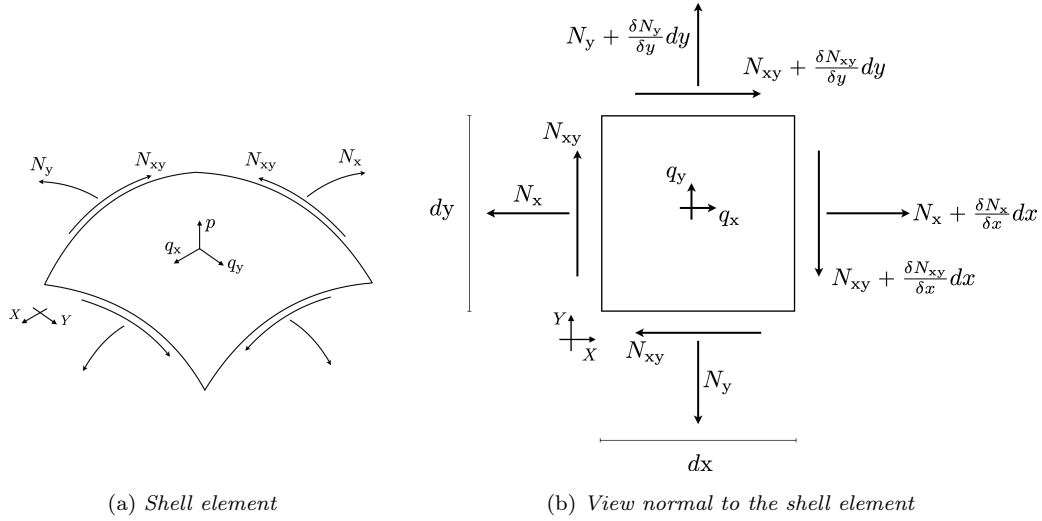
Figure 2.8: Membrane theory - Stress resultants

As it would be for a plane element, computing the tangential equilibrium, the differential Equations (2.8) and (2.9) are obtained. The normal equilibrium is expressed by Equation (2.10) that depends on the curvature values, hence it is influenced by the shell geometrical form.

In principle with three equations in three unknown stress resultants, the shell should be statically determinate. However the solution depends strictly upon the shape of the shell surface and the nature of the boundary conditions [1, 14]. If a shell has the wrong shape or the wrong boundary conditions, it may become a mechanism rather than a true structure to which the membrane theory can be applied.

It is worth mentioning that sometimes, even if the shell has the appropriate shape and boundary conditions, membrane theory is not applicable because bending stiffness is necessary. In fact if compressive stresses occur in the shell, bending stiffness is fundamental to avoid buckling and prevent any consequent sudden collapse [1].

2.3.2 Bending theory

In certain circumstances bending effects cannot be neglected as they sustain a substantial portion of the applied loads. A more general formulation needs to be considered where the shell is able to carry the loading by both stretching and bending effects. The flexural stiffness or rigidity is not zero, but can be calculated as:

$$D_{flexural} = \frac{Eh^3}{12(1 - \nu^2)} \tag{2.11}$$

Applying the bending theory, the stress resultants acting on a small shell element are shown in Figure 2.9. As in Figure 2.8, small differences in the values acting on opposite edges are taken into account. For the sake of brevity, the increased variables have been labelled using the symbol + as superscript. The limit $dx, dy \to 0$ is set.
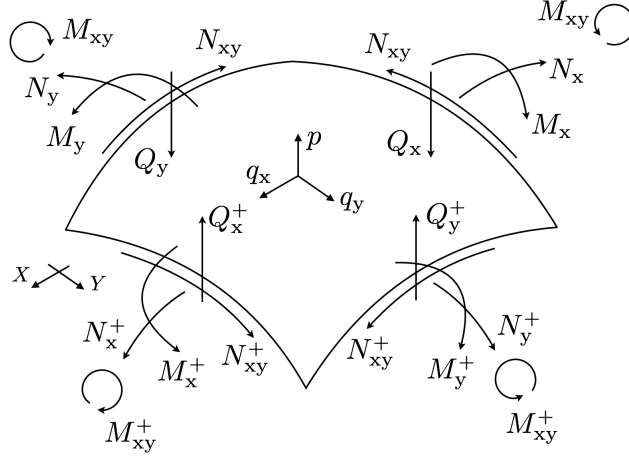
Figure 2.9: Bending theory - Stress resultants

The equilibrium equations are now five [14]:

$$\frac{\delta N_x}{\delta x} + \frac{\delta N_{xy}}{\delta y} + \frac{Q_x}{R_x} = -q_x \tag{2.12}$$

$$\frac{\delta N_y}{\delta y} + \frac{\delta N_{xy}}{\delta x} + \frac{Q_y}{R_y} = -q_y \tag{2.13}$$

$$\frac{N_x}{R_x} + \frac{N_y}{R_y} - \frac{\delta Q_x}{\delta_x} - \frac{\delta Q_y}{\delta_y} = p \tag{2.14}$$

$$Q_x - \frac{\delta M_x}{\delta x} - \frac{\delta M_{xy}}{\delta y} = 0 \tag{2.15}$$

$$Q_y - \frac{\delta M_y}{\delta y} - \frac{\delta M_{xy}}{\delta x} = 0 \tag{2.16}$$

$$\tag{2.17}$$

Combined with the compatibility and constitutive equations, the equilibrium equations define the problem of a shell subjected to stretching and bending effects allowing to calculate stress resultants and deflections of the shell surface.

2.4   Design of roof shell structures

Shells can be designed and constructed as continuous surfaces or from discrete elements following the shell surface. In the last case they are usually defined *gridshells*.

According to their geometry, shells can be classified in three groups [1]:

- *freeform* or *sculptural* shells are generated without taking into consideration structural performance (Fig. 2.10a);

- *mathematical* shells are described by analytical functions, such as lower degree polynomials or trigonometric or hyperbolic functions (Fig. 2.10b);

- *form-found* shells are generated through the use of form finding methods (Refer to Chapter 3) exploring states of static equilibrium (Fig. 2.10c).

(a) *Freeform: Bosjes Chapel by Steyn Studio (South Africa, 2016) [PC: Adam Letch]*

(b) *Mathematical: Los Manantiales by Félix Candela (Mexico City, 1958) [via archdaily.com]*

(c) *Form-found: Open Air Theatre in Grötzingen by Heinz Isler (Germany, 1977) [PC: John Chilton]*

Figure 2.10: Classification of shell geometries

These three classes of shell shapes are generated following different approaches. Freeform and mathematical shells are conceived without considering any specific stress state, so they may resist external loadings with a combination of membrane forces and bending moments. In a different way, form-found shells demand a structurally-informed design process that tries to guarantee primarily a membrane behavior.

2.4.1   History of design of roof shells

In the field of civil engineering, shell structures are widely used to build roofs and coverings of large spans without the application of intermediate supports. Early examples of roof shells date back to Egyptian, Assyrian, and Roman time, when arched and vaulted structures were erected using materials as masonry or rudimentary types of concrete.

The Pantheon, built in Rome during the reign of Hadrian between 118 and 125 AD, and the Basilica of Hagia Sophia, built in Istanbul in 537 AD at the beginning of the Middle Ages, are spectacular examples of shell structures that can still be visited (Fig. 2.11). The domes

(a) *Pantheon (Rome, 118-125 AD)*   (b) *Basilica of Hagia Sophia (Istanbul, 537 AD)*

Figure 2.11: Early examples of shell structures [Images in the public domain]

and vaults built during antiquity and Middle Ages were usually thick (thickness to span ratio greater than 1/20, hence the assumption of negligible shearing deformations is not applicable) and could mainly resist compressive loads. More recently, thinner shell structures have been developed.

In the late 19th and early 20th centuries, exceptional masonry shells were designed and built by the Guastavino Company [80]. By adapting a traditional Mediterranean method of constructing vaults to the American construction market, Rafael Guastavino Sr. (1842-1908) and Jr. (1872-1950) realized remarkable examples of structural masonry roofs (Fig. 2.12).

In the 20th century, also the Uruguayan engineer and architect Eladio Dieste became well-known for the design of elegant structures applying the technique of reinforced masonry. Dieste was able to achieve efficient vaults through the form of the structure and the using of ordinary reinforcing bars between the brick rows [4]. An example of Dieste's work is shown in Figure 2.13, where the double-cantilever vaults of the municipal bus terminal in Salto, Uruguay are represented [79].

Masonry materials such as bricks or stones are strong in compression and weak in tension. Hence the development of reinforced concrete, a moldable material with both compressive and tensile strength, marked the beginning of a new era of construction of thin roof shells.

Figure 2.12: Guastavino Room in the Boston Public Library by Rafael Guastavino (Boston, 1895) [PC: Author]

The years between 1920s and early 1960s have been considered the golden age of concrete shell construction [68]. According to Billington [7], the modern era of thin concrete shells starts in 1922 with the dome of the Zeiss-Planetarium in Jena, Germany designed by the German engineer Walther Bauersfeld (1879-1959) (Fig. 2.14).

Modern shells were designed later by architects and engineers such as Eugène Freyssinet (1879-1962), Pier Luigi Nervi, Ulrich Finsterwalder (1897-1988), Eduardo Torroja, Oscar Niemeyer (1907-2012), Félix Candela (1910-1997), Heinz Isler (1926- 2009), among others. They introduced innovative theories of design and construction and experimented with shells of different forms. Many shell structures designed during these years are world famous landmarks, some examples are shown in Figures 2.15, 2.16 and 2.17.

Concrete roof shells lost their popularity at the end of the years 1960s. The construction cost, especially due to the formwork production, has been identified as one of the main reasons [13]. However, in the latest years, a new interest in shell structures is arising. New materials and new design and construction methods have allowed to overcome difficulties that occurred in the past.

Shell structures will always have a fundamental role for architecture and engineering [1]. When designed properly, shells show their beauty and efficiency more than any other structural system [13].

Shells are able to span large column-free spaces offering to the designer numerous options when choosing their final geometry. Usually designers attempt to find shell shapes able to carry the applied loads in axial compression with minimal bending moments in order to minimize the thickness and the amount of material. Ideally, if there is no bending, the shell can be defined as *funicular*.

Figure 2.13: Municipal bus terminal in Salto by Eladio Dieste(Uruguay, 1974) [PC: Vicente del Amo]
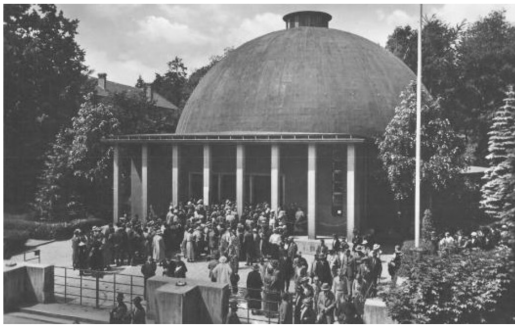
(a) *Historic view [PC: Karl Müller]*

(b) *Dome under construction [Image in the public domain]*

Figure 2.14: Zeiss-Planetarium by Walther Bauersfeld (Germany, 1922)

Figure 2.15: Palazzetto dello Sport by Annibale Vitellozzi and Pier Luigi Nervi (Rome, 1957) [Image in the public domain]

Figure 2.16: Igreja da Pampulha/Church of Saint Francis of Assisi by Oscar Niemeyer (Belo Horizonte, 1943) [PC: Bruno do Val]

Figure 2.17: Zarzuela's Hippodrome by Carlos Arniches Moltó, Martín Domíngues Esteban and Eduardo Torroja (Madrid, 1941) [PC: Ana Amado]

Chapter 3

Funicularity and form finding

Among efficient and optimized structural systems, funicular structures adopt the "right" shape in accordance with the applied load. Funicular shell structures are ideally able to resist external loads using membrane forces, mainly tension or compression forces, without introducing bending. As a result their thickness can be minimized and the amount of material reduced. The historical development of the concept of funicularity is reviewed in Section 3.1. In order to achieve "optimal" structural geometry in static equilibrium with a design loading, different form finding techniques have been developed during the years. An overview and classification of these methods is given in Section 3.2, while a brief definition of structural optimization is given in Section 3.3. Section 3.4 is devoted to the presentation of the Force density method.

3.1   About funicularity

The idea of funicularity has been formalized from an analytical point of view between 15th and 17th century. Otherwise one can observe many funicular structures constructed before this time, thanks to experience and static considerations of the designers and constructors; suspended bridges and corbelled domes represent some early examples.

(a) *Photo of the interior*   (b) *Drawing of the interior by Francesco Piranesi*
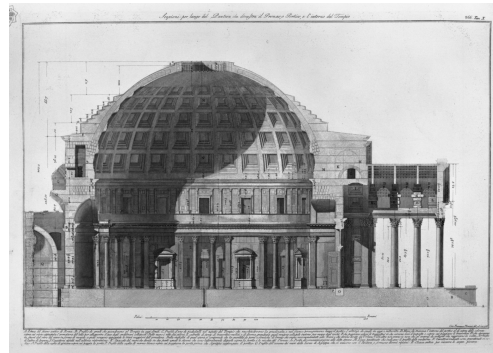
Figure 3.1: Pantheon (Rome, 118-125 AD) [Images in the public domain]

During the Roman period, builders seem to have some awareness of funicularity expressed in attempts to change load distributions to achieve better structural stability (e.g. use of filler materials or use of concrete with graded density) [103]. One famous example that seems

to confirm this hypothesis is the Pantheon (Fig.3.1). The iconic dome of the Pantheon was made possible by the use of concrete, a Roman material innovation of that time, employed adopting a structurally efficient solution. The five rows of coffers, as shown in Figure 3.1, have been constructed with variable density and this load distribution is key to guarantee the structural stability of the building, as demonstrated in [57].

In order to find some written essays concerning this topic, one needs to look at the 13th century. The medieval architect Villard de Honnecourt in his manuscript "Livre de portraiture", between sketches and notes, describes how to construct a cross vault optimizing the entire process with the application of the rule of the three arches [28]. At a later date, it has been confirmed that cross vaults constructed respecting this rule have a better structural behavior since the bending stresses are reduced [31]. This could demonstrate an intuition of the relationship between shape and performance of the structure, even if this concept was not analytically expressed during the Middle Ages [34]. Starting from the 15th century, the first studies on arches and cables appear. Theoretical definitions attempt to justify and formalized what was experimentally evident. Leon Battista Alberti (1404-1472), Andrea Palladio (1508-1580), Leonardo da Vinci (1452-1519) and Simon Stevin (1548-1620) are some of the most celebrated scientists to give a fundamental contribution to the formulation of the behavior of curved structure and of the arch equilibrium [103]. Galileo Galilei (1564-1642) was the first one who attempted to give a mathematical description of a cable; in his writing "Dialogues Concerning Two New Sciences" (1638), mistakenly using an erroneous analogy with the parabolic motion of projectiles, he confused catenary and parabola [35]. Joachim Jungius (1587-1657) rejected Galilei's statement, demonstrating the difference between the two, which increases when the sag to span ratio decreases. Jungius's writing "Geometria Empyrica" was published in 1669 after his death [103]. The correct equation of a cable's geometry was written in 1691 by Gottfried Wilhelm von Leibniz (1646-1716), Christiaan Huygens (1629-1695) and Johann Bernoulli (1667-1748) [24]. Huygens was the first one to use the term *catenaria* in one of his missive to Leibniz. English engineer and scientist Robert Hooke (1635-1703) gave an additional fundamental contribution in 1676 publishing in an appendix to his Description of Helioscopes the Latin anagram indicated in Figure 3.2. The
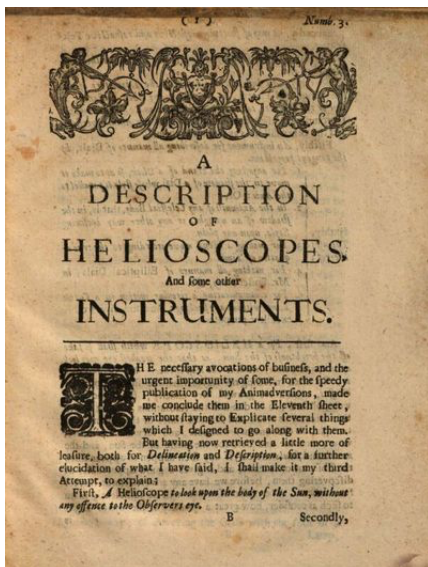
(a) *A description of helioscopes, and some other instruments by Robert Hooke*
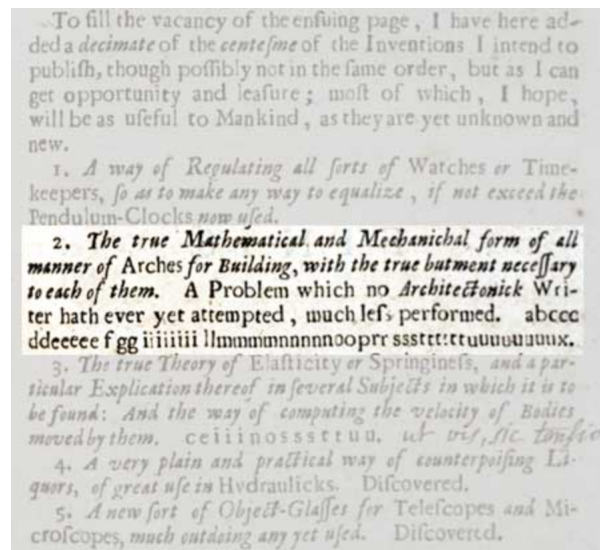
(b) *Robert Hooke's anagram, excerpt from his manuscript*

Figure 3.2: Robert Hooke's Latin anagram (Hooke, 1676) [Images in the public domain]

solution was published by the secretary of the Royal Society, Richard Waller in 1705 and read "Ut pendet continuum flexile, sic stabit contiguum rigidum inversum", the translation is "As hangs the flexible line, so but inverted will stand the rigid arch" [81]. The concept is simple: in order to obtain an arch that acts in pure compression, the shape of the equivalent hanging chain needs to be inverted. During the same years, David Gregory (1659-1708) stated that an arch is stable if the *thrust line*, that is the line representing the path of the resultants of forces acting in a structure, lies within its thickness [40]. This is the basic concept behind the structural assessment of masonry structures. In 1748, Poleni used Hooke's idea and Gregory's statement to assess the safety of the cracked dome of St. Peter's in Rome. Poleni showed that the dome was safe by employing the hanging chain principle (Fig. 3.3).
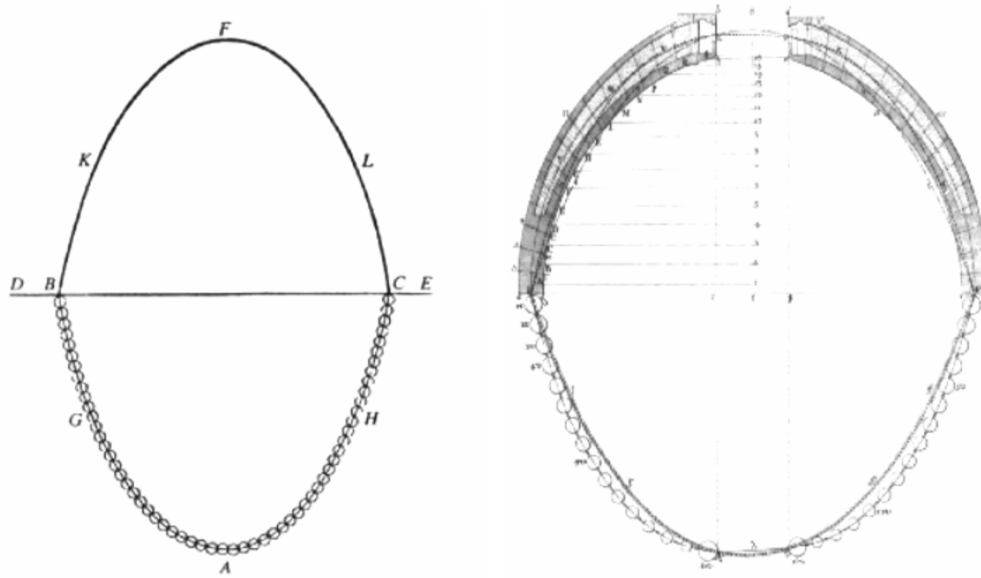
(a) *Hooke's analogy between an arch and a hanging chain*   (b) *Analysis of the Dome of St. Peter's in Rome*

Figure 3.3: Poleni's drawings and studies of the Dome of St. Peter's in Rome (Poleni, 1748) [Images in the public domain]

For this, he divided the dome in slices and hung thirty-two unequal weights proportional to the weight of corresponding sections of that "arch" wedge, and then showed that the hanging chain could fit within the section of the arch [43, 11]. Some years later, Claude-Louis Navier (1785-1836) and E. Méry (1840) supposed that in order to have an arch fully compressed, the thrust line would have to lie within the middle third of his section [44]. The thrust line becomes an indicator of the stability of arches: the more this line lies away from the axis of the arch, the more its thickness needs to be increased. Hence the "right" shape for an arch is the one corresponding to the funicular of the loads applied.

3.2 Form finding

The inversion principle proposed by Robert Hooke can be considered the earliest example of structural form finding for an arch. *Form finding* can be defined as a "forward process in which parameters are explicitly/directly controlled to find an optimal geometry of a structure which is in static equilibrium with a design loading" [1].

Beyond the one-dimensional (1D) case represented by the arch, Hooke's principle can be extended to 3D surfaces of different geometries such as shell structures. As seen in Chapter 2, when designing a shell a membrane behavior should be pursued, avoiding bending. Hence between all possible shapes, a funicular one should be adopted. In the last two centuries, three different groups of methods have been formalized to find the "right" shape and define funicular geometries.

3.2.1 Physical models

The first group of form finding methods uses *physical models* where bending stiffness is neglected, as hanging chains or membranes models. The inversion principle is applied to find bending-free shapes. Compare to the case of the 1D hanging cable, it should be noted that hanging membranes are more complex: multiple funicular solutions are possible, because multiple load paths can be found [1].

Sir Christopher Wren (1632-1723) was one of the first designers to apply Hooke's studies and use chain models to design the dome of the St. Paul's Cathedral in London, his drawings are shown in Figure 3.4. As seen in Section 3.1, also Giovanni Poleni (1683-1761) followed the same principle to assess the structural behavior of the dome of the St. Peter's Cathedral in Rome.
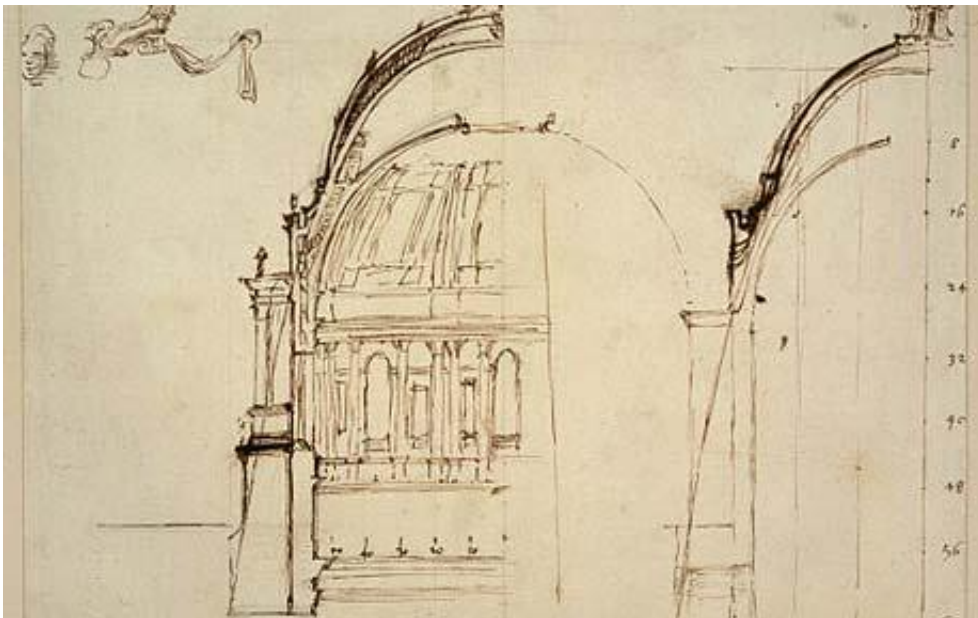
Figure 3.4: Sir Cristopher Wren's sketches of the Dome of St. Paul's in London (Wren, 1690) [Image in the public domain]

In the 19th century, Heinrich Hübsch (1795-1863) investigated the form of arches and vaults with the support of hanging string models and in 1837 his method was applied to design a dome in Kassel, Germany obtaining a significant reduction of the structure's thickness [1].

More recently, Antoni Gaudì (1852-1926), Frei Otto (1925, 2015) and Heinz Isler are some of the most famous designers who used this method to establish structural shapes in their projects. They preferred different types of physical models made of various materials. Examples of models used by Gaudì are indicated in Figures 3.5 and 3.6.

The Spanish Catalan architect disliked drawings and explored some of his designs using scale models made of chains or weighted threads and turning the model upright by the help

of a mirror placed underneath.

In the second half of 19th century, Frei Otto (1925-2015) and his colleagues at the Institute of Lightweight Structures in Stuttgart, Germany developed a different range of modeling techniques using elastic sheets, nets and also soap bubbles (Fig. 3.7) [110]. Otto applied physical models to design tension structures where gravity loads played a minor parts in defining the geometry [1]; for this reason, soap bubble models where largely employed by the German designer. A soap bubble structure in fact, constrained by its wands, always minimizes its surface having a constant surface tension. A minimal surface is the one with minimal energy between all possible shapes. The challenge is then to measure the bubble shape using photogrammetric techniques and taking advantage of the mirroring surface [61].

Figure 3.5: Reproduction of Gaudi's chain model displayed at the Casa Milà or Pedrera, Barcelona [PC: Author]

(a) *Reproduction of Gaudi's hanging model*
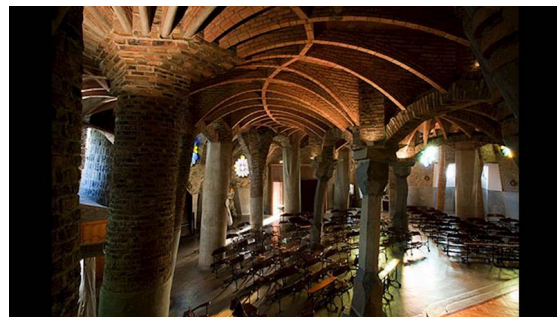
(b) *Internal view of the structure*

Figure 3.6: Crypt of Colonia Güell by Antoni Gaudì (Barcelona, 1908) [Images in the public domain]
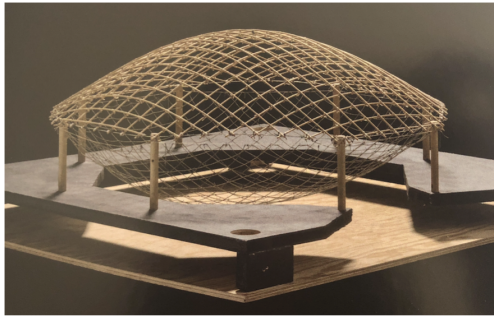
(a) *Net model for lattice structure during the Summer Academy (Saizburg, 1971) [110]*

(b) *Chain model for the Mannheim Multihalle (Germany, 1974) [Image in the public domain]*
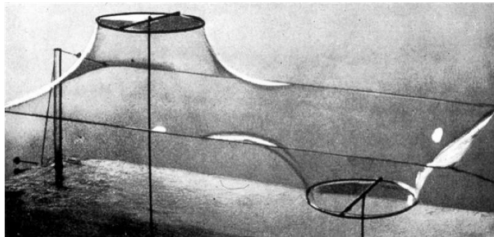
(c) *Soap bubble experimenting model [Image in the public domain]*
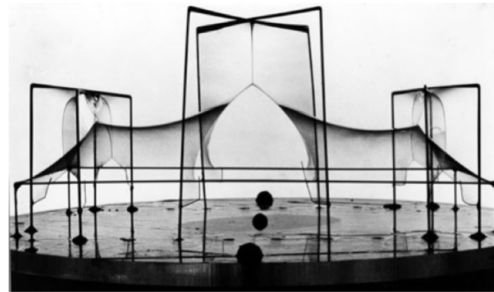
(d) *Soap bubble model for a tensile membrane roof [Image in the public domain]*

Figure 3.7: Frei Otto's form finding models

Contemporary of Frei Otto, Heinz Isler (1926-2009) took Hooke's inversion principle in three dimensions, using hanging sheets of cloth instead of chains. Each of Isler's shell shape is unique and most of them have been developed by the Swiss engineer taking advantage of the cold winter: a piece of wet cloth was suspended outdoors and left to freeze during the night as shown in Figure 3.8 [19].

Elegant thin shells as the one indicated in Figure 3.9 are the result of Isler's form finding techniques. Once defined the geometry, a mathematical model was applied to finalize the design and calculate the amount of reinforcement.

In the same period but in a different location, Sergio Musmeci (1926-981) questioned the relationship between architectural form and structure. The Italian engineer used textile membrane and soap film models to go beyond the analytical model developed in his theoretical studies [46, 75]. The Basento bridge in Potenza, Italy, known as the bridge "with the unnamed shape" [47], is the most famous structure realized by Musmeci and will be extensively discussed in Chapter 4.

About physical models, it is relevant to evidence that only for some types of structures a small model may provide insight into the behavior of a real scale version. Masonry arches, hanging chains and funicular vaults can be placed in this category. However, there are many other structures that cannot be simply scaled up. The stiffness of a beam or the buckling strength of a thin shell cannot be evaluated scaling up linearly the full size structure. Hence a distinction between *scale-independent* and *scale-dependent* models is made [1].

Physical models present some advantages. The physical model form finding process can help to generate surfaces different from the common geometric shapes and provide immediate feedback to change of loading or support conditions. On the other side, some disadvantages may be the amount of work and time necessary to construct a detailed and reliable model,

and the complexity to measure it to get the final shape. Difficulties can also arise when trying to apply variable thickness or loads different from the vertical ones.
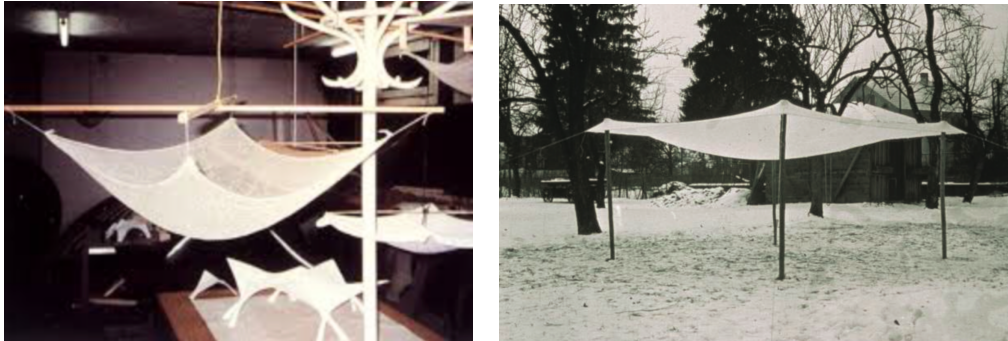
(a) *Hanging cloth model [Image in the public domain]*

(b) *Hanging cloth model left to freeze [19]*

Figure 3.8: Heinz Isler's hanging membrane models

Figure 3.9: Motorway service station in Deitingen by Heinz Isler (Switzerland, 1968) [via wikimedia.org]

3.2.2 Graphic methods

The second group of form finding methods is made of *graphic methods*, among which graphic statics is the most well known. This one is based on the parallelogram rule introduced by Simon Stevin [100] and the dualism between the funicular polygon and the force polygon introduced later by Varignon (1654-1722) [107]. In his work, Varignon described how to construct the funicular form of a hanging, inelastic rope using attached weights, as shown in Figure 3.10.

In 1866, Karl Culmann (1821-1881) was the first one to formalize graphical analysis as a powerful method for equilibrium analysis of structures [11, 26]. The method uses two
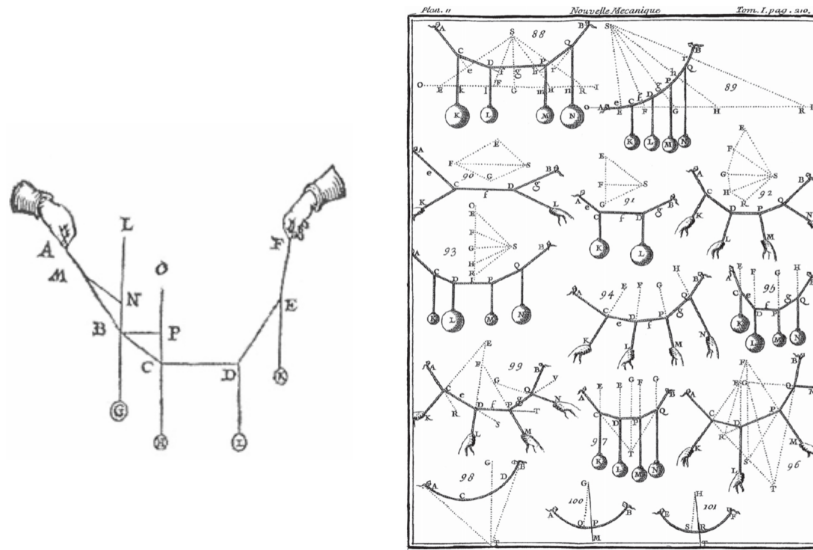
(a) *Force equilibrium of hanging weights on a string by Stevin [100]*

(b) *Illustration of funicular polygons by Varignon [107]*

Figure 3.10: Introduction of graphic statics by Simon Stevin and Pierre Varignon

diagrams: a form diagram, representing the geometry of the structure, and a force diagram (also known as Cremona or Maxwell-Cremona diagram), representing the equilibrium of the internal forces and external loads acting on the structure. The geometrical and topological relationship between form and force diagrams is called reciprocal [1, 93].

During the 19th century, graphic statics has been widely applied by Luigi Cremona (1830-1903), James C. Maxwell (1831-1879) and William Rankine (1820-1872) [44, 55]. Until the beginning of 20th century, many designers such as Gustave Eiffel (1832-1923), Rafael Guastavino Sr. (1842-1908), Pier Luigi Nervi and Eladio Dieste used graphic statics in their projects. However, by 1920 graphical methods were largely replaced by analytical methods. The reasons are to be found in the time-consuming drawing work, the limitations in addressing advanced problems in case of complex structures and the difficulties to extend the method from 2D to 3D problems [93]. Only recently, research on 3D graphic statics has been undertaken again.

The Thrust network analysis (TNA) method has been developed to extend the concepts of thrust line and graphic statics to 3D problems [12, 10]. Thrust networks correspond to the 3D version of thrust lines and are used for the analysis and design of vaulted masonry structures under vertical loading. The TNA method uses form and force diagrams to define the geometry of the structure and represent the distribution of the horizontal thrust, respectively. The funicular shape under the action of the applied load is obtained.

3.2.3   Numerical methods

The last and most recent group of form finding methods is made of *numerical methods*, developed from the years 1960s. This category can be subdivided in three groups depending on the computational approach adopted [108]:

- *Stiffness matrix methods* are among the oldest form finding methods and are based on the use of the elastic and geometric stiffness matrices. They have been criticized

for including the material properties, which is computationally costly and may lead to problems of convergence [42].

- *Geometric stiffness methods* use only a geometric stiffness and are material independent. The Force density method (FDM) [96] is the most popular and will be discussed in Section 3.4, several later methods have been presented as generalizations or extensions of it.

- *Dynamic equilibrium methods* are the ones that arrive at a steady-state solution solving the problem of dynamic equilibrium of a system of concentrated masses. The parameters defined have no physical representation and the convergence of the problem depends strongly on the surface discretization. The Dynamic relaxation (DR) [27] and the Particle-spring method (PS) [52] are part of this group.

With the development of computer technology, numerical form finding methods have been commonly implemented in software, partly replacing physical models and graphic methods.

3.2.4 Form finding digital tools

Nowadays computer aided models and digital morphogenesis models have been developed, making more approachable the application of form finding methods to search the "right" structural shape.

The digital tools available are numerous. Geometry based tools are implemented in computer aided design (CAD) softwares that allow the user to change easily the geometry of the structure. The most well known form finding tools of this category are based on the use of the 3D modeling software Rhinoceros together with Grasshopper, a visual algorithm editor integrated with Rhinoceros [101] (Fig. 3.11). In Rhinoceros the geometry of surfaces is defined using Non-Uniform Rational Basis Splines (NURBS) as parameterization. Among others, RhinoVAULT is a geometry based tool developed by the Block Research Group (ETH Zurich) that implements graphic statics, while Kangaroo Physics, developed by Daniel Piker, implements the Particle-spring method.
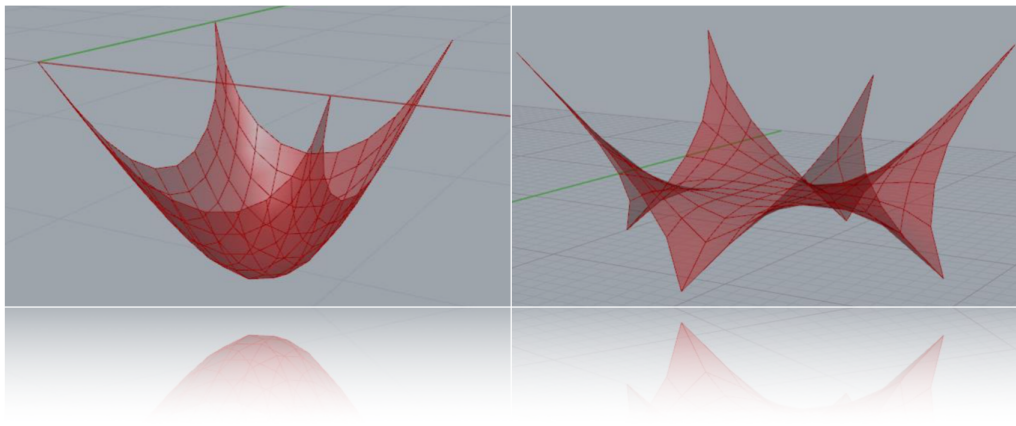
Figure 3.11: Examples of CAD model developed in Grasshopper and Rhinoceros

Other available tools are based on Finite Element (FE) modeling and allow calculation of stresses, deflections, etc. As example, Karamba is a plug-in of Grasshopper based on FE developed by Clemens Preisinger.

Since the work done by digital tools is often non-transparent to the user, they have been defined as "black boxes". Although the use of computer tools can help immensely the designer and offer many benefits compare to the past, a critical understanding of the methodologies implemented remains crucial. In the author's opinion, this thought is perfectly expressed by Anton Tedesko's words:

> "Young engineers are often perfect in using computers, but they don't know where to put the comma. It's not the computer that produces ideas. Let us not throw away the pencil and the slide rule." (Tedesko, 1967) [111]

> "Computers cannot replace engineering judgement and are no substitute for good design. Computers can show us what new shapes are possible; they opened up new opportunities and are a wonderful tool in the hands of experienced engineers for speeding up calculations and replacing the tedious work of former days. They make it easier to cope with complicated shapes." (Tedesko, 1971) [102]

3.3   Structural optimization

Structural optimization can be defined as an "inverse process in which parameters are implicitly/indirectly optimized to find the geometry of a structure such that an objective function or fitness criterion is minimized" [1]. While form-found shapes are usually generated settings supports and external loadings as parameters, structural optimization methods can be applied to introduce additional constraints. Both form-found shapes and freeform or mathematical shapes can be used as initial geometry.

Depending on the variables involved, three structural optimization categories may be identified:

- *Sizing optimization*, where variables such as cross-section dimension or transverse thickness of the structure are considered. Topology and shape are fixed.

- *Shape optimization*, where the variables are the coordinates of the structural surface nodes. During the process, the geometry is modified, not the topology.

- *Topology optimization*, where the variables are represented by the connectivity of the nodes of the structure, hence the topology. During the process, the starting area with homogeneous material distribution becomes highly inhomogeneous: no-mass areas (openings and holes) and high-density areas (bars and struts) arise.

The complexity and the numerical efforts strongly increase from sizing to shape to topology optimization. While for sizing and shape optimization a first design proposal exists, this is not the case for the topology optimization.

The optimization problem is defined:

- Linear programming (LP) if objective and constraint functions are linearly dependent;

- Quadratic programming (QP) if the objective function is quadratic and the constraint function is linearly dependent;

- Non-Linear programming (NLP) if objective and constraint functions are non-linearly dependent.

Structural optimization may be objective or multi-objective. Shape optimization objectives may be weight minimization or strain energy minimization (that is equal to maximize the stiffness) [8, 9].

3.4 Force density method

The *linear Force density method* (LFDM) is one of the most used numerical form finding methods. It was originally developed for cable-net structures by Klaus Linkwitz (1927-2017) and applied optimizing the geometry of the pre-stressed cable-net roof of the Olympic Stadium in Munich by Günther Behnisch (1922-2010) and Frei Otto shown in Figure 3.12.
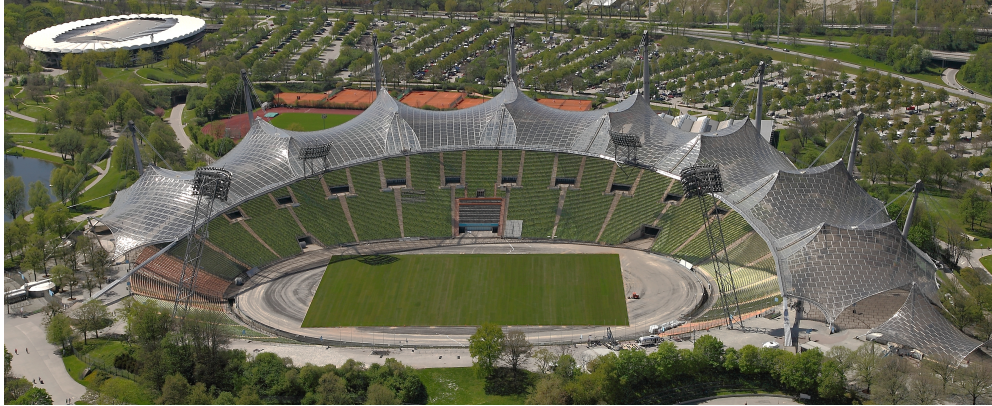
Figure 3.12: Olympic Stadium by Günther Behnisch and Frei Otto (Munich, 1972) [PC: IMGKID]

Hans-Jörg Schek, advised by Professor Linkwitz during his Ph.D., clearly and concisely described the Force density method in [96]. The main advantage of the procedure lies in the fact that any state of equilibrium of a discrete network can be obtained by the solution of one system of linear equations. The *force density* is defined as the ratio of force over length in a branch of the net structure. Each branch of the equilibrium structure has one prescribed force density.

The linear approach is then extended to the *non linear Force density method* (NLFDM) in order to include additional geometrical conditions or force constraints. According to the definitions given in Section 3.3, the non linear Force density method is a structural shape optimization method.

Following the formulation given by Schek, the steps of both LFDM and NLFDM are presented. A code to perform the form finding and the structural shape optimization of a general network according to the linear and non linear approaches has been implemented by the author in the numerical computing environment and proprietary programming language Matlab [67].

3.4.1 Linear Force density method

Given a graph of a network, all nodes are numbered from 1 to n_s and all branches from 1 to m, in any order. The fixed nodes are taken at the end of the sequence and have number n_f, the free nodes have number n. Hence we have $n_s = n + n_f$. A graph of a portion of a general network is shown in Figure 3.13.

The branch-node matrix $\mathbf{C_s}$ is defined with m rows and n_s columns. Each element $c_{i,j}$ of the matrix is equal to:

- zero if the node is not connected to the branch;

- +1 if the branch is directed toward the node;

- −1 if the branch is directed away from the node.
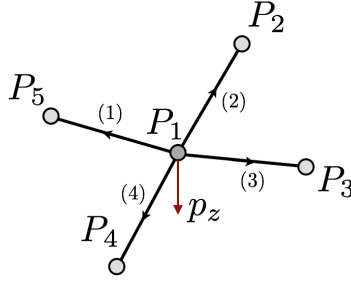
Figure 3.13: Network graph with 5 nodes, 4 branches and a vertical load

Referring to Figure 3.13, all elements $c_{i,1}$ of the 4×5 matrix $\mathbf{C_s}$ are equal to -1, while the other elements are zero.

According to the classification into free and fix nodes, the matrices $\mathbf{C}$ and $\mathbf{C_f}$ are defined.

All free nodes P_i have coordinates x_i, y_i, z_i where $i = 1, 2, ..., n$. The fixed nodes have coordinates x_{fi}, y_{fi}, z_{fi} where $i = 1, 2, ..., n_f$. The n-vectors $\mathbf{x}, \mathbf{y}, \mathbf{z}$ and the n_f-vectors $\mathbf{x_f}, \mathbf{y_f}, \mathbf{z_f}$ of the corresponding coordinates can be defined.

Other definitions include the m-vector of the branch lengths $\mathbf{l}$, the m-vector of the branch forces $\mathbf{s}$ and n_s-vectors of the loads $\mathbf{p_x}, \mathbf{p_y}, \mathbf{p_z}$.

The coordinate difference vectors $\mathbf{u}, \mathbf{v}, \mathbf{w}$ of the connected points are calculated as follows:

$$\begin{cases} \mathbf{u} = \mathbf{Cx} + \mathbf{C_f x_f} \\ \mathbf{v} = \mathbf{Cy} + \mathbf{C_f y_f} \\ \mathbf{w} = \mathbf{Cz} + \mathbf{C_f z_f} \end{cases} \qquad (3.1)$$

$\mathbf{U}, \mathbf{V}, \mathbf{W}$ and $\mathbf{L}$ are the diagonal matrices of the corresponding vectors.

Since the compatibility between elongation of the branch and geometry of the net in the final state must be satisfied, the branch length vector $\mathbf{l}$ and the matrix $\mathbf{L}$ can be calculates as follows:

$$\mathbf{l} = \sqrt{\mathbf{u^2 + v^2 + w^2}} \qquad \qquad \mathbf{L} = \sqrt{\mathbf{U^2 + V^2 + W^2}} \qquad (3.2)$$

Using the Jacobian matrices, from (3.1) and (3.2) the following is obtained:

$$\begin{cases} \frac{\delta \mathbf{l}}{\delta \mathbf{x}} = \mathbf{C^t U L^{-1}} \\ \frac{\delta \mathbf{l}}{\delta \mathbf{y}} = \mathbf{C^t V L^{-1}} \\ \frac{\delta \mathbf{l}}{\delta \mathbf{z}} = \mathbf{C^t W L^{-1}} \end{cases} \qquad (3.3)$$

Looking at Figure 3.14, the component l_j of the vector $\mathbf{l}$ is:

$$l_j = \sqrt{(x_2 - x_1)^2 + (y_2 - y_1)^2 + (z_2 - z_1)^2} \qquad (3.4)$$

$$\mathbf{x_1} \in \mathbf{x}$$
$$\mathbf{x_2} \in \mathbf{x_f}$$
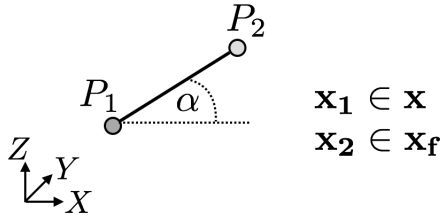
Figure 3.14: Branch of a network graph in the Cartesian coordinate system X, Y, Z

If s_j is the force in the branch and p_x the external load, the equilibrium in X direction can be written as follows:

$$s_j cos\alpha_j + p_x = s_j \frac{x_2 - x_1}{l_j} + p_x = 0 \tag{3.5}$$

Using (3.4), the following is obtained:

$$\frac{\delta l_j}{\delta x} = -\frac{x_2 - x_1}{l_j} \tag{3.6}$$

At this point, Equation (3.5) can be written as:

$$s_j - \frac{\delta l_j}{\delta x} + p_x = 0 \tag{3.7}$$

Generalizing and applying Equations (3.3), the equilibrium in every node and each direction between external loads and internal forces is expressed by the following system of equations:

$$\begin{cases} \mathbf{C^t U L^{-1} s = p_x} \\ \mathbf{C^t V L^{-1} s = p_y} \\ \mathbf{C^t W L^{-1} s = p_z} \end{cases} \tag{3.8}$$

As anticipated the force density is the ratio of force over length in a branch, so the m-vector $\mathbf{q}$ is set:

$$\mathbf{q = L^{-1} s} \tag{3.9}$$

Equilibrium Equations (3.8) can be written as:

$$\begin{cases} \mathbf{C^t U q = p_x} \\ \mathbf{C^t V q = p_y} \\ \mathbf{C^t W q = p_z} \end{cases} \tag{3.10}$$

$\mathbf{Q}$ is the diagonal matrix of the vector $\mathbf{q}$ and the following identities are valid:

$$\mathbf{U q = Q u} \qquad \mathbf{V q = Q v} \qquad \mathbf{W q = Q w} \tag{3.11}$$

Using Equations (3.1), equilibrium Equations (3.10) can be written as:

$$\begin{cases} \mathbf{C^t Q C x + C^t Q C_f x_f = p_x} \\ \mathbf{C^t Q C y + C^t Q C_f y_f = p_y} \\ \mathbf{C^t Q C z + C^t Q C_f z_f = p_z} \end{cases} \tag{3.12}$$

or, for sake of brevity, setting $\mathbf{D = C^t Q C}$ and $\mathbf{D_f = C^t Q C_f}$, as:

$$\begin{cases} \mathbf{D x = p_x - D_f x_f} \\ \mathbf{D y = p_y - D_f y_f} \\ \mathbf{D z = p_z - D_f z_f} \end{cases} \tag{3.13}$$

Equations (3.13) are linear. Under a given load and a given position of fixed points, for each set of prescribed force densities, one equilibrium state exists.

The shape of the network corresponding to the equilibrium state can be calculated computing the coordinates of the nodes as follows:

$$\begin{cases} \mathbf{x = D^{-1}(p_x - D_f x_f)} \\ \mathbf{y = D^{-1}(p_y - D_f y_f)} \\ \mathbf{z = D^{-1}(p_z - D_f z_f)} \end{cases} \tag{3.14}$$

As many equilibrium shapes as force density vectors $\mathbf{q}$ can be obtained.

3.4.2   Non Linear Force density method

If further conditions are prescribed, the choice of the force densities becomes restricted and the Force density method becomes non linear. The shape obtained at the end of the linear Force density method is adopted as initial geometry to start the iterations.

The r-vector $\mathbf{g}$ represents the r conditions imposed:

$$\mathbf{g}(\mathbf{x}, \mathbf{y}, \mathbf{z}, \mathbf{q}) = \mathbf{0} \tag{3.15}$$

Remembering Equations (3.14), where the coordinates are represented as functions of the force densities, the additional condition vector can be written as:

$$\mathbf{g}^*(\mathbf{q}) = \mathbf{g}(\mathbf{x}(\mathbf{q}), \mathbf{y}(\mathbf{q}), \mathbf{z}(\mathbf{q}), \mathbf{q}) = \mathbf{0} \tag{3.16}$$

If $\mathbf{q}^{(0)}$ is the vector of the force densities belonging to the shape found at the end of the linear Force density method, the non linear equations $\mathbf{g}^*(\mathbf{q}^{(0)}) = \mathbf{0}$ will not be satisfied. Hence the new force density vector $\mathbf{q}^{(1)} = \mathbf{q}^{(0)} + \boldsymbol{\Delta}\mathbf{q}$ is sought, in order to satisfy the equations $\mathbf{g}^*(\mathbf{q}^{(1)}) = \mathbf{0}$.

Because of the non linearity, the iterative Newton-Raphson method is set:

$$\mathbf{g}^*(\mathbf{q}^{(0)}) + \frac{\delta\mathbf{g}^*(\mathbf{q}^{(0)})}{\delta\mathbf{q}}\boldsymbol{\Delta}\mathbf{q} = \mathbf{0} \tag{3.17}$$

Having $\mathbf{g}^*(\mathbf{q}^{(0)}) = -\mathbf{r}$ and $\frac{\delta\mathbf{g}^*(\mathbf{q}^{(0)})}{\delta\mathbf{q}} = \mathbf{G}^{\mathbf{t}}$, Equation (3.17) can be written as the linear condition:

$$\mathbf{G}^{\mathbf{t}}\boldsymbol{\Delta}\mathbf{q} = \mathbf{r} \tag{3.18}$$

The initial force density vector $\mathbf{q}^{(0)}$ is used in the first iteration, for the next one $\mathbf{q}^{(0)} + \boldsymbol{\Delta}\mathbf{q}$ is used and so on until $\mathbf{g}^*$ is zero within a given tolerance.

Since the additional conditions are usually given as functions of $\mathbf{x}, \mathbf{y}, \mathbf{z}$ and $\mathbf{q}$, the Jacobian matrix $\mathbf{G}^{\mathbf{t}}$ can be represented as:

$$\mathbf{G}^{\mathbf{t}} = \frac{\delta\mathbf{g}^*}{\delta\mathbf{q}} = \frac{\delta\mathbf{g}}{\delta\mathbf{x}}\frac{\delta\mathbf{x}}{\delta\mathbf{q}} + \frac{\delta\mathbf{g}}{\delta\mathbf{y}}\frac{\delta\mathbf{y}}{\delta\mathbf{q}} + \frac{\delta\mathbf{g}}{\delta\mathbf{z}}\frac{\delta\mathbf{z}}{\delta\mathbf{q}} + \frac{\delta\mathbf{g}}{\delta\mathbf{q}} \tag{3.19}$$

With reference to the equilibrium Equations (3.10), any changes $\mathbf{dq}$ and $\mathbf{dx}$ should leave untouched the state of equilibrium in the X direction. Hence the following is valid:

$$\mathbf{d}(\mathbf{C}^{\mathbf{t}}\mathbf{U}\mathbf{q}) = \frac{\delta(\mathbf{C}^{\mathbf{t}}\mathbf{U}\mathbf{q})}{\delta\mathbf{q}}\mathbf{dq} + \frac{\delta(\mathbf{C}^{\mathbf{t}}\mathbf{U}\mathbf{q})}{\delta\mathbf{x}}\mathbf{dx} = \mathbf{0} \tag{3.20}$$

Since $\frac{\delta(\mathbf{C}^{\mathbf{t}}\mathbf{U}\mathbf{q})}{\delta\mathbf{q}} = \mathbf{C}^{\mathbf{t}}\mathbf{U}$ and $\frac{\delta(\mathbf{C}^{\mathbf{t}}\mathbf{U}\mathbf{q})}{\delta\mathbf{x}} = \frac{\delta(\mathbf{C}^{\mathbf{t}}\mathbf{Q}\mathbf{u})}{\delta\mathbf{x}} = \mathbf{C}^{\mathbf{t}}\mathbf{Q}\frac{\delta\mathbf{u}}{\delta\mathbf{x}} = \mathbf{C}^{\mathbf{t}}\mathbf{Q}\mathbf{C}$, X direction equilibrium Equation (3.20) becomes:

$$\mathbf{C}^{\mathbf{t}}\mathbf{U}\mathbf{dq} + \mathbf{C}^{\mathbf{t}}\mathbf{U}\mathbf{C}\mathbf{dx} = \mathbf{0} \rightarrow \frac{\delta\mathbf{x}}{\delta\mathbf{q}} = -\frac{\mathbf{C}^{\mathbf{t}}\mathbf{U}}{\mathbf{C}^{\mathbf{t}}\mathbf{Q}\mathbf{C}} = -\mathbf{D}^{-1}\mathbf{C}^{\mathbf{t}}\mathbf{U} \tag{3.21}$$

Applying the same procedure in Y and Z directions:

$$\begin{cases} \frac{\delta\mathbf{x}}{\delta\mathbf{q}} = -\mathbf{D}^{-1}\mathbf{C}^{\mathbf{t}}\mathbf{U} \\ \frac{\delta\mathbf{y}}{\delta\mathbf{q}} = -\mathbf{D}^{-1}\mathbf{C}^{\mathbf{t}}\mathbf{V} \\ \frac{\delta\mathbf{z}}{\delta\mathbf{q}} = -\mathbf{D}^{-1}\mathbf{C}^{\mathbf{t}}\mathbf{W} \end{cases} \tag{3.22}$$

At this point, the Jacobian matrix $\mathbf{G}^{\mathbf{t}}$ can be calculated according to the possible different constraints applied to the network.

Node distance conditions

Since the length $\bar{\mathbf{l}}_v$ is prescribed to the first r branches, the imposed condition is expressed as:

$$\mathbf{g}(\mathbf{x}, \mathbf{y}, \mathbf{z}) = \bar{\mathbf{l}} - \bar{\mathbf{l}}_v = 0 \tag{3.23}$$

where $\bar{\mathbf{l}}$ contains the r components of the m-vector $\mathbf{l}$. Similarly $\bar{\mathbf{L}}$, $\bar{\mathbf{U}}$ and $\bar{\mathbf{C}}$ are defined.

The condition $\mathbf{g}$ depends on $\mathbf{x}, \mathbf{y}, \mathbf{z}$, so $\frac{\delta \mathbf{g}}{\delta \mathbf{q}}$ is equal to zero.

Furthermore using Equations (3.23) and (3.3), the following system is obtained:

$$\begin{cases} \frac{\delta \mathbf{g}}{\delta \mathbf{x}} = \frac{\delta \bar{\mathbf{l}}}{\delta \mathbf{x}} = \bar{\mathbf{C}}^t \bar{\mathbf{U}} \bar{\mathbf{L}}^{-1} \\ \frac{\delta \mathbf{g}}{\delta \mathbf{y}} = \frac{\delta \bar{\mathbf{l}}}{\delta \mathbf{y}} = \bar{\mathbf{C}}^t \bar{\mathbf{V}} \bar{\mathbf{L}}^{-1} \\ \frac{\delta \mathbf{g}}{\delta \mathbf{z}} = \frac{\delta \bar{\mathbf{l}}}{\delta \mathbf{z}} = \bar{\mathbf{C}}^t \overline{\mathbf{W}} \bar{\mathbf{L}}^{-1} \end{cases} \tag{3.24}$$

Finally Equation (3.19) can be written using (3.22) and (3.24) in order to get the Jacobian matrix $\mathbf{G_d^t}$ in case of node distance conditions:

$$\mathbf{G_d^t} = -\bar{\mathbf{L}}^{-1}(\bar{\mathbf{U}}\bar{\mathbf{C}}\mathbf{D}^{-1}\mathbf{C}^t\mathbf{U} + \bar{\mathbf{V}}\bar{\mathbf{C}}\mathbf{D}^{-1}\mathbf{C}^t\mathbf{V} + \overline{\mathbf{W}}\bar{\mathbf{C}}\mathbf{D}^{-1}\mathbf{C}^t\mathbf{W}) \tag{3.25}$$

Force conditions

In this second case, given values $\bar{\mathbf{s}}_v$ are prescribed as forces in r selected branches. The imposed condition is expressed as:

$$\mathbf{g}(\mathbf{x}, \mathbf{y}, \mathbf{z}, \mathbf{q}) = \bar{\mathbf{s}} - \bar{\mathbf{s}}_v = \bar{\mathbf{L}}\bar{\mathbf{q}} - \bar{\mathbf{s}}_v = \bar{\mathbf{Q}}\bar{\mathbf{l}} - \bar{\mathbf{s}}_v = 0 \tag{3.26}$$

Using Equations (3.26) and (3.24), the following system can be calculated:

$$\begin{cases} \frac{\delta \mathbf{g}}{\delta \mathbf{x}} = \bar{\mathbf{Q}}\frac{\delta \bar{\mathbf{l}}}{\delta \mathbf{x}} = \bar{\mathbf{Q}}\bar{\mathbf{C}}^t \bar{\mathbf{U}} \bar{\mathbf{L}}^{-1} \\ \frac{\delta \mathbf{g}}{\delta \mathbf{y}} = \bar{\mathbf{Q}}\frac{\delta \bar{\mathbf{l}}}{\delta \mathbf{y}} = \bar{\mathbf{Q}}\bar{\mathbf{C}}^t \bar{\mathbf{V}} \bar{\mathbf{L}}^{-1} \\ \frac{\delta \mathbf{g}}{\delta \mathbf{z}} = \bar{\mathbf{Q}}\frac{\delta \bar{\mathbf{l}}}{\delta \mathbf{z}} = \bar{\mathbf{Q}}\bar{\mathbf{C}}^t \overline{\mathbf{W}} \bar{\mathbf{L}}^{-1} \\ \frac{\delta \mathbf{g}}{\delta \mathbf{q}} = \bar{\mathbf{L}} \end{cases} \tag{3.27}$$

Finally Equation (3.19) can be written using (3.22) and (3.27) in order to get the Jacobian matrix $\mathbf{G_d^t}$ in case of force conditions:

$$\mathbf{G_f^t} = \bar{\mathbf{L}} - \bar{\mathbf{Q}}\bar{\mathbf{L}}^{-1}(\bar{\mathbf{U}}\bar{\mathbf{C}}\mathbf{D}^{-1}\mathbf{C}^t\mathbf{U} + \bar{\mathbf{V}}\bar{\mathbf{C}}\mathbf{D}^{-1}\mathbf{C}^t\mathbf{V} + \overline{\mathbf{W}}\bar{\mathbf{C}}\mathbf{D}^{-1}\mathbf{C}^t\mathbf{W}) \tag{3.28}$$

Length distance conditions

The node distance condition refers to the length of the branches in the strained state. In this case a length distance condition is prescribed to the unstrained lengths $\bar{\mathbf{l}}_u$ (Fig. 3.15).
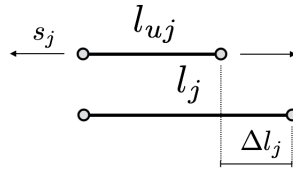
Figure 3.15: Strained and unstrained length of a network branch

Being s_j the force in the branch, σ the stress, ϵ the strain, A the branch section area and E the Young's Modulus, the following can be written:

$$\frac{\Delta l_j}{l_{uj}} = \frac{l_j - l_{uj}}{l_{uj}} = \epsilon = \frac{\sigma}{E} = \frac{s_j}{AE} \tag{3.29}$$

Defining the branch stiffness $h_j = AE$, Equation (3.29) becomes:

$$l_j - l_{uj} = \frac{s_j}{h_j}l_{uj} \rightarrow l_{uj} = \frac{h_j}{h_j + s_j}l_j \tag{3.30}$$

Since the length $\bar{\mathbf{l}}_{uv}$ is prescribed to the first r branches, the imposed condition is written as:

$$\mathbf{g}(\mathbf{x}, \mathbf{y}, \mathbf{z}, \mathbf{q}) = \bar{\mathbf{l}}_u - \bar{\mathbf{l}}_{uv} = \frac{\bar{\mathbf{h}}}{\bar{\mathbf{h}} + \bar{\mathbf{s}}}\bar{\mathbf{l}} - \bar{\mathbf{l}}_{uv} = 0 \tag{3.31}$$

Using Equations (3.31) and (3.24), the following system can be calculated:

$$\begin{cases} \frac{\delta \mathbf{g}}{\delta \mathbf{x}} = \bar{\mathbf{l}}_u^2 \bar{\mathbf{l}}^{-3} \bar{\mathbf{C}}^t \bar{\mathbf{U}} \\ \frac{\delta \mathbf{g}}{\delta \mathbf{y}} = \bar{\mathbf{l}}_u^2 \bar{\mathbf{l}}^{-3} \bar{\mathbf{C}}^t \bar{\mathbf{V}} \\ \frac{\delta \mathbf{g}}{\delta \mathbf{z}} = \bar{\mathbf{l}}_u^2 \bar{\mathbf{l}}^{-3} \bar{\mathbf{C}}^t \bar{\mathbf{W}} \\ \frac{\delta \mathbf{g}}{\delta \mathbf{q}} = -\bar{\mathbf{l}}_u^2 \bar{\mathbf{H}}^{-1} \end{cases} \tag{3.32}$$

Finally Equation (3.19) can be written using (3.22) and (3.32) in order to get the Jacobian matrix $\mathbf{G_d^t}$ in case of length distance conditions:

$$\mathbf{G_u^t} = -\bar{\mathbf{L}}_u^2 \bar{\mathbf{H}}^{-1} - \bar{\mathbf{L}}_u^2 \bar{\mathbf{L}}^{-3} (\bar{\mathbf{U}} \bar{\mathbf{C}} \mathbf{D}^{-1} \mathbf{C}^t \mathbf{U} + \bar{\mathbf{V}} \bar{\mathbf{C}} \mathbf{D}^{-1} \mathbf{C}^t \mathbf{V} + \bar{\mathbf{W}} \bar{\mathbf{C}} \mathbf{D}^{-1} \mathbf{C}^t \mathbf{W}) \tag{3.33}$$

If the branches have very high stiffness, the strained lengths become equal to the unstrained lengths, so $\bar{\mathbf{h}} \rightarrow \infty$ and $\mathbf{G_u^t} \rightarrow \mathbf{G_d^t}$.
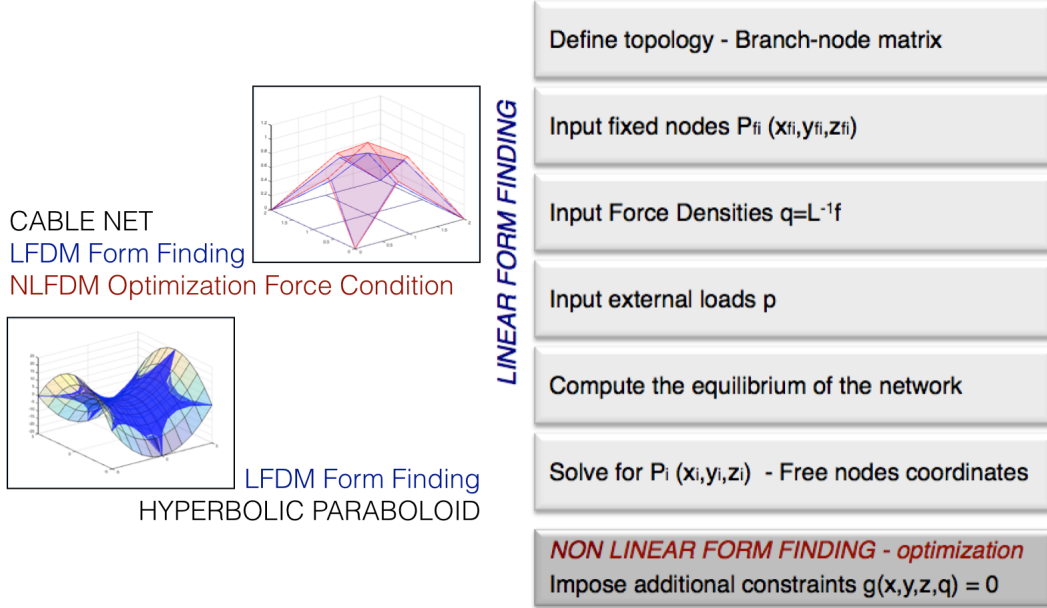
Figure 3.16: Force density method scheme and testing examples implemented in Matlab

Chapter 4

Musmeci and the Basento bridge

Many designers around the world have used form finding methods to design and construct elegant and efficient shell structures. Among others, the Italian engineer Sergio Musmeci is noteworthy for his ability to design continuous shells with unprecedented shapes well ahead of his time. His goal was trying to minimize the shell area while maximizing the structural behavior. Musmeci's most famous project, that well represents his design philosophy, is the bridge over the Basento river. Section 4.1 investigates Musmeci's education and experience leading to the project of the bridge. Section 4.2 reviews the design steps of the Basento bridge and discusses the different modeling and testing techniques adopted by Musmeci. Section 4.3 revisits the shape generation of the 3D surface structure using resources available nowadays and applying the Force density method as form finding technique. Finally the form-found shape is validated with the support of a FE model.

4.1   Sergio Musmeci

Quoting Sergio Musmeci:

> "There is no reason why the unknown factors should always be the internal stresses and not, for example, the geometric parameters which define the form itself of the structures, since in this latter case a uniformity of stresses and a more complete and efficient use of material may be obtained. With this method, it is possible to arrive at a synthesis of new forms rich in expressive strength."
> (Musmeci, 1980) [77]

Sergio Musmeci, shown in Figure 4.1, was a pioneer in the use of form finding techniques for the design of structural surfaces. Undertaking an iterative process and manipulating physical models, analytical formulations and Finite Difference (FD) simulations, he was able to derive incredible shapes for a broad range of structures.

Musmeci was born in 1926 in Rome, Italy. He had an interdisciplinary education, in fact he graduated in Civil Engineering in 1948 and in Aeronautical Engineering in 1953 [74]. After graduation, he worked as apprentice to Pier Luigi Nervi, recognized as the most brilliant artist of reinforced concrete of his time by Nikolaus Pevsner [106], and to Riccardo Morandi (1902-1989) [37]. During these years, Musmeci gained knowledge in reinforced concrete, pre-stressed structures, and bridge design [94]. As well as being a practicing civil engineer and designer, Musmeci was a faculty member at La Sapienza University in Rome. He was appointed lecturer in Analytical mechanics in 1968, and in Bridges and large structures in 1971 [15].

Pier Luigi Nervi and Riccardo Morandi played a crucial role in Musmeci's education. Both of them are known for their ability to balance architectural aesthetics and structural soundness in their innovative design. They are famous for their successful work using large scale concrete formwork and experimenting with pre-stressed technology. However they tended to adopt traditional shell forms and well established structural solutions such as arch bridges [106]. Musmeci continued their legacy but liberated himself from analytical prescribed forms, employing different form finding techniques to discover a wide range of new shapes [106].

Figure 4.1: Sergio Musmeci (left) in front of the Basento bridge [PC: Paolo Musmeci]

Also the Italian historical context played a role in Musmeci's path. Following the Second World War (WWII), the public sector and the construction industry were at a standstill. However advances continued to be made during these decades [48]. Engineers focused on research and theory rather than physical construction. It was at that time that material testing and pre-stressing techniques were investigated.

When the war ended, there was need for reconstruction of bridges and civil structures destroyed during the conflict. International funding allowed a rapid industrialization and population growth and, as a consequence, revitalized the construction industry [56]. Furthermore, Italy hosted high profile international events such as the 1960 Summer Olympics held in Rome and the 1961 International Exposition on Labor held in Turin [48].

The post-war Italian socio-economic context provided civil engineers with the opportunity to apply the technological advances made. With the development of pre-stressed and reinforced concrete, new structural surface geometries could be designed. During the years 1950s and 1960s, the so-called "structural expressionism" spread [48]. Italian architects and engineers worked hand in hand to create unique structures applying the newly developed theories. Italian architectural and engineering products became actual landmarks known world-wide and showcased at the exhibition "Twentieth Century Engineering" held in 1964 at the Museum of Modern Art in New York City, USA.

4.2   The design of the Basento bridge

The rapid Italian progress that followed WWII, led to urban sprawl and industrial development. Many areas, including the city of Potenza located in the south of Italy, experienced significant industrialization, especially along the watercourses such as the Basento river. As a consequence of the booming industry, the commuter traffic increased and the existing infrastructures such as railroads and bridges became inadequate [86].

The president of the Italian Consortium for the industrial development, Gino Viggiani (1920-2014) strongly advocated the construction of a new bridge that could meet the current needs as well as represent an excellent example of the 20th-Century Italian architecture. What set Musmeci apart from other bridge designers was his ability to experiment creating new structural forms. His goal was to find an optimized shape able to minimize the material employed in the construction. Ideally, the shell would have a membrane behavior with no bending moments, a uniform stress and a mean curvature equal to zero (minimal surface) [16]. Musmeci's conceptual idea took advantage of Hooke's inversion principle. In fact, Musmeci was seeking an isotropic shape surface able to carry only tensile stress, which he could translate into a structural shell surface carrying compression forces.

The Basento bridge shown in Figures 4.2 and 4.3 is made of a reinforced concrete structure with four spans and a total length of about 280 m. The transverse section of the deck is 16 m wide, but the supports are located 2 m away from the edges at a transverse distance of 12 m. The deck is supported every 17.30 m longitudinally. Sergio Musmeci started the design in 1967. The bridge was build between 1971 and 1976.

Figure 4.2: View of the Basento bridge [Image in the public domain]

Figure 4.3: Front view of the Basento bridge [Image in the public domain]

4.2.1 Design steps

To design the bridge over the Basento river, Musmeci combined physical, numerical and analytical methods. The process undertaken to generate the final shape can be organized into

seven steps divided in two different approaches: the form finding approach and the structural analysis approach. All steps have been carried out following the chronological order indicated in Table 4.1.

	Form Finding	Structural Analysis
1	Soap films - Physical model	-
2	Laplace equation - Mathematical model	-
3	1:100 Neoprene model - Physical model	-
4	-	1:100 Methacrylate model - Physical model
5		Beam model - Mathematical model
6	Finite Difference method - Numerical model	-
7	-	1:10 Concrete model - Physical model

Table 4.1: Musmeci's design steps for the Basento bridge

The sequence of the design steps shows that, while still seeking the final shape, Musmeci was also verifying the structural feasibility of the shell surface obtained from the application of different form finding techniques.

Firstly, Musmeci explored the potential of soap bubble models. As seen in Chapter 3, a soap bubble is a minimal surface with constant surface tension in all directions under a specific set of boundary conditions. Unlike the final geometry, Musmeci modeled the connections of the shell vault to the bridge deck using continuous wands. The soap anticlastic surface obtained by Musmeci and shown in Figure 4.4 was a source of inspiration for the 3D geometry of the lower bridge section that connects to the foundations.
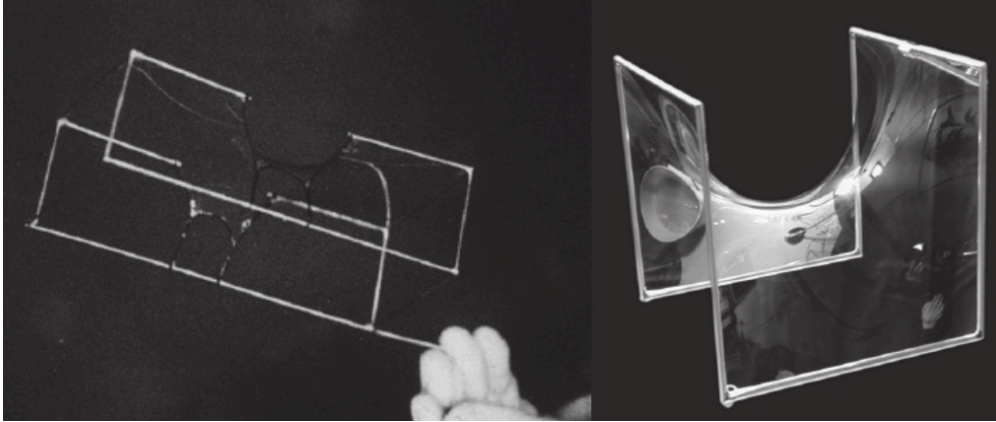
Figure 4.4: Musmeci's physical soap bubble model of the Basento bridge [16]

At this point, Musmeci was ready to compute the first approximation of the overall surface geometry using the Laplace equation. The equation considered is:

$$div(\nabla z) = \frac{q}{N} \tag{4.1}$$

where q/N is the constant ratio between the self-weight per unit area q and the normal force per unit length N, while $z = z(x, y)$ is the unknown scalar field, solution of the Laplace equation, that corresponds to the vertical coordinate of the bridge surface.

Neglecting the self-weight and assuming $q/N = 0$, Musmeci set the homogeneous form of Equation (4.1). He solved it using harmonic functions, that approximate minimal surfaces when the gradient is small enough, under the hypothesis of boundary conditions equal to the ones adopted in the soap bubble model. Musmeci illustrated his solution in the diagram

shown in Figure 4.5a, focusing again on the lower section of the bridge. In Figure 4.5b the diagram generated implementing the Laplace equation in the simulation software COMSOL Multyphisics is shown. Comparing the two figures, similar results can be observed.

(a) *Musmeci's solution [76]*   (b) *Solution in COMSOL Multyphisics*
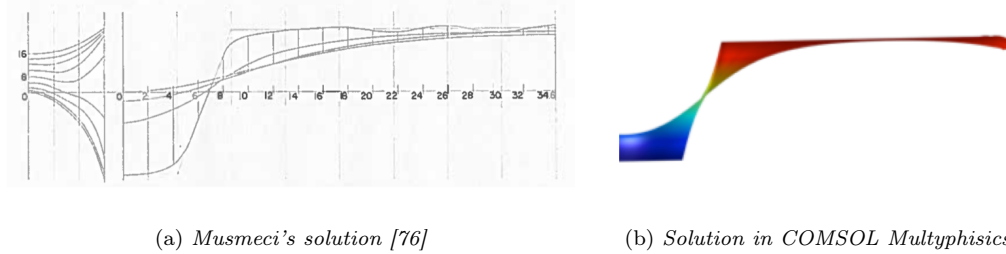
Figure 4.5: Geometry of the lower section of the Basento bridge generated using the approximated Laplace equation

Following the first two steps, an isotropically stressed minimal surface with continuous boundary conditions was obtained by the Italian engineer [76]. However he deemed the geometry not curved enough to follow the flow of forces through the structure according to the load applied. In fact in the constructed bridge, the boundary conditions are different from the ones assumed initially by Musmeci. The shell picks up the deck at selected points, not continuously. Solving the Laplace equation with this new assumption yields the surface geometry shown in Figure 4.6a to the one of Figure 4.6b, more similar to the final solution.

(a) *Continuous supports*   (b) *Punctual supports*
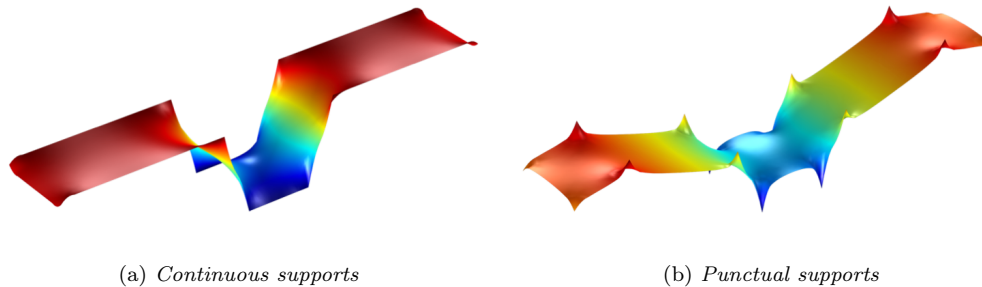
Figure 4.6: Geometry of the Basento bridge obtained applying the Laplace equation in COMSOL Multyphisics

Unfortunately a simulation software was not available at that time, therefore Musmeci decided to realize a second physical model using a 0.8 mm thick neoprene rubber [17, 18]. The 1:100 scale neoprene model is shown in Figure 4.7. The stresses were introduced into the flexible neoprene fabric by tensile pulling forces applied at the connection points as shown in Figure 4.7. The pulling forces had the same orientation but opposite direction with respect to the loads transfer from the deck to the underlying shell.

The surface given by the neoprene model was no longer an isotropic minimal surface. In order to achieve the curvatures Musmeci desired, the pre-stresses applied in the longitudinal direction of the bridge were three times larger than those in the traverse direction [76].

Once Musmeci achieved a satisfying shell shape, he wanted to verify its structural feasibility. Therefore a first structural analysis was performed building the methacrylate model of the bridge shown in Figure 4.8 [99].

Like the previous neoprene model, the third physical model used by Musmeci was at a
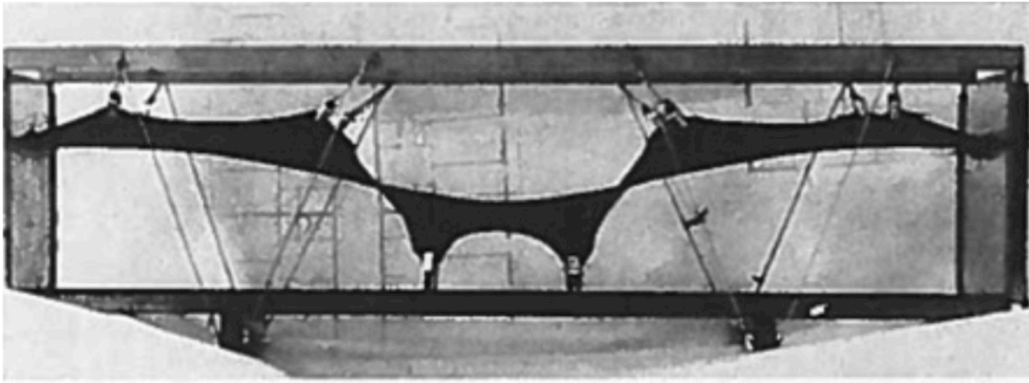
Figure 4.7: Musmeci's neoprene mechanically pre-stressed form finding model of the Basento bridge [76]

scale of 1:100. Upon loading the model, strain measurements of the shell were taken using electrical strain gauges. The associated shell stresses were then evaluated [17, 18]. The loads considered by Musmeci included permanent loads, but also asymmetric loading due to the vehicular traffic.
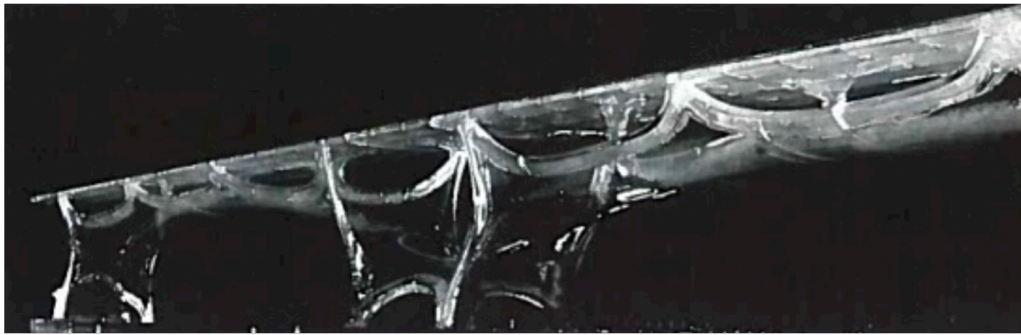
(a) *3D view*

(b) *Front view*

Figure 4.8: Musmeci's methacrylate model for the Basento bridge [76, 99]

Nowadays this step could be replaced by a structural analysis performed on a FE model of the bridge, as the one presented in Section 4.3. Musmeci did not have analogous tools available, but he was convinced of the importance of ensuring the good performance of the form-found shell before moving on in the design process.

Following the fourth step, Musmeci performed an additional structural analysis using a 2D analytical beam model. Again, the aim was to review the structural feasibility of the

form-found shell computing the internal forces and, consequently, calculating the thickness of the bridge sections. Unfortunately there is no record of the model employed, but Musmeci's writings suggest it might be an Euler-Bernouilli beam model [76].

At this point Musmeci was convinced that the form-found shell could work structurally and be translated in an actual design solution for the Basento bridge. However the use of physical models was suitable for a preliminary design only. As seen in Chapter 3, physical models are time-consuming to construct and to alter. Furthermore, once the shape has been generated, measuring the exact geometry may be a real challenge. Small errors in the geometry acquisition could lead to significant errors in the full scale structure. Especially when considering a shell surface working mainly through membrane action, any deviation from the exact geometry could result in undesirable bending moments under the applied loadings. Hence Musmeci decided to implement a numerical Finite Difference form finding method. He did not leave details of the calculations computed, but the results refined and confirmed the solution derived from the previous steps.

Once the shell shape was finally defined, Musmeci performed the last structural analysis. A micro-concrete 1:10 scale model was built and tested at the Institute of Experimental Models and Structure in Bergamo, Italy funded by the Industrial Consortium of the city of Potenza [17, 18].

4.3 Revisiting the design of the Basento bridge - Force density method and Finite Element analysis

Sergio Musmeci developed the unique shape of the Basento bridge through a well-structured design process, alternating form finding techniques and structural analyses testing the structural behavior of the geometry found. The last form finding method used was a numerical Finite Difference approach impossible to accurately determine. Not enough details are left, but it is interesting to note that two of today's most common numerical form finding techniques were devised immediately before or at the time of the Basento bridge project. These methods are the Dynamic relaxation and the Force density method, both discussed in Chapter 3. The linear Force density method implemented in a Matlab code, as discussed in Section 3.4, has been chosen to generate the geometry of the Basento bridge and compare the result with Musmeci's surface.

One span of the bridge has been modeled using a quadrilateral mesh $1 \times 1\ m$. The nodes picking up the deck and the ones connected to the foundations have been restrained in the X, Y and Z directions. Different force density values have been applied in longitudinal and transverse direction following Musmeci's statement:

> "The concrete membrane has been thought as a uniformly compressed but non-isotropic surface. The compression forces were foreseen constant along longitudinal and transversal directions, but different each other. The longitudinal compression was taken three times greater than the transverse one, according to the final geometry of the bridge." (Musmeci, 1977) [76]

Instead of the 3:1 ratio indicated by Musmeci, a 4:1 ratio between the force densities has been implemented to obtain the most similar geometry to the one of the constructed shell vault. The result obtained is shown in Figure 4.9. From the coordinates of all nodes, a NURBS model has been generated to represents the form-found surface. This one has been imported in the software COMSOL Multiphysics to perform a FE structural analysis. The process is summarized in the flowchart in Figure 4.10.
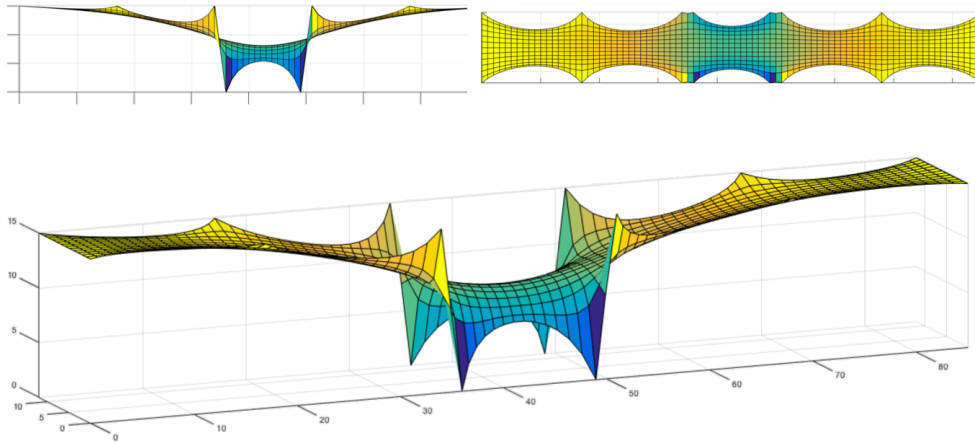
Figure 4.9: Basento bridge surface obtained applying the Force density method implemented in Matlab
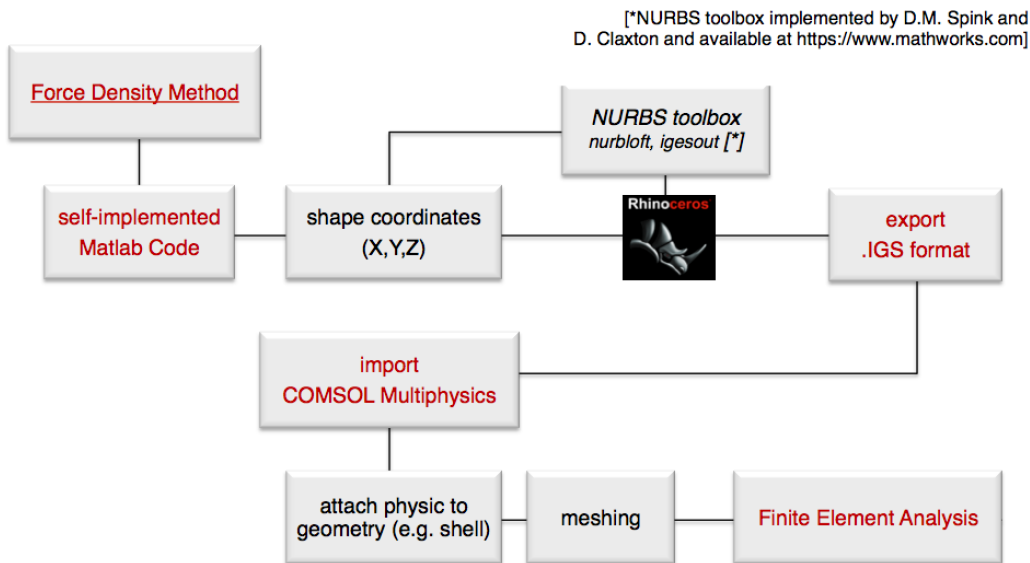
Figure 4.10: Review process of Musmeci's design for the Basento bridge

The FE model has a triangular mesh as shown in Figure 4.11. A reinforced concrete material with density equal to 23 kN/m^3 and Young's modulus equal to 25000000 kN/m^2 has been considered. The shell thickness is uniform and equal to 30 cm, that is the minimum shell thickness of the constructed bridge. The loading transferred from the deck to the underlying shell structure has been applied in the nodes located in correspondence of the shell-deck connections. Results of the FE linear elastic analysis are shown in Figure 4.12. Tensile stresses, represented by the empty areas, can be observed in both directions. Hence the shell surface is not fully compressed as wished by Musmeci. In fact, in the application of the physical and numerical form finding techniques, he did not consider the self-weight of the shell but only the one transferred by the deck. When additional loads not considered during the form finding procedure are applied to the shell structure, bending moments arise
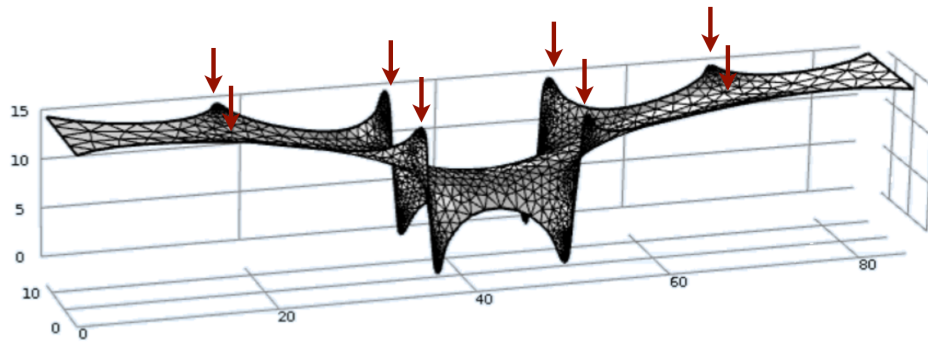
Figure 4.11: Finite Element model of the Basento bridge

and a funicular behavior cannot be guaranteed. Furthermore, additional constraints occurred during the construction phase inducing Musmeci to increase the shell vault thickness up to 120 *cm* in specific location such as the edges [47, 76], as can be observed in Figures 4.13 and 4.14. Nevertheless, the compressed area of the shell is substantially larger than the tensile one, suggesting that Musmeci's shape, even if not perfectly optimized, can still be interpreted as a good starting point. Musmeci's principle of considering the shape as an unknown variable and the design procedure he followed are still valid.
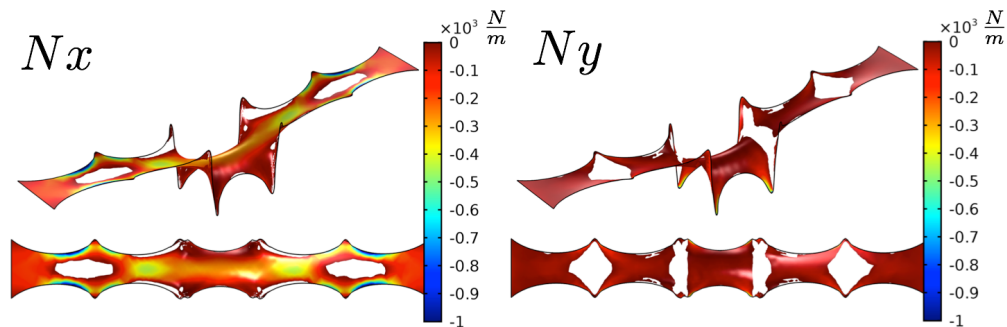
Figure 4.12: Finite Element linear elastic analysis - Axial forces acting on the Basento bridge

A non linear iterative procedure of shape optimization carried out with contemporary computational tools could certainly refine the design solution obtained by the Italian engineer. However the output is not unique. As seen in Chapter 2, multiple load paths are possible and different shell geometries can function in compression under the applied loadings. The choice can be finalized adding further constraints such as Musmeci's will to have different curvatures in the longitudinal and transverse direction.

The research of the "right" shape accompanied Sergio Musmeci along all his career. His ability to experiment combining physical models and complex calculations, intuition and theory, architecture and engineering makes him a unique non-conformist character of his time [47]. In the design of the Basento Bridge, he could not achieve the ideal funicular behavior he was pursuing. However, when designing shell structures, many designers could find themselves in the same situation faced by Musmeci choosing to adopt a shell shape not ideally funicular, but funicular "enough". In these circumstances, the request of an instrument able to quantify the funicularity arises. A new method aiming to meet this need is proposed in Chapter 5.

Figure 4.13: Under deck detail of the Basento bridge [via wikiarquitectura.com]

Figure 4.14: Shell detail of the Basento bridge [PC: Henri Cartier-Bresson]

Chapter 5

Relaxed Funicularity Ellipse Method

Funicular systems adopt the "right" shape in accordance with the applied load and are ideally able to act without introducing bending. As a result their thickness can be minimized and the amount of material reduced. When designing shell structures, designers pursue solutions characterized by efficiency and optimization but an ideal funicular behavior is sometimes impossible to achieve due to multiple design constraints. However when this is the case and bending moments cannot be avoided, a shell can still be considered "more or less funicular". In fact in term of stresses and structural performance, there is a substantial difference if the bending moments give a contribution much smaller than that of the membrane forces or if the two contributions are comparable. This topic is extensively discussed in Section 5.1. Section 5.2 presents an effective and easy-to-read new method to study and quantify the funicularity. The classical funicularity concept has been extended to the one of Relaxed Funicularity, based on a generalized definition of eccentricity. The rationale of the method proposed, together with the mathematical formulation and a proper graphical representation, is discussed. The method has been applied to form-found shell structures analyzed under different static loads. In Section 5.3 the form finding approach and the numerical model used are detailed. Section 5.4 is devoted to the discussion of the parametric numerical study and the observed results.

5.1 Funicularity evaluation

When no-bending occurs, the shape is determined by forces and vice versa. This is valid for 1D shapes, but it can be interpreted differently for shells. In theory, as anticipated in Chapter 2 and confirmed by different authors, a shell properly supported can carry any load by membrane action only.

Belluzzi declares that:

> "The behavior of a membrane differs from that of a cable.[....]The membrane is always in equilibrium for every external force and irrespective of its initial shape, and this equilibrium is satisfied solely by means of the internal membrane forces." (Belluzzi, 1982) [6]

In Pizzetti et al. it is stated that:

> "From a theoretical point of view, one could expect to oppose any curved thin surface to any load, confident that this surface will organize to perform statically at its best, that is a bending-free behavior." (Pizzetti et al., 1980) [87]

However bending-free behavior is only valid under two assumptions: the boundary conditions are congruent with the shape considered and the load applied, and the ratio between membrane stiffness and flexural stiffness tends to infinity; therefore a pure membrane model is applicable. In this circumstance the structure is locally isostatic and the equilibrium equations seen in Section 2.3.1 can be solved directly.

In practice, however, matters may not be so simple. Calladine confirms that:

"For a membrane, the nature of the solution may depend on the shape of the shell surface and the nature of the boundary conditions." (Calladine, 1983) [14]

Summarizing for a given shape and load, a funicular behavior can be found assigning the right boundary conditions to the shell analyzed; otherwise, for a given load and boundary conditions, the right shape needs to be found in order to obtain a no-bending behavior. Hence defining the "right" shape becomes crucial and several form finding approaches can be used for this purpose. Furthermore, when designing an actual surface, an elastic shell problem has to be solved: the flexural stiffness starts playing a role and the problem becomes hyperstatic. Bending moments, even if minimal, will arise. This also happens for form-found shell surfaces when the thickness increases and consequently the ratio between membrane stiffness and flexural stiffness decreases.

As seen in Chapter 4, in the design of the Basento bridge, when applying the form finding methods seeking the shell shape that could guarantee an ideal membrane behavior, Musmeci did not include all loads acting on the structure. If additional loads not considered during the form finding procedure are then applied to the shell, bending moments appear. The mutual dependency between shape and applied load leads to the common criticism made on the effective application of form finding methodologies; they can be suited to preliminary design, but the research of the shape cannot be generalized when the relevant load cases are multiple, since no-bending behavior cannot be guaranteed for all of them [1]. When this is the case and bending moments cannot be avoided, can the shell be still considered funicular? An answer to this question is given introducing a *relaxed* definition of the term funicularity. Surely, in term of stresses and structural performance, there will be a difference if the bending moments give a contribution much smaller than that of the membrane forces or if the two contributions are comparable.

From these considerations, the need to assess if a structural shape is more or less funicular arises, as well as the idea that an instrument able to quantify the funicularity could be helpful to judge the global design of a shell.

An interesting example of redefinition of funicular arches, whose initial shape is not funicular under given applied loads and boundary conditions, can be found in [104], where the funicularity is recovered by an optimized system of post-tensioning cables. The cited work is limited to 1D structures.

A useful parameter to define the condition of funicularity in arch strucures is the eccentricity associated to the normal force and related to the bending moment acting on a section. This parameter could be used also for shell structures by defining a proper generalization of it. To the author's knowledge, the first ones to use eccentricity as a parameter to quantify the funicularity of optimized shells are Marino et al. [65]. Marino calculates the eccentricity for a shell as the ratio between the norm of the moment matrix and the one of the membrane force matrix, stating that this value tends to zero when the behavior is membrane dominated. Earlier Lucchesi et al. [63, 64] proposed a numerical method allowing for analyzing masonry vaults, where the calculation of the maximum modulus eccentricities surface (MMES) has been proposed in the context of no-tension materials, as a tool for limit analysis.

5.2 Relaxed Funicularity Ellipse Method

In order to assess if a structural shape is more or less funicular, a method named *Relaxed Funicularity (RF) Ellipse Method* is proposed.

As seen in Section 5.1, other authors have used the eccentricity as a parameter to quantify the funicularity [63, 64, 65]. The method presented in this work aims at generalizing these procedures obtaining a quick and easy-to-read graphical feedback on the structural behavior of the shape analyzed.

As shown in Figure 5.1, given a shell surface S, every point P on it has a local orthonormal basis $\mathbf{a}_1,\mathbf{a}_2$, $\mathbf{a}_3$ where local $\mathbf{a}_1,\mathbf{a}_2$ vectors lie in the tangent plane to the surface at the point considered and $\mathbf{a}_3$ is the normal to the tangent plane.
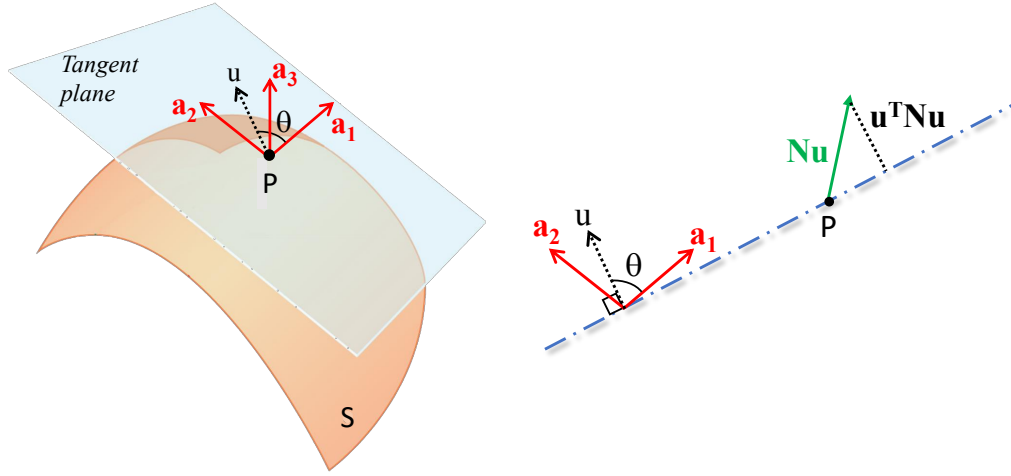
Figure 5.1: Surface with local basis and projection of internal forces

Following the evaluation of the membrane forces and bending moments acting on a shell, one can write the associated local tensors $\mathbf{N}$ and $\mathbf{M}$ respectively:

$$\mathbf{N} = \begin{pmatrix} N_{11} & N_{12} \\ N_{12} & N_{22} \end{pmatrix} \qquad \mathbf{M} = \begin{pmatrix} M_{11} & M_{12} \\ M_{12} & M_{22} \end{pmatrix} \tag{5.1}$$

Let $\mathbf{u}$ be a unit vector lying on the tangent plane and represented in the base $\mathbf{a}_1,\mathbf{a}_2$ as follows:

$$\mathbf{u} = \begin{pmatrix} \cos(\theta) \\ \sin(\theta) \end{pmatrix} \tag{5.2}$$

where the angle $\theta \in [0, \pi]$ is calculated between $\mathbf{u}$ and $\mathbf{a}_1$.

The normal force $N(\theta)$ acting along the direction $\mathbf{u}$ and the bending moment $M(\theta)$ acting in the plane $(\mathbf{u}, \mathbf{a}_3)$ can be evaluated as the quadratic forms:

$$N(\theta) = \mathbf{u}^\mathrm{T}\mathbf{N}\mathbf{u} \qquad\qquad M(\theta) = \mathbf{u}^\mathrm{T}\mathbf{M}\mathbf{u} \tag{5.3}$$

The eigenvalue problem related to each quadratic form and solved separately for $\mathbf{N}$ and $\mathbf{M}$ gives the eigenvalues of Equations (5.4) and (5.5) (principal normal forces and principal moments respectively), and the corresponding eigenvectors (principal directions):

$$N_{\min}^{\max} = \frac{\mathrm{Tr}(\mathbf{N})}{2} \mp \frac{\sqrt{\mathrm{Tr}(\mathbf{N})^2 - 4\det(\mathbf{N})}}{2} = \bar{N} \mp \sqrt{N_{12}^2 + \widehat{N}^2} \tag{5.4}$$

$$M^{\max}_{\min} = \frac{\mathrm{Tr}(\mathbf{M})}{2} \mp \frac{\sqrt{\mathrm{Tr}(\mathbf{M})^2 - 4\det(\mathbf{M})}}{2} = \overline{M} \mp \sqrt{M_{12}^2 + \widehat{M}^2} \qquad (5.5)$$

where $\bar{N} = \frac{N_{11}+N_{22}}{2}$, $\widehat{N} = \frac{N_{11}-N_{22}}{2}$, $\overline{M} = \frac{M_{11}+M_{22}}{2}$, $\widehat{M} = \frac{M_{11}-M_{22}}{2}$.

Because $\mathbf{N}$ and $\mathbf{M}$ are 2D tensors and unit norm eigenvectors are considered, each eigenvector can be represented by a value of θ. It is worth to note that, apart from specific conditions of symmetry (e.g. axial symmetric vaults under axial symmetric load conditions), eigenvectors of $\mathbf{N}$ do not coincide with eigenvectors of $\mathbf{M}$. This can be verified by the condition that the two tensors, in general, do not commute: $\mathbf{NM} \neq \mathbf{MN}$.

Each 2×2 matrix $\mathbf{A}$ can be uniquely decomposed in a spherical $\mathrm{Sph}(\mathbf{A}) = \mathrm{Tr}(\mathbf{A})/2\,\mathbf{I}$ and deviatoric component $\mathrm{Dev}(\mathbf{A}) = \mathbf{A} - \mathrm{Sph}(\mathbf{A})$. Moreover, it is important to say that eigenvectors of $\mathbf{A}$ coincide with the eigenvectors of $\mathrm{Dev}(\mathbf{A})$.

The following notation for the spherical (Sph) and deviatoric (Dev) components of $\mathbf{N}$ and $\mathbf{M}$ is introduced:

$$\mathbf{N} = \bar{N} \begin{pmatrix} 1 & 0 \\ 0 & 1 \end{pmatrix} + \begin{pmatrix} \widehat{N} & N_{12} \\ N_{12} & -\widehat{N} \end{pmatrix} = \mathrm{Sph}(\mathbf{N}) + \mathrm{Dev}(\mathbf{N}) \qquad (5.6)$$

$$\mathbf{M} = \overline{M} \begin{pmatrix} 1 & 0 \\ 0 & 1 \end{pmatrix} + \begin{pmatrix} \widehat{M} & M_{12} \\ M_{12} & -\widehat{M} \end{pmatrix} = \mathrm{Sph}(\mathbf{M}) + \mathrm{Dev}(\mathbf{M}) \qquad (5.7)$$

With the given notation, it is possible to define the *generalized eccentricity* $e(\theta)$ of the normal force along the direction $\mathbf{u}$ [64]:

$$e(\theta) = \frac{M(\theta)}{N(\theta)} \qquad (5.8)$$

This generalized eccentricity will be used to define the Relaxed Funicularity.

5.2.1   Relaxed Funicularity

Using the trigonometrical identities:

$2\sin(\theta)\cos(\theta) = \sin(2\theta)$ and $\cos^2(\theta) = \frac{1+\cos(2\theta)}{2}$, $\sin^2(\theta) = \frac{1-\cos(2\theta)}{2}$, $\alpha = 2\theta$,

Equation (5.3) can be written explicitly as:

$$\begin{cases} N(\alpha) = \bar{N} + \widehat{N}\cos(\alpha) + N_{12}\sin(\alpha) \\ M(\alpha) = \overline{M} + \widehat{M}\cos(\alpha) + M_{12}\sin(\alpha) \end{cases} \qquad (5.9)$$

The *generalized eccentricity* represented by Equation (5.8) can reparametrized as $e(\alpha) = \frac{M(\alpha)}{N(\alpha)}$.

Equation (5.9) can be written in matrix form:

$$\begin{pmatrix} N(\alpha) \\ M(\alpha) \end{pmatrix} = \begin{pmatrix} \bar{N} \\ \overline{M} \end{pmatrix} + \begin{pmatrix} \widehat{N} & N_{12} \\ \widehat{M} & M_{12} \end{pmatrix} \begin{pmatrix} \cos(\alpha) \\ \sin(\alpha) \end{pmatrix}. \qquad (5.10)$$

Equation (5.10) represents a parametric curve in the plane $(N, M) \equiv \mathbb{R}^2$, in particular it represents the equation of an ellipse when α ranges between 0 and 2π. The example of a possible ellipse is depicted in Figure 5.2. Every point of the shell surface is endowed of such an ellipse, whose values are the couples (N, M) acting along the direction α.

As discussed in the introduction, an attempt to give a *relaxed* definition of the funicularity is made. A 1D structure (e.g. an arch) is defined funicular, for a given load and boundary condition, if the eccentricity $e = M/N = 0$ for each point of the curve. Such a definition,

once extended to 2D structures, should correspond to require that $e(\alpha) = 0 \,\forall \alpha \in [0, 2\pi]$ for each point of the surface. In practical cases this will never happen, because of the intrinsic coupling between membrane and bending behavior in shells, then a *relaxed* concept of funicularity should be given. The term *relaxed* is used to mean that a structure can be still considered funicular, also for $M(\alpha) \neq 0$, whenever $e(\alpha)$ is included into an admissibility interval. The admissibility interval has been set as $[-\lambda h, \lambda h]$, being h the thickness of the shell, and $\lambda \in [0, 1/2]$ a suitable admissibility coefficient that depends on the applications. For example $\lambda = 1/2$ means that $e(\alpha)$ is admissible if $N(\alpha)$ lies inside the thickness of the shell, while $\lambda = 1/6$ means that $e(\alpha)$ is admissible if, supposing a linear elastic response of the material, the section is fully compressed or fully stretched (this last example can be viewed as generalization of the middle third criterion used for compressed arches).
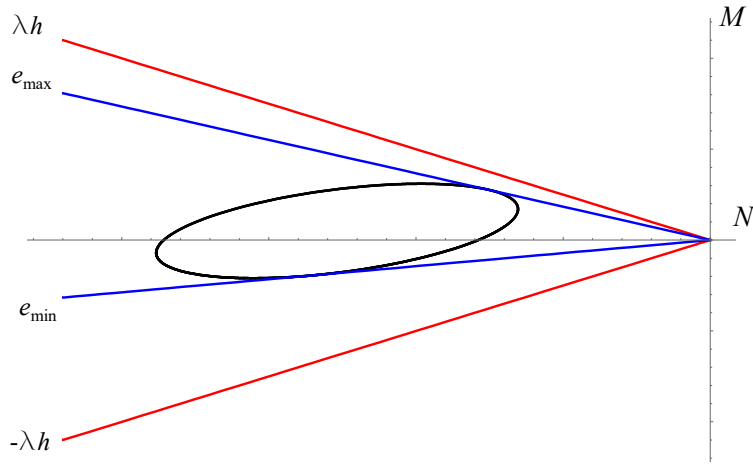
Figure 5.2: Ellipse of eccentricity or Relaxed Funicularity (RF) ellipse [The maximum and minimum eccentricity are equal to the slope of the upper and lower blue lines respectively, the limits λh and $-\lambda h$ are equal to the slope of the red lines, being h the thickness of the shell, and $\lambda \in [0, 1/2]$ a suitable admissibility coefficient that depends on the applications.]

Hence the following definition for Relaxed Funicularity (RF) is given: a shell is R-Funicular if $e(\alpha) \in [-\lambda h, \lambda h] \forall \alpha \in [0, 2\pi]$, for each point of the surface.

In practice the problem of the R-Funicularity is that of verifying:

$$[\min(e(\alpha)), \max(e(\alpha))] \subset [-\lambda h, \lambda h] \qquad (5.11)$$

Equation (5.11) is suitable for an interesting graphical representation, as pictured in Figure 5.2 where, recalling the definition of the generalized eccentricity $e(\alpha)$, and given a certain angle $\bar{\alpha}$, the eccentricity $e(\bar{\alpha})$ is the slope of the straight line that starts from the origin and intersects the ellipse in $(N(\bar{\alpha}), M(\bar{\alpha}))$ and can be evaluated as:

$$e(\bar{\alpha}) = \frac{M(\bar{\alpha})}{N(\bar{\alpha})} = \frac{\overline{M} + \widehat{M}\cos(\bar{\alpha}) + M_{12}\sin(\bar{\alpha})}{\overline{N} + \widehat{N}\cos(\bar{\alpha}) + N_{12}\sin(\bar{\alpha})}. \qquad (5.12)$$

The slope of the blue lines tangent to the ellipse represents maximum and minimum eccentricities ($e_{\max}$ and $e_{\min}$ respectively), while the one of the red lines represents the limiting values of the eccentricities, taken equal to λh. The section of the surface, in this example, is fully compressed (negative values of the N axis) as the $e_{\max}$ and $e_{\min}$ lines are included in

the limit lines $\pm\lambda h$. This also corresponds to the ellipse fully included in the given limits. In this respect the ellipse itself is a graphical representation of the R-Funicularity and it will be also denoted as *RF-ellipse*. It is relevant to note that the more the RF-ellipse is next and flattened to the N axis, the lower is the eccentricity: in the point analyzed, the surface will be mainly stretched and the bending moments would be reduced.

In general, in order to discuss the problem of minimum and maximum eccentricities, the evaluation of the critical points of the Equation (5.12) must be performed.

In most cases, the values obtained for $e_{\min}^{\max}$ give a direct quantification of how much the shell is affected by the internal moments with respect to the membrane forces. The higher the values of the eccentricities, the lower will be the capability of the shell of carrying the applied loads by means of the sole membrane forces. Zero values of the extrema of the eccentricities means that the shape of the shell can be considered fully funicular. In reality this last condition is almost never satisfied, and one of the goal of the presented method is also to allow for an assessment of how much a form-found shell can be considered R-Funicular.

5.2.2   RF-ellipse and bounding box

Looking at Equation (5.10), the right hand side is characterized by two terms. The first term $(\bar{N}, \bar{M})$ does not depend on α and gives the center of the RF-ellipse. Note that $(\bar{N})$ and $(\bar{M})$ are the mean values of $\mathbf{N}$ and $\mathbf{M}$ and are associated to the spherical components $\mathrm{Sph}(\mathbf{N})$ and $\mathrm{Sph}(\mathbf{M})$ as defined in (5.6) and (5.7). The second term of the equation is given by the square matrix $\mathbf{D} = [(\widehat{N}, N_{12}), (\widehat{M}, M_{12})]$ containing, by row, the components of the deviatoric parts $\mathrm{Dev}(\mathbf{N})$ and $\mathrm{Dev}(\mathbf{M})$, respectively. This matrix multiplies the unit vector $(\cos(\alpha), \sin(\alpha))$, by transforming (for $\alpha \in [0, 2\pi]$) a unit circumference in an ellipse. Hence the *position* of the RF-ellipse is given by $\mathrm{Sph}(\mathbf{N})$ and $\mathrm{Sph}(\mathbf{M})$ while the *shape* of the RF-ellipse is given by the $\mathrm{Dev}(\mathbf{N})$ and $\mathrm{Dev}(\mathbf{M})$.

The following special cases can be emphasized:

1. The RF-ellipse is *centered* in $(0,0) \iff \mathrm{Sph}(\mathbf{N}) = \mathrm{Sph}(\mathbf{M}) = \mathbf{0}$;

2. The RF-ellipse is a *point* $\iff \mathrm{Dev}(\mathbf{N}) = \mathrm{Dev}(\mathbf{M}) = \mathbf{0}$;

3. The RF-ellipse is a *circumference* $\iff \mathbf{D}^{\mathrm{T}}\mathbf{D} = r^2\mathbf{I}$, where $r \in \mathbb{R}$ is the radius of the circle;

4. The RF-ellipse is a *straight line* $\iff \det(\mathbf{D}) = 0$;

5. The RF-ellipse is a *straight line passing through the origin* $\iff \mathbf{M} = e\mathbf{N}$, where $e \in \mathbb{R}$.

The first two cases are trivial: in the first one the mean values $\bar{N}$ and $\bar{M}$ vanish and the RF-ellipse is centered in the origin; the second one represents the case in which both $\mathbf{N}$ and $\mathbf{M}$ are isotropic. The third case has an interesting mechanical interpretation. In fact:

$$
\begin{aligned}
\mathbf{D}^{\mathrm{T}}\mathbf{D} = r^2\mathbf{I} \implies (\widehat{N}, N_{12}) \cdot (\widehat{M}, M_{12}) = 0 \\
(\widehat{N}, N_{12}) \cdot (\widehat{N}, N_{12}) = (\widehat{M}, M_{12}) \cdot (\widehat{M}, M_{12}) = r^2
\end{aligned}
\tag{5.13}
$$

These implications can be summarized as follows $\mathrm{Dev}(\mathbf{N}) \cdot \mathrm{Dev}(\mathbf{M}) = 0$ and $\|\mathrm{Dev}(\mathbf{N})\| = \|\mathrm{Dev}(\mathbf{M})\|$, i.e. $\mathrm{Dev}(\mathbf{N})$ and $\mathrm{Dev}(\mathbf{M})$ are orthogonal with respect to the dot product between square matrices, and they have the same norm.

It is possible to demonstrate that the first property means that the principal directions of the two matrices are mutually rotated of $\pi/4$. Then one can state: *the RF-ellipse is a circumference if and only if the principal directions of* $\mathbf{M}$ *are rotated by* $\pi/4$ *w.r.t. the principal directions of* $\mathbf{N}$ *and* $M_{max} - M_{min} = N_{max} - N_{min}$. The last two special cases are the most significant from a mechanical point of view.

In particular the condition $\det(\mathbf{D}) = 0$ leads to an important consequence:

$$\det(\mathbf{D}) = \det\left(\begin{array}{cc} \widehat{N} & N_{12} \\ \widehat{M} & M_{12} \end{array}\right) = 0 \implies \frac{\widehat{M}}{\widehat{N}} = \frac{M_{12}}{N_{12}} \tag{5.14}$$

This means that $\mathrm{Dev}(\mathbf{M}) \propto \mathrm{Dev}(\mathbf{N})$ and implies that eigenvectors of $\mathbf{M}$ coincide with eigenvectors of $\mathbf{N}$ (i.e. the principal directions of $\mathbf{M}$ are equal to the principal directions of $\mathbf{N}$). Then one can state: *the RF-ellipse is a straight line if and only if the principal directions of $\mathbf{M}$ are equal to the principal directions of $\mathbf{N}$*. If the straight line crosses the origin (last case itemized as 5), it means that $\mathbf{M} \propto \mathbf{N}$, so that the eccentricity does not depends on α, and corresponds to the unlikely case of constant eccentricity along each direction.

Mechanical interpretation of the shape of RF-ellipse

The shape of any RF-ellipse is dependent on the principal directions of the $\mathbf{N}$ and $\mathbf{M}$ tensors; this concept can be generalized defining a *bounding box* in which the RF-ellipse is inscribed. The idea of the bounding box directly follows by noting that $\mathbf{N}$ ranges in $(\bar{N} - \frac{\Delta N}{2}, \bar{N} + \frac{\Delta N}{2})$ and $\mathbf{M}$ ranges in $(\bar{M} - \frac{\Delta M}{2}, \bar{M} + \frac{\Delta M}{2})$, being ΔN and ΔM the side dimensions of a rectangular box in the (N, M) space, and defined by the principal values of $\mathbf{N}$ and $\mathbf{M}$ as following:

$$\begin{aligned} \Delta N = (N_{\max} - N_{\min}) = 2\sqrt{N_{12}^2 + \widehat{N}^2} \\ \Delta M = (M_{\max} - M_{\min}) = 2\sqrt{M_{12}^2 + \widehat{M}^2} \end{aligned} \tag{5.15}$$

From a geometrical point of view the RF-ellipse and the corresponding bounding box can be drawn following the next steps:

1. Draw the *center* of the ellipse $(\bar{N}, \bar{M})$ (note that it depends only on the spherical components).

2. Draw around the center the *bounding box* in which the ellipse will be inscribed. This box has dimensions given in Equation (5.15), and it is worth noting that the box dimensions depend on the norm of the deviatoric components.

3. Draw along each side of the bounding box the *four points* that are *tangent* to the ellipse. The coordinates of these points are given by as follows:

$$\begin{aligned} P_1 &\left(N_{\min}, \bar{M} - \Delta M \cos 2\beta\right) & P_2 &\left(N_{\max}, \bar{M} + \Delta M \cos 2\beta\right) \\ P_3 &\left(\bar{N} - \Delta N \cos 2\beta, M_{\min}\right) & P_4 &\left(\bar{N} + \Delta N \cos 2\beta, M_{\max}\right) \end{aligned}$$

being β the angle that the principal directions of $\mathbf{M}$ form with the principal directions of $\mathbf{N}$.

4. Draw the ellipse passing through the four points $\{P_1, P_2, P_3, P_4\}$.

At this stage some specific cases, pictured in Figure 5.3, can be discussed. When $\beta = 0$ the principal directions of $\mathbf{M}$ and $\mathbf{N}$ coincide, and the RF-ellipse degenerates in one of the diagonals of the bounding box (Fig. 5.3a). This means that the limit eccentricities could be simply calculated by the ratios $e_{\min}^{\max} = M_{\min}^{\max}/N_{\min}^{\max}$, and that their directions coincide with that of principal section forces. As one can see from Figure 5.4a, N, M and e have maximum and minimum values at the same α.

On the opposite, when $\beta = \pi/2$ the ellipse degenerates in the second diagonal of the bounding box (Fig. 5.3.b). As one can see from Figure 5.4b, the limit eccentricities are given

by $e_{\min}^{\max} = M_{\min}^{\max}/N_{\max}^{\min}$, and their directions coincide with those of principal moments (M and e have maximum value when N is minimum and vice versa).

When $\beta = \pi/4$, see (Fig. 5.3c), the ellipse reaches the maximum area, passing through the four midpoints of the bounding box sides. Figure 5.3d represent a generic ellipse for other β values.

(a) $\beta=0$

(b) $\beta = \pi/2$

(c) $\beta = \pi/4$

(d) *Others* β
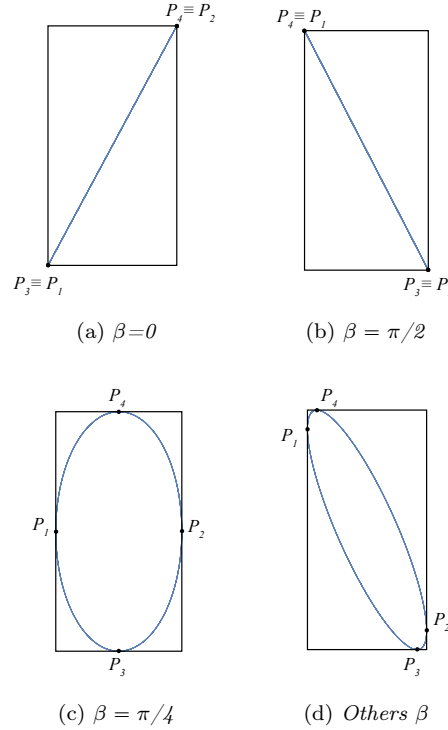
Figure 5.3: Bounding boxes and related RF-ellipses

(a) $\beta=0$

(b) $\beta = \pi/2$
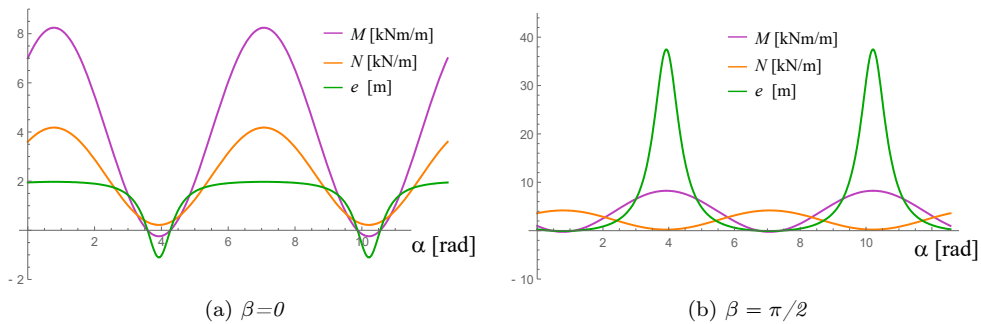
Figure 5.4: Values of N, M and e varying with α

5.2.3   Algorithm for principal eccentricities

Once the ellipse is drawn, the eccentricity can be evaluated as the slope of the straight lines joining the origin with each point of the ellipse, as indicated in Figure 5.5. The slopes of the

red lines are the maximum and minimum eccentricity or *principal eccentricities*: cases (a) and (b) show two examples of ellipse inside the limit values (blue lines) and outside of them, a RF-ellipse and a *non* RF-ellipse respectively; ellipses (c) and (d) share the same bounding box, located at the same point of the graph, but it is interesting to note that, according to β, the one in Figure 5.5c is a RF-ellipse (included in the limit values), while in the other (Fig. 5.5d) the maximum eccentricity exceeds the limit imposed, so as the ellipse is not RF.
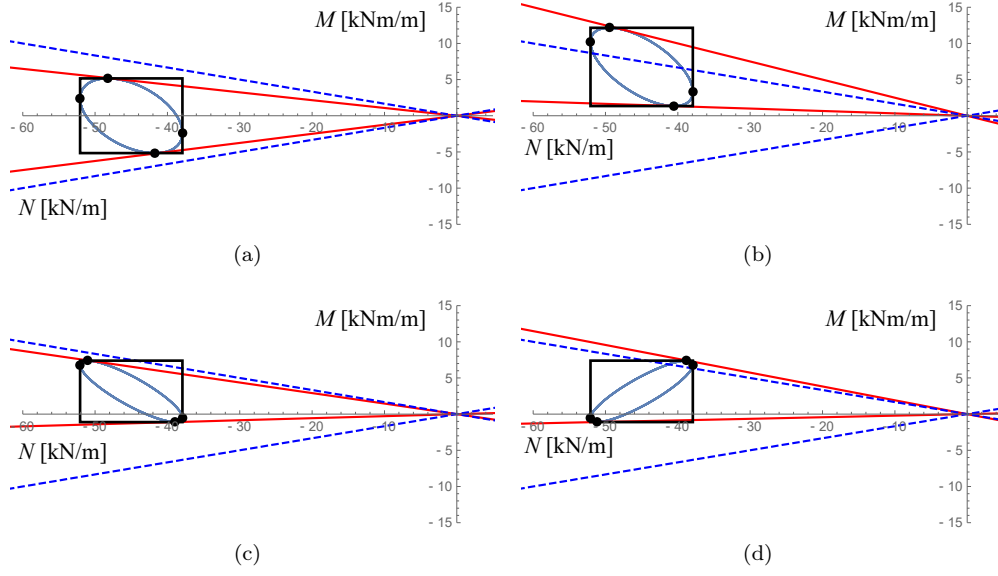
Figure 5.5: Examples of RF-ellipses and non RF-ellipses with related bounding boxes

To evaluate if an eccentricity ellipse is Relaxed Funicular or not, then the admissibility of e inside given limits $[-\lambda h, \lambda h]$ need to be tested, hence one needs to quantify $[\min(e(\alpha)), \max(e(\alpha))]$. Following Lucchesi et al. [64, 63] and from Equations (5.3) and (5.8), e is defined as the Rayleigh quotient:

$$e = \frac{\mathbf{u}^{\mathrm{T}}\mathbf{M}\mathbf{u}}{\mathbf{u}^{\mathrm{T}}\mathbf{N}\mathbf{u}},$$

corresponding to the generalized eigenvalue problem:

$$(\mathbf{M} - e\mathbf{N})\mathbf{u} = 0 \tag{5.16}$$

The eigenvalues are given by the following equation:

$$e^{max}_{min} = \begin{cases} \text{(a) } \frac{\mathrm{Tr}(\mathbf{N}^{-1}\mathbf{M}) \mp \sqrt{\mathrm{Tr}(\mathbf{N}^{-1}\mathbf{M})^2 - 4\det(\mathbf{N}^{-1}\mathbf{M})}}{2} & \text{if } \det(\mathbf{N}) \neq 0 \\[2em] \text{(b) } \left(\frac{\mathrm{Tr}(\mathbf{M}^{-1}\mathbf{N}) \mp \sqrt{\mathrm{Tr}(\mathbf{M}^{-1}\mathbf{N})^2 - 4\det(\mathbf{M}^{-1}\mathbf{N})}}{2} \right)^{-1} & \text{if } \det(\mathbf{M}) \neq 0 \,\&\, \det(\mathbf{N}) = 0 \\[2em] \text{(c) } 0, \infty & \text{if } \det(\mathbf{M}) = \det(\mathbf{N}) = 0 \,\& \\ & \det(\mathbf{D}) \neq 0 \\[1em] \text{(d) } \mathrm{Tr}(\mathbf{M})/\mathrm{Tr}(\mathbf{N}) & \text{if } \det(\mathbf{M}) = \det(\mathbf{N}) = 0 \,\& \\ & \det(\mathbf{D}) = 0 \end{cases} \tag{5.17}$$

The four options for calculating the principal eccentricities are summarized in the algorithmic Equation (5.17), and are shown in Figure 5.6. Case (a) can be considered as the standard algorithm for calculating the principal eccentricities [63]. Here also singular cases are considered for completeness.
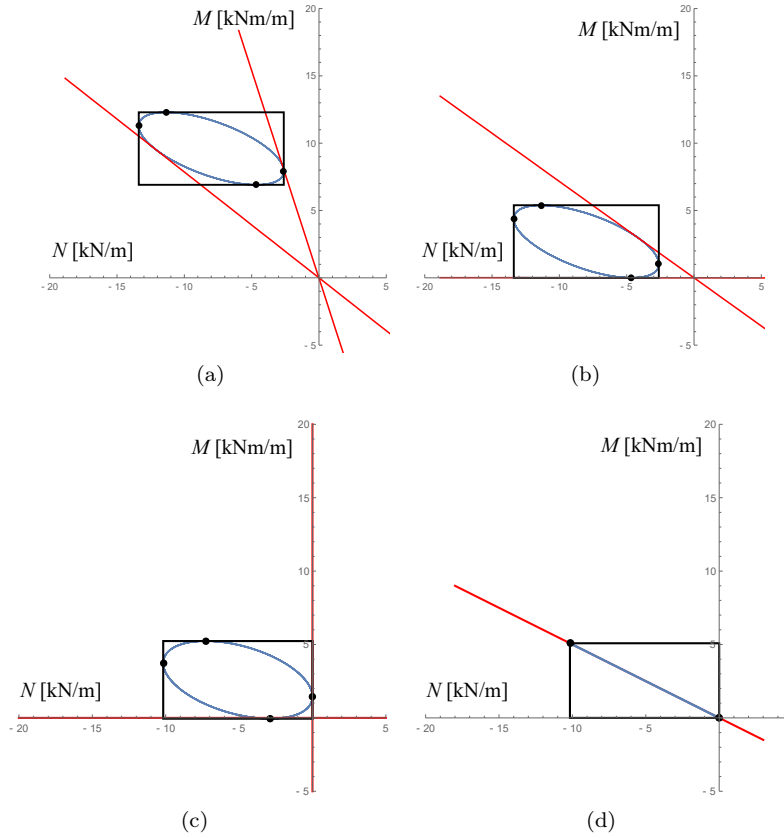
Figure 5.6: Maximum and minimum eccentricities

Cases from (b) to (d) should be considered *singular*, in fact when $\mathbf{M}$ or $\mathbf{N}$ are not full rank, then some principal eccentricities are 0 or ∞ and the corresponding ellipses are tangent to the N or M axis or both of them (Fig. 5.6b and Fig. 5.6c). In the last case (d), where all the involved matrices $\mathbf{M}$, $\mathbf{N}$ and $\mathbf{D}$ are singular, then only one value for the principal eccentricity is admissible, constant in every direction (Fig. 5.6d).

Here it is worth noting that, nevertheless $\mathbf{N}$ and $\mathbf{M}$ are symmetric, but the products $\mathbf{N}^{-1}\mathbf{M}$ and $\mathbf{M}^{-1}\mathbf{N}$ are, in general, non-symmetric. This fact has two important consequences: Equation(5.17) can give complex solutions and, also in the case of real solutions, the eigenvectors of $\mathbf{N}^{-1}\mathbf{M}$ and $\mathbf{M}^{-1}\mathbf{N}$ will be, in general, not orthogonal. Hence *the directions of maximum and minimum eccentricity, in general, are not orthogonal.*

Finally it is very important to state that Equation (5.17) gives the *local extrema* of the eccentricity $e(\alpha)$ but not always are these also *global extrema*. In particular it is possible to show three different situations:

1. Equation(5.17) gives real solutions and $N(\alpha) \neq 0 \,\forall \alpha \in [0, 2\pi] \rightarrow e(\alpha)$ has local extrema

that are also *global extrema*. Refer to the black ellipses in Figure 5.7.

2. Equation(5.17) gives real solutions but $\exists \bar{\alpha} \in [0, 2\pi] \, s.t. \, N(\bar{\alpha}) = 0 \rightarrow e(\alpha)$ has local extrema that are not *global extrema*. Refer to the blue ellipses in Figure 5.7.

3. Equation(5.17) gives complex solutions $\rightarrow e(\alpha)$ does not have local extrema. Refer to the red ellipse in Figure 5.7.

These three different solutions can be easily understood looking at Figures 5.7 and 5.8.

Figure 5.7: Different examples of RF-ellipses

(a) *Refer to Black ellipses in Fig. 5.7*

(b) *Refer to Blue ellipses in Fig. 5.7*

(c) *Refer to Red ellipse in Fig. 5.7*

Figure 5.8: Values of N, M and e varying with α according to Fig. 5.7

5.3   Form-found and numerical shell models

The RF-ellipse method has been applied to different form-found structures in order to validate it, evaluate the R-Funicularity and give an initial judgment of the shell shape examined. Two typologies of surfaces have been analyzed: shells with Gaussian curvature equal to zero and shells with positiv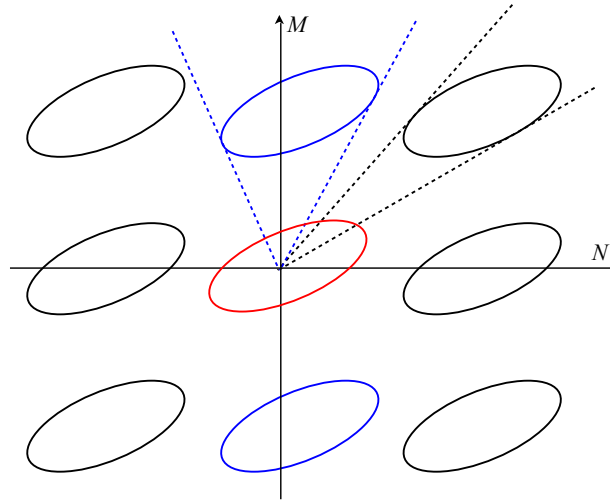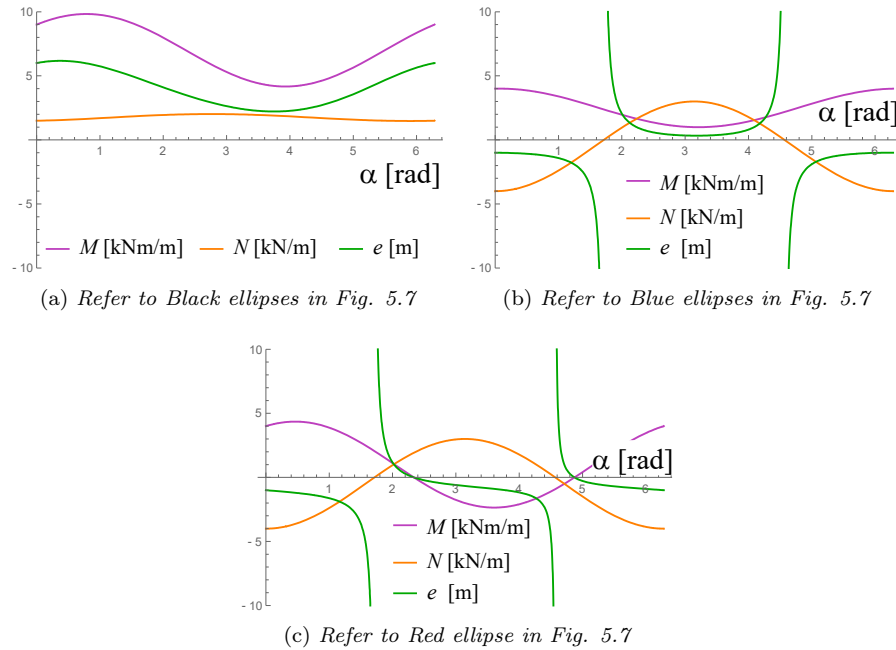e Gaussian curvature (i.e. synclastic surfaces). In all the presented analyses the limit values of the eccentricity, $\pm \lambda h$, is set by supposing a linear elastic response of the material and posing $\lambda = 1/6$ (middle third criterion).

The units of the membrane forces are expressed in force per unit length. Bending moments, usually expressed in moment per unit length, have been divided by the shell thickness in order to obtain limiting values not dependent on the shell thickness.

All form-found surfaces have been obtained using the form finding tool Kangaroo Physics developed by Daniel Piker, physics modeling plug-in of Grasshopper used together with Rhinoceros (Refer to Section 3.2). Starting from a flat mesh and defining a set of anchor points and a load distribution, Kangaroo Physics allows to find the funicular shape consistent with the conditions applied implementing the numerical form finding Particle-spring method [52]. The surface is discretized using line and joint elements; an axial spring has been assigned to every line setting the value of the stiffness. The at rest length of the lines is equal to 1.0 m. The form-found shape is obtained applying a given load and will be funicular (purely in tension) under it and anti-funicular (purely in compression) under this same load applied with equal distribution but opposite sign.

Following the form finding procedure, all discretized shell shapes have been imported and analyzed in the commercially available FE software SAP2000 [22]. The mesh, consistently with the form-found surfaces, is equal to 1×1 m and thin shell element formulation has been used. The shells are analyzed considering a reinforced concrete material with density ρ equal to 25 kN/m^3.

It is worth to underline that the FE software has been employed to perform a linear elastic analysis and compute the internal forces of the form-found shell under the acting loading. The calculation of the values of N and M is preparatory to the application of the RF-ellipse method. The evaluation of the R-funicularity is related to the geometry of the shell surface. The proposed method considers the shape of the shell regardless of the strength of the material chosen. Therefore it is supposed to be preliminary to any additional analyses, such as a buckling analysis, necessary to check the structural feasibility of the shell structure and that may be chosen according to the construction material employed.

5.4   Case studies

5.4.1   Case study 1 - Shell with Gaussian curvature equal to zero

The first structural shape analyzed is the vault with Gaussian curvature equal to zero shown in Figure 5.9. The shell geometry has been obtained starting from a flat rectangular shell 10×20 m, pin-supported at the longer edges. Kangaroo Physics allows the funicular shape to be found under self-weight with an assigned spring stiffness equal to 10 N/m.

This surface can be described as an extruded catenary curve, i.e. a curve formed by a chain hanging freely from two points that are not in the same vertical line.

Neglecting the effects of the boundary conditions, thin vaults obtained from catenary generatrices behave as a series of independent arches and have a bending-free behavior under self-weight, hence when the applied load corresponds to the one applied to obtain the original catenary curve but opposite in sign [6].

The vault is 20 cm thick and the longitudinal edges are pinned. The only load applied is the self-weight.

(a) *Form-found surface*
(b) *Joint position*
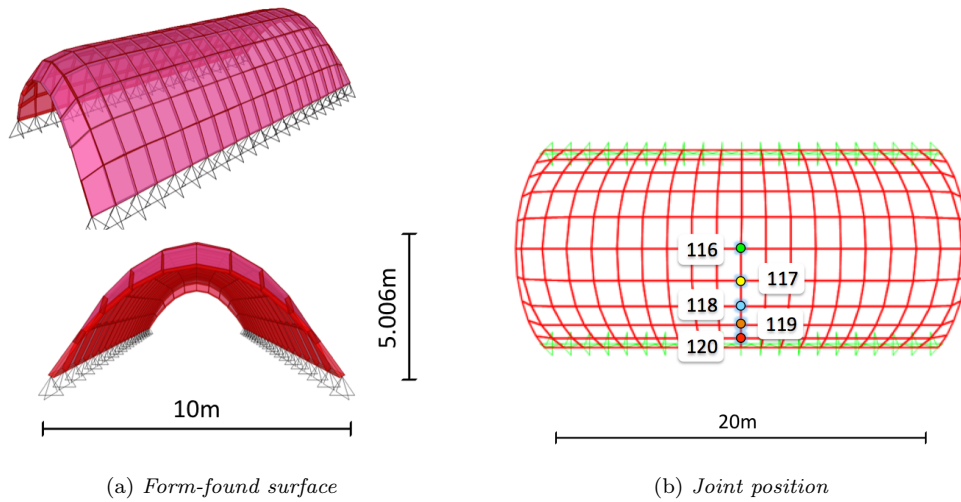
Figure 5.9: Shell with Gaussian curvature equal to zero

The RF-ellipse method has been applied to the surface. Results are presented focusing on the shell behavior in the areas indicated by the nodes shown in Figure 5.9b.

As shown in Figure 5.10, all ellipses degenerate in to line segments flattened on the N axis confirming that the shell has a bending-free behavior and is R-Funicular.
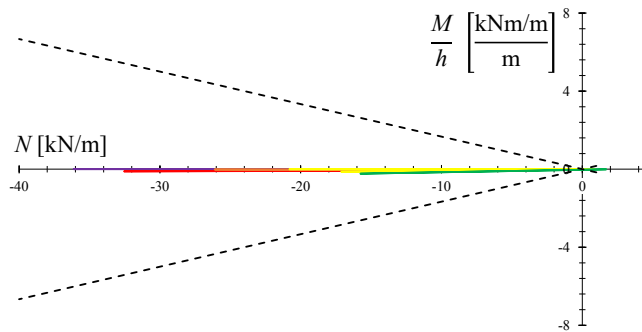
Figure 5.10: RF-ellipse method applied to the shell with Gaussian curvature equal to zero [The color of the ellipses matches with the color of the joints in Fig. 5.9b]

5.4.2 Case study 2 - Shell with positive Gaussian curvature

The second structural shape analyzed is the shell with positive Gaussian curvature shown in Figure 5.11. The surface geometry has been obtained starting from a flat square shell 20×20 m, pin-supported at the four corners. Three nodes have been pinned at every corner in order to model a more realistic constraint. Kangaroo Physics allows the funicular shape to be found under self-weight with an assigned spring stiffness equal to 500 N/m.

This shape structure has been analyzed under three different boundary conditions as indicated in Figure 5.12. Static loads have then been applied to the surface: a first analysis has been performed under the action of self-weight only, while at a second stage a horizontal load equivalent to 30% of the self-weight has been added (Fig. 5.13). The same procedure has been implemented for different shell thicknesses: 6 cm, 12 cm, 20 cm, 35 cm and 50 cm.

(a) *Form-found surface*

(b) *Joint position*
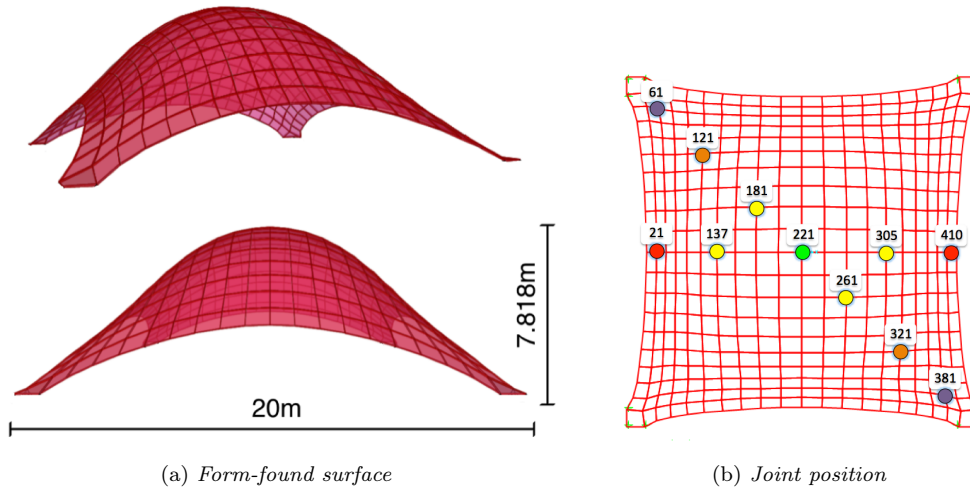
Figure 5.11: Shell with positive Gaussian curvature

(a) *Clamped boundaries*

(b) *Pinned boundaries*
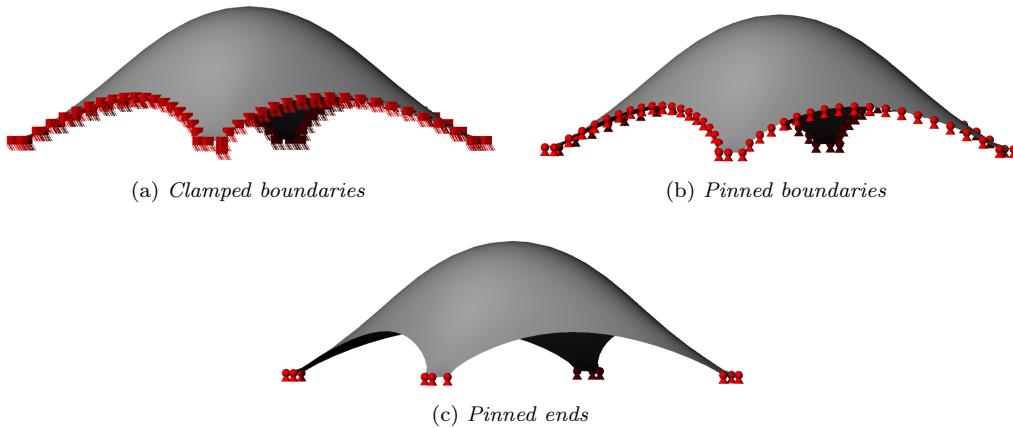
(c) *Pinned ends*

Figure 5.12: Shell with positive Gaussian curvature - Boundary conditions applied

The results obtained by applying the RF-ellipse method are summarized as follows. The case under self-weight and pinned end boundary conditions is the one used in the form finding procedure implemented in Kangaroo Physics, the corresponding RF-ellipses shown in Figure 5.14 are flattened on the N axis.

The structural behavior improves decreasing the thickness: under self-weight the 6 cm surface is more R-Funicular than the 50 cm surface. Concerning the 50 cm surface, the ellipses related to joints 121 and 321 exceed the domain (Fig. 5.11), hence the orange straight line of Figure 5.14b crosses the minimum eccentricity represented by the dotted black line. Modifying the thickness of the shell leads to the following changes:

- the self-weight changes in terms of absolute value but not in terms of distribution of the load, hence the funicularity of the shell is not affected;

- the ratio between membrane stiffness and flexural stiffness changes, hence the funicularity of the shell is affected.

(a) *Self-weight* (b) *Self-weight + horizontal load*
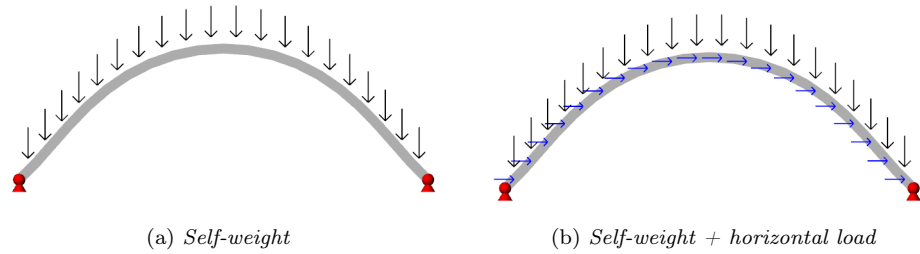
Figure 5.13: Shell with positive Gaussian curvature - Loads applied

(a) *pinned ends, h=6cm, self-weight* (b) *pinned ends, h=50cm, self-weight*

Figure 5.14: RF-ellipse method applied to shell with positive Gaussian curvature - Thickness effect on self-weight [The color of the ellipses matches with the color of the joints in Fig. 5.11b]

Effect of horizontal load

With the addition of the horizontal load, equal to 30% of the self-weight, the bending moments raises, as one can observe comparing Figure 5.14a and Figure 5.15a. In this latter figure, the opposite effect of the thickness on the analyzed form-found shape can be observed: the structural behavior improves increasing the thickness; in fact the 50 *cm* surface is more R-Funicular than the 6 *cm* one.

In Figure 5.16, one can observe how different boundary conditions affect the behavior of the shell. The bending moment increases changing from pinned ends, used in the form finding procedure, to pinned borders or clamped borders. In Figure 5.16c, only the joints located inside the green area can still be considered R-funicular.

In Figure 5.17, one can observe that also with different boundary conditions a thicker shell behaves better than a thinner shell under self-weight and horizontal load. The R-Funicularity area increased as indicated in Figure 5.17c, maintaining a relevant bending effect only at the corners.

For a thicker shell ($h = 50$ *cm*), it is interesting to see how, restoring the boundary conditions used in the form finding procedure, the structural shape almost recovers the R-Funicularity in every considered joint. In the clamped borders case (Fig. 5.18a) joints 61 and 381 exceed the limit values, this is due to the proximity to the corners and the influence of the boundary conditions.

In the pinned ends case (Fig. 5.18b) the only joint exceeding the limits is the number 121, far from the applied boundary conditions. When pinned ends (used in the form finding process) are applied, the influencing parameter is the curvature more than the boundary conditions. In fact the curvature of the surface becomes flatter where the joint 121 is located (Fig. 5.18d).

(a) *pinned ends, h=6cm,*
self-weight + horizontal load

(b) *pinned ends, h=50cm,*
self-weight + horizontal load
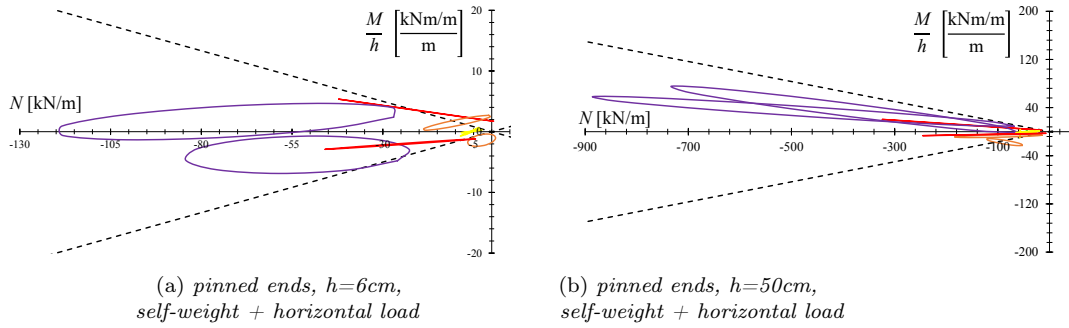
Figure 5.15: RF-ellipse method applied to shell with positive Gaussian curvature - Thickness effect on self-weight plus horizontal load [The color of the ellipses matches with the color of the joints in Fig. 5.11]

(a) *pinned borders, h=6cm,*
self-weight

(b) *clamped borders, h=6cm,*
self-weight

(c) *R-Funicularity area*

Figure 5.16: RF-ellipse method applied to shell with positive Gaussian curvature - Boundary condition effect on thin shells under self-weight [The color of the ellipses matches with the color of the joints]

(a) *clamped borders, h=6cm, self-weight+horizontal*

(b) *clamped borders, h=50cm, self-weight+horizontal load*

(c) *R-Funicularity areas*

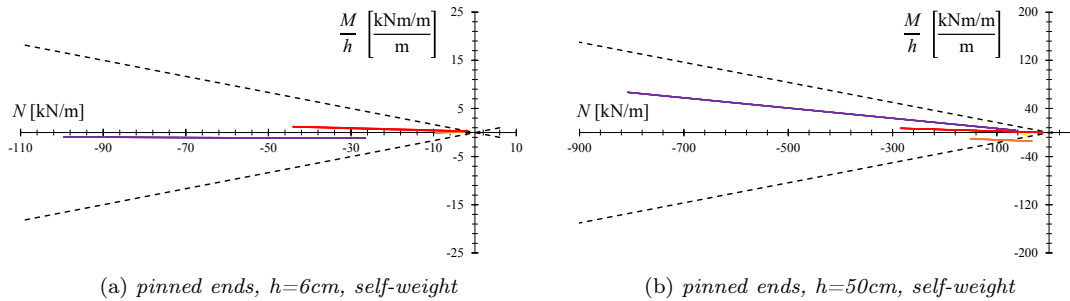Figure 5.17: RF-ellipse method applied to shell with positive Gaussian curvature - Thickness effect under self-weight plus horizontal load with clamped borders [The color of the ellipses matches with the color of the joints]
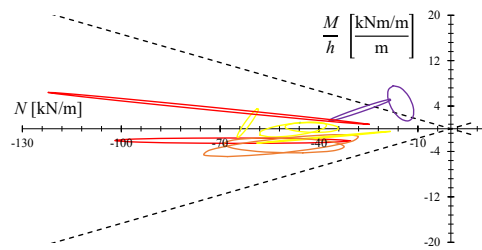
(a) *clamped borders, h=50cm,*
self-weight+horizontal load
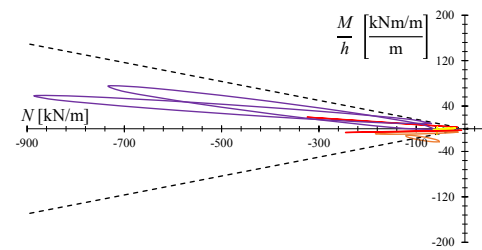
(b) *pinned ends, h=50cm,*
self-weight+horizontal load

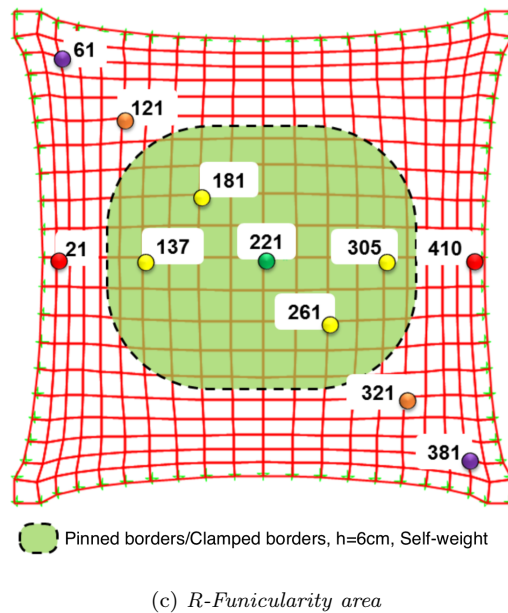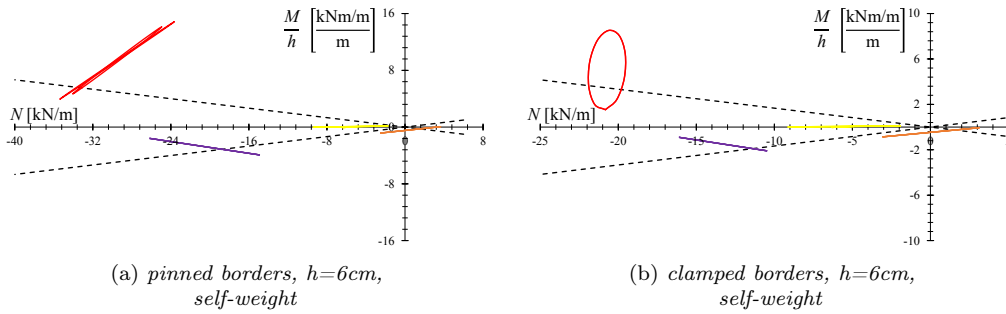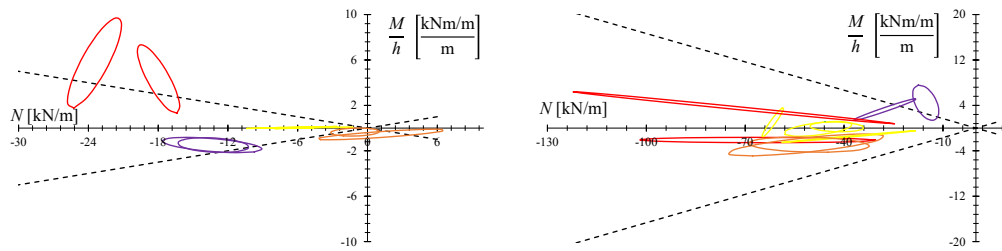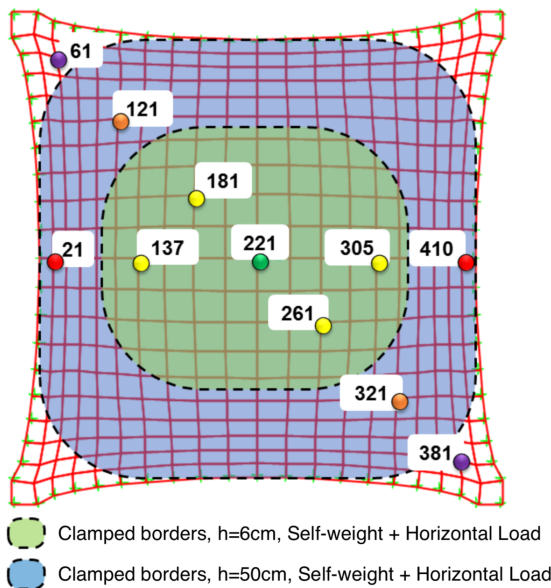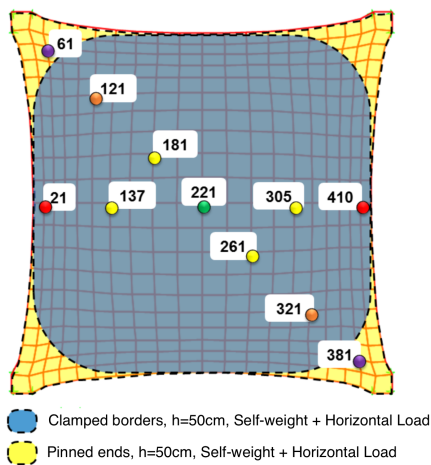(c) *R-Funicularity area*
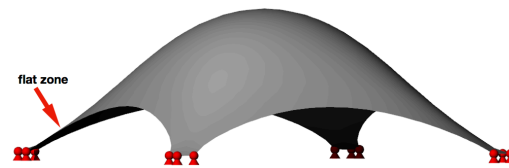
(d) *Location of joint 121*

Figure 5.18: RF-ellipse method applied to shell with positive Gaussian curvature - Boundary condition effect on thick shells under self-weight plus horizontal load [The color of the ellipses matches with the color of the joints]

Chapter 6

Dynamic behavior of form-found shells

Civil shell structures are generally designed with the objective to achieve an ideal membrane behavior and pursuing criteria of structural efficiency and minimization of the material used. During the shell form finding process, gravity loads are generally considered, while the role of horizontal loading is ignored. Today shells with complex geometries are being designed and built, and are used to shelter people during extreme events such as earthquakes, but the dynamic behavior of thin shells has always been subjected to limited research. A two-phased methodology to investigate the effects of dynamic loading on the behavior of civil thin shells form-found under gravity loads is proposed. Following an initial literature overview on the dynamic behavior of shell structures presented in Section 6.1, the rationale of the methodology proposed is presented in Section 6.2. In Section 6.3 the form-found and numerical models used are detailed. Section 6.4 is dedicated to the presentation of the results obtained applying the methodology to two different form-found shell structures: one with positive and one with negative Gaussian curvature. Moreover the shell with positive Gaussian curvature is analyzed under the action of a real seismic event.

6.1   Dynamic behavior of shells

In order to design an efficient structural system, all factors influencing the behavior of the structure must be characterized and understood. The effect of loading on the shell structural response is of crucial importance when selecting the best shape. If shells resist external loads mainly through membrane stresses, they are characterized by an effective response in term of strength-to-weight ratio resulting in reduced thickness and efficient use of material.

As seen in Chapter 3, given a specific loading and boundary conditions, different form finding techniques have been proposed to find the shape for the shell that allows an ideal membrane behavior. When applying a form finding method to design a civil shell structure, the load considered is most commonly taken to be a static gravity load. As a result the shape experiences a state of membrane stresses when only the self-weight, the only permanent load, acts upon it. In general horizontal loads due to wind or earthquakes, are not taken into consideration in the conceptual design stage but their effect on the shell behavior is only verified once the form is already generated. Even in seismic areas, where horizontal forces can become the dominant loading under extreme events, seismic loadings are usually neglected in the conceptual phases of the design process [1].

The omission to consider seismic loads in the form generation process can be justified by the fact that shells have shown an apparent good seismic resistance [84, 71]. Because of

their relative lightweight nature, the seismic forces induced are relatively low. However the interaction between shape and dynamic loading for shell roofs has been subject to limited research. As shells with more complex forms are being designed and built today, a deeper understanding of their behavior is the key. Moreover shells are used to build structures, which function is crucial even in case of catastrophic events: shell roofs are often use to shelter people during disasters (e.g. earthquake, tornado, hurricanes) [97]. These considerations emphasize the importance of gaining a better insight into the dynamic behavior of shells.

Bearing in mind that achieving a state of membrane stress should always be the design objective, the research goal of this study is to present an analysis methodology that allows for the evaluation of the effects of dynamic loading (e.g. earthquakes) on the membrane behavior of shells form-found for gravity loading.

6.1.1 About free vibrations of shells

Different studies have been carried out to understand free vibrations of shell structures. Geometry, thickness, material, curvature and initial imperfections are all parameters that can affect the performance of a shell and its fundamental modes [84].

In 1970 Leissa investigated the influence of curvature on shallow shell vibrations [59]. A shell is considered shallow when the rise of the shell is less than 1/5 of the smallest planform dimension. By solving the linear eigenvalue problem, Leissa demonstrated how the curvature ratio affects the frequencies. He showed that the minimum fundamental frequency always occurs for negative Gaussian curvature. He also demonstrated that the hyperbolic paraboloid, for certain boundary aspect ratios, behaves like a simply supported square plate with no stiffness being added by the curvature of the shell. Moreover Leissa extended these analyses into the non-linear field and focused on different methods for obtaining the equations of motions and finding the natural frequencies of cylindrical, conical, spherical shapes and other shells of revolution. The equations of motion describe the behaviour of a physical system as a set of mathematical functions in terms of dynamic variables. The differential equations are the most common approach for finding equations of motion used by researchers [84]. In order to derive the natural frequencies of different shell geometries, Leissa summarized previous studies on the derivation of differential sets of equations according to different shell theories [58]. Among others recalled by Leissa, Arnold and Warburton derived their widely used equations of motion valid for thin cylindrical shells by using Lagrange equations [5]. Later, the equations of motion for free vibrations of orthotropically stiffened spherical shells have been derived in [98] using a Finite Difference approach.

More recently an extensive review of papers published from 1989 to 2000 related to the subject of free vibrations and dynamic behavior of shells was published [88, 89]. In this review extensive studies on vibrations of singly-curved shallow shells and doubly-curved shallow shells, mainly spherical, are presented. For example, the effect of different boundary conditions on shells with positive and negative Gaussian curvature is reported in [62].

In 2011 Qatu published the first comprehensive study of shallow shell vibrations subjected to different boundary conditions presenting natural frequencies for various shell curvatures for a series of spherical, cylindrical and hyperbolic paraboloidal geometries [90].

Some years later, a study on a family of axisymmetric shells of revolution with equal material, mass and thickness, but variable curvature was published in [41]. In this study, the authors performed modal analyses and observed that the natural frequency of the shell increases with the curvature and frequency values can be approximated by a linear function of the characteristic ratio c/R where c is the height of the shell pole and R the radius of its circular plane projection.

6.1.2 Behavior of shell structures during seismic events

The literature review just presented shows the studies available on the topic of free vibrations, however there is a real gap of knowledge in the domain of forced vibrations and seismic response of shells.

Some initials studies have used the Fourier series to obtain a closed-form solution for the non-linear dynamic response of shallow shells under earthquake loading [50]. Following the 1995 Hyogoken-Nanbu earthquake in Japan, few reviews of the performance of shell structures subjected to this catastrophic event were published. The accelerations and stresses of spherical domes and cylindrical roof shells located in the city of Kobe were investigated using mathematically analytic solutions [54]. A more general survey of damages to spatial structures caused by the Japanese seismic event can be found in [95]. Also in [51], the author investigates the performance of shell structures specifying that, during the emergency, many large roof spaces were converted as temporary refuge spaces. Moreover, he reports that light weight large roof structures could mostly survive, while a few large span roof structures were heavily damaged.

As seen, most of the research reviewed by Qatu in [88, 89] discusses the problem of free vibrations, however few studies considered also the response of shells under dynamic loadings. As example, [72] examines parametric vibrations of cylindrical shell under combined static and periodic axial loading.

The results of seismic analyses of double-layer barrel vaults with different configurations and support conditions are presented in [73]. In this study, the author states that in space structures of non-plane geometry (like domes and barrel vaults) higher modes and vertical modes give an effective contribution to the dynamic response.

More recently, for cylindrical and doubly-curved surfaces, Ostovari-Dailamani [84] gave a fundamental contribution studying the behaviour of cylindrical and doubly-curved shells under earthquake loading. Her study showed how the membrane stiffness and the bending stiffness control the natural shell modes and that the doubly-curved shell shapes have natural modes with higher frequencies compared with singly-curved cylindrical geometries. Moreover the response of cylindrical shells under the action of earthquake loading was studied, using both an analytical and a numerical approach. Comparing the results and checking the convergence of the values, the number of modes required to accurately predict displacement, acceleration and stress for a specific shell geometry was established.

Concerning form-found shells, to the best of the author's knowledge, few studies on their dynamic behavior are available. A study of form-found arches and shell structures subjected to seismic loading can be found in [69, 70], where a form finding algorithm to generate geometries under combined gravity and horizontal loading is presented. Recently, a study that reformulates the form finding technique known as Thrust Network Analysis (TNA) was published and can be found in [66], where the authors extend the TNA methodology to include the effect of horizontal forces.

6.2 Two-phased methodology

The concise review in Section 6.1 showed that there is a little research literature available on the dynamic behavior of mathematical shell structures (e.g. directly described by analytical functions), while the dynamic behavior of form-found shells has not been largely investigated. Due to this lack of knowledge and the increasing interest in form-found shell shapes [1], the objective of this study is to characterize the dynamic behavior of form-found thin shell geometries. In order to study the effect of the shape on the dynamic behavior of form-found shells, a two-phased methodology is presented. In the first phase, a modal analysis is carried out, while in the second phase a forced dynamic analysis (i.e. a time-history analysis) is

performed. In both phases the R-Funicularity Ellipse Method discussed in Chapter 5 is applied, setting the admissibility coefficient equal to $\lambda = 1/6$. This methodology is summarized in the flowchart in Figure 6.1. A general description is given next and every step is explained in detail in Section 6.4, where the application of the method to different form-found shells is shown.
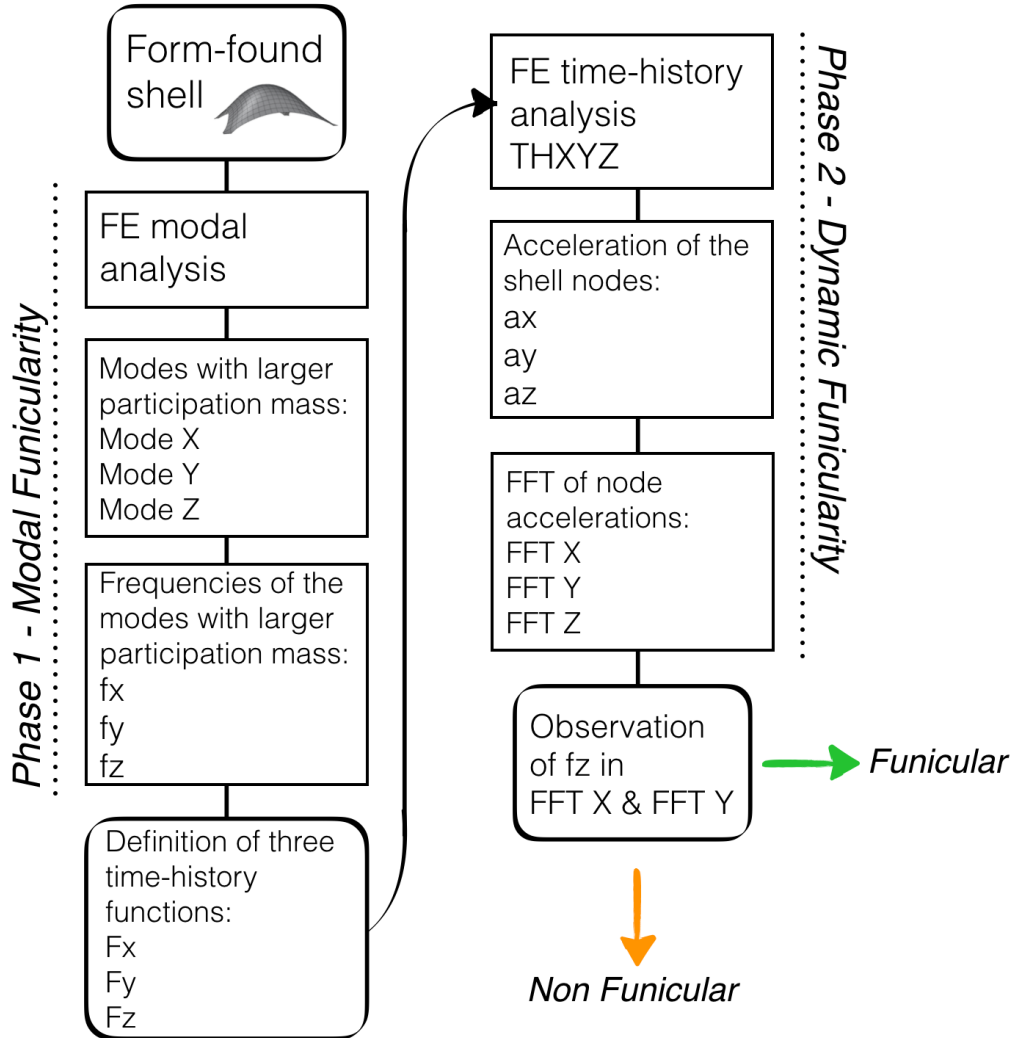
Figure 6.1: Two-phased methodology to study the effect of the shape on the dynamic behavior of form-found shells

6.2.1   Phase 1 - Modal Funicularity

When performing a modal analysis on a shell, the structure can be thought of as a system of an infinite number of mass particles. As a consequence, when excited, the system possesses an infinite number of degrees of freedom. Hence the response of a shell may be decomposed into an infinite number of periodic motions. These motions are the normal modes of free vibration, each of them with an associated natural frequency of free vibration [53]. Each couple of

eigenmode and eigenfrequency is an intrinsic property of the shell and their evaluation is the first step of the first phase of the methodology proposed.

Since all modes are characterized by a shape, related stresses can be computed for every mode obtained. However, the magnitude of the modal shape is arbitrary and does not correspond to a real displacement, hence the modal stresses are useful in term of distribution, regardless of their values. In other words, the absolute values of stress results have not meaning, but the relative values between two or more points in the shell surface can provide insights into the shell behavior.

Using the stress distribution obtained for each mode of the shell analyzed and the R-Funicularity Ellipse Method the concept of *Modal Funicularity* is introduced. Evaluating the Modal Funicularity of a shell refers to the assessment of the R-Funicularity, where the values of normal force $N(\theta)$ and bending moment $M(\theta)$ are the ones related to a specific modal shape. A comparison of Modal Funicularities for different modes allows one to evaluate which modal shape is more or less funicular. For each direction of coordinates X, Y and Z, the modes exciting largest participating mass and the related eigenfrequency are identified. Between these three modes, the one more funicular is shown.

6.2.2 Phase 2 - Dynamic Funicularity

In the second phase, linear time-history analyses are performed to observe the evolution of the dynamic response of the shell over time. Three time-history functions are defined based on the frequencies of the modes with largest participating mass identified in phase 1, one function for each direction X, Y and Z. A forced dynamic analysis combining all three functions is performed. At this point, the R-Funicularity Ellipse Method can be applied to the results obtained for every time step of the analysis in order to observe the evolution of the *Dynamic Funicularity* over time.

Moreover, the influence of each of the three time-history functions on the shell response is evaluated. In order to analyze the response of linear systems to excitations varying with time two different approaches may be adopted: a time-domain method symbolized by Duhamel's integral or a frequency-domain method [20, 21]. Adopting the latter approach, when the excitation is not periodic, it may be represented using the Fourier integral that involves the use of the Fourier Transform (FT). The FT decomposes a signal, function of time, into the frequencies that constitute it. Analytical evaluation of the FT is feasible only for excitations described by simple functions applied to simple structural systems. When the problem is more complicated, these integrals must be evaluated numerically. The discrete version of the FT is represented by the Discrete Fourier Transform (DFT) that can be computed with the application of the Fast Fourier Transform (FFT). The FFT is a highly efficient algorithm that drastically reduces the computational effort [83].

Starting from the accelerations of a node of the shell in the three directions X, Y and Z, the FFT converts the results from the time-domain to the frequency-domain. The observation of the FFT results, hence of the frequency content for a specific node, can finally give insight on the funicularity of the shell in that node.

6.3 Form-found and numerical shell models

Analogously to the case studies presented in Chapter 5, all shell shapes have been generated using a particle spring approach applied to an inverted hanging chain model, implemented in the plug-in Kangaroo Physics of the 3D modeling software Rhinoceros.

Two typologies of axisymmetric surfaces have been analyzed: shells with positive and negative Gaussian curvature (i.e. synclastic and anticlastic surfaces, respectively).

Starting with a numerical model of the form-found shell, all structural analyses are carried out in the FE software SAP2000 using a thin shell element formulation [22]. The mesh of the numerical model, consistently with the form-found surface and according to the sensitivity analysis performed, is equal to 1×1 m. The shells are analyzed considering a reinforced concrete material with density ρ equal to 25 kN/m^3. For further details concerning the form-found and the numerical shell models refer to Section 5.3.

In the modal analyses, possible multiple values due to the axial symmetry of the shapes are avoided by moving one node of the surface a thousandth of a meter: this measure discards the coupling effect, without affecting the analysis results.

6.3.1   Sensitivity analysis of the mesh

When performing FE analyses, the mesh density of the numerical model is a critical issue as it affects the accuracy of the results obtained. The choice of the discretization of the mesh needs to balance the reliability of the outputs, in term of stresses, displacements, modal shapes and frequencies, with the computational effort. A sensitivity analysis has been carried out to choose a mesh size that yields accurate results in the modal analysis which is the starting point (phase 1) of the two-phase methodology presented in Section 6.2.

As a benchmark study, the shallow shell studied by Leissa [59] is chosen. The numerical FE analysis has been performed for different mesh size in order to find a discretization able to give results, in terms of frequencies and modal shapes, consistent with the analytical ones obtained by Leissa, without being too computationally onerous. Following this procedure, a mesh size of 1×1 m has been chosen and adopted also for the models of the form-found shapes in this study.

The shell is characterized by a square boundary ($a/b = 1$) and has a mid-surface given by the following equation:

$$z = -\frac{1}{2}(\frac{x^2}{R_x} + \frac{y^2}{R_y}), \tag{6.1}$$

where R_x and R_y are constants identifying the radii of curvature in the X and Y directions, respectively. The conditions on shallowness and thickness h are $a/R_x = 0.4$ and $h/R_x = 0.001$.

The results are recorded for a curvature ratio interval equal to $R_x/R_y \in [-1.5, 1.5]$. The shell is assumed to be supported on all boundaries by shear diaphragms that allow displacements only in the direction perpendicular to the edge considered and with negligible bending resistance. For further details of the shell analyzed and the analytical calculations adopted by Leissa, the reader is referred to [59] and [60]. Results are given by Leissa in terms of non-dimensional frequency parameters:

$$\omega_{ad}^2 = \rho\omega^2(1 - \nu^2)R_x^2/E, \tag{6.2}$$

where ν is the Poisson's coefficient equal to 0.3, E is the Young's modulus and ω is the angular frequency. The numerical analyses are performed neglecting the tangential inertia and setting the following values: $a = b = 40$ m, $\rho = 25$ kN/m^3 and $E = 30600000$ kN/m^2. In Table 6.1 the frequency $f = \omega/2\pi$ obtained in the numerical FE analysis is compared with the value obtained analytically by Leissa for a curvature ratio $R_x/R_y = 1$ and different mesh sizes.

The result obtained for the 0.5×0.5 m mesh is only 0.03% more accurate than the 1×1 m mesh, on the other hand the duration of the analysis is five times longer.

In Table 6.2, for a mesh equal to 1×1 m and different curvature ratios, the values of the numerical and analytical frequencies are shown. The accuracy is acceptable for shells with positive and negative Gaussian curvature, such as the ones analyzed in Section 6.4. Hence a mesh size equal to 1×1 m has been adopted throughout this study.

Mesh size	4x4m	2x2m	1x1m	0.5x0.5m
$f_{numerical}[FE]$	5.2077	5.4557	5.4671	5.4686
$f_{analytical}[Leissa]$	5.5720	5.5720	5.5720	5.5720
Difference %	6.99	2.13	1.92	1.89

Table 6.1: $R_x/R_y = 1$ - Comparison between numerical and analytical frequency values

Rx/Ry	-1.5	-1	-0.5	0	0.5	1	1.5
$f_{numerical}[FE]$	1.3811	0.2011	1.3967	2.7735	4.1424	5.4671	6.8642
$f_{analytical}[Leissa]$	1.4075	0.2079	1.4075	2.7918	4.1813	5.5720	6.9633
Difference %	1.91	3.38	0.77	0.66	0.94	1.92	1.44

Table 6.2: Mesh $1 \times 1\ m$ and $R_x/R_y \in [-1.5, 1.5]$ - Comparison between numerical and analytical frequency values

6.4 Case studies

6.4.1 Case study 1 - Shell with positive Gaussian curvature

Phase 1 - Modal Funicularity

The first shell analyzed is the form-found vault with positive Gaussian curvature introduced in Subsection 5.4.2 and obtained from a flat square mesh $20 \times 20\ m$ supported at its four corners, under the action of the self-weight only (Fig. 6.2). Three nodes have been pinned at every corner in order to model a more realistic constraint. The same procedure has been implemented for different shell thicknesses: 6 cm and 50 cm, in order to observe the difference in dynamic behavior between a thin and a thick surface.

(a) *Form-found surface*   (b) *Joint position*

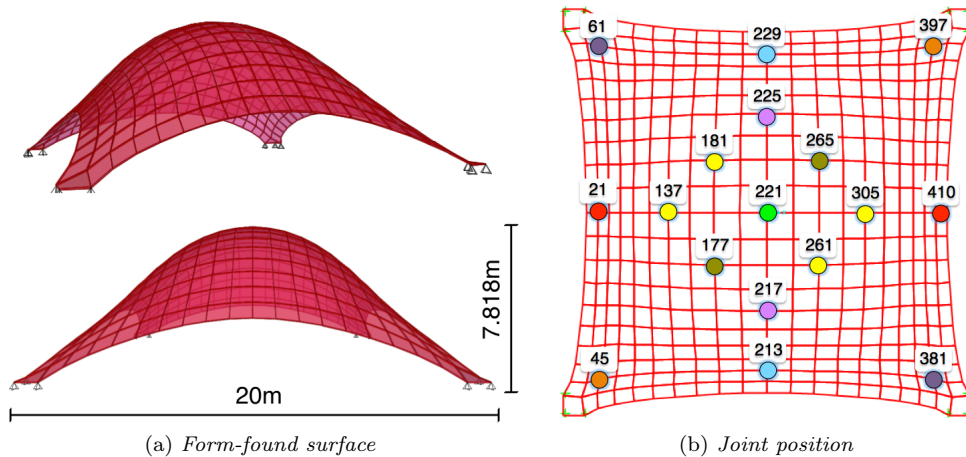Figure 6.2: Shell with positive Gaussian curvature

The first modal analysis has been performed on the 6 cm thick shell. The number of modes to be selected in order to have a participating mass bigger than 90% in all three directions (X, Y and Z) is 56 modes, but a larger number equal to 300 modes has been adopted to ensure convergence of the results in the forced analyses performed in phase 2 [84].

Table 6.3 shows the eigenmodes with the more significant participating mass in the X, Y and Z directions.

Shell with Positive Gaussian Curvature

Step	Frequency [Hz]	Modal Participating Mass Ratios					
		UX	UY	UZ	SumUX	SumUy	SumUZ
Mode 14	10.583	**0.183**	0.020	0	0.206	0.043	0
Mode 15	10.585	0.020	**0.183**	0	0.226	0.226	0
Mode 22	15.207	0	0	**0.822**	0.232	0.233	0.822
Mode 42	22.628	0	0	0.064	0.258	0.258	0.944
Mode 55	26.194	0.367	0.014	0	0.937	0.584	0.977
Mode 56	26.197	0.014	0.367	0	0.951	0.951	0.977

Table 6.3: Results of modal analysis performed on the shell shown in Fig. 6.2 (6 *cm* thick)

Subsequently the R-Funicularity Ellipse Method can be applied to the stress distribution related to the eigenmodes. Hence the eccentricity is computed in every node of the shell using Equation (5.8), and the inclusion in the admissibility interval is checked to verify the condition of R-Funicularity of the eigenmode, or the so-called Modal Funicularity.

The results obtained for the modes with larger participating mass in X, Y and Z directions (i.e. Mode 14, 15 and 22 with participating mass in bold in Table 6.3) are indicated in Figure 6.3. Among them, the one with a larger participating mass in Z direction (i.e. Mode 22) is the more funicular one. Observing the deformed geometry of the Mode 22, it is interesting to highlight a strong similarity with the shape obtained in the form finding process of the shell. In fact the modal shape 22 is the one that diverges less from the form-found shape, the one that guarantees a funicular behavior under load and supports applied.

■ R-Funicularity condition verified
■ R-Funicularity condition NOT verified

(a) *Mode 14 - X direction*   (b) *Mode 15 - Y direction*   (c) *Mode 22 - Z direction*
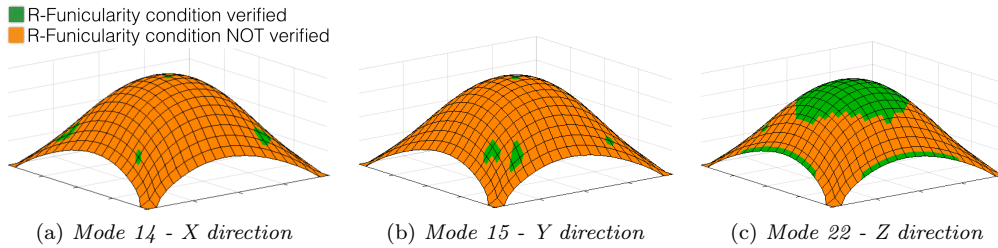
Figure 6.3: Modal Funicularity of the 6 *cm* thick shell shown in Fig. 6.2

A second modal analysis has been performed applying to the form-found geometry a thickness equal to 50 *cm*. The eigenmodes of the thick shell have been compared to the one of the thin shell in order to find similarities and compare the related Modal Funicularity. The correlation between modal vectors can be estimated using the modal assurance criterion (MAC) [3]. This parameter quantifies the similarity between modal vectors originating from different sources and is defined as follows:

$$MAC(\Phi_i, \Phi_j) = \frac{(\Phi_i^T \Phi_j)^2}{(\Phi_i^T \Phi_i)(\Phi_j^T \Phi_j)} \tag{6.3}$$

where Φ_i is the modal vector of the 6 *cm* thick shell and Φ_j is the modal vector of the 50 *cm* thick shell with $i, j = 1, 2, ..., n$ where n is equal to the degree of freedom of the

system. The modal assurance criterion takes on values from zero, representing no consistent correspondence, to one, representing a consistent correspondence.

The first 25 modal vectors are compared and the comparable modes are reported in Table 6.4. In the first two rows, the more relevant modes in term of participating mass in horizontal directions are shown. These modes are mode 14 and 15 for the 6 *cm* thick shell and mode 11 and 10 for the 50 *cm* thick one. The MAC values show a very low correspondence between them. Mode 22 for the 6 *cm* thick shell and mode 7 for the 50 *cm* thick shell are the ones more relevant in term of participating mass in vertical direction (82.2% and 92.9% respectively) and the MAC value show a high correspondence between them. In the remaining rows, couple of values with a MAC close to one are shown demonstrating a consistent correspondence between them.

Shell with Positive Gaussian Curvature						
Thickness	**Mode**	**Frequency [Hz]**	**Modal Participating Mass**			**MAC**
			UX	**UY**	**UZ**	
6 cm	14	10.6	18.3%	2.0%	<<1.0%	**0.002**
50 cm	11	27.1	46.5%	17.8%	<<1.0%	
6 cm	15	10.6	2.0%	18.3%	<<1.0%	**0.002**
50 cm	10	27.1	17.8%	46.5%	<<1.0%	
6 cm	4	3.9	<<1.0%	<<1.0%	<<1.0%	**0.994**
50 cm	8	21.0	<<1.0%	<<1.0%	<<1.0%	
6 cm	3	3.2	<<1.0%	<<1.0%	<<1.0%	**0.942**
50 cm	9	22.5	<<1.0%	<<1.0%	4.2%	
6 cm	22	15.2	<<1.0%	<<1.0%	82.2%	**0.785**
50 cm	7	18.0	<<1.0%	<<1.0%	92.9%	
6 cm	5	4.4	<<1.0%	<<1.0%	<<1.0%	**0.916**
50 cm	2	11.8	<<1.0%	<<1.0%	<<1.0%	

Table 6.4: Significant modes for 6 *cm* and 50 *cm* thick shells shown in Fig. 6.2

Applying the R-Funicularity Ellipse Method, the ellipses of eccentricity of the nodes indicated in Figure 6.2b can be drawn. In Figure 6.4a, ellipses related to the Mode 4 of the 6 *cm* thick shell are compared to the ones related to the Mode 8 of the 50 *cm* thick shell. Even if the MAC indicates a high correspondence between the two, the ellipses are not similar. However it is interesting to note that all of them are represented as a line crossing the origin. This graphical representation means that the eccentricity in every point is independent from the direction, as seen in Section 5.2.

The 6 *cm* thick shell seems to behave better than the 50 *cm* thick shell, hence it seems to be more R-Funicular. This observation has been confirmed checking the results of all modes of Table 6.4.

In Figure 6.4b the RF-ellipses are drawn for the vertical modes (i.e. Mode 22 for the 6 *cm* thick shell and mode 7 for the 50 *cm* thick shell). Since all ellipses respect the limiting values represented by the dotted lines, the R-Funicularity is confirmed and the contribution of the bending moments is much smaller compared to the one of the membrane forces.

Phase 2 - Dynamic Funicularity

In the time-history analysis, a modal solution method has been selected [22]. The analysis is performed applying a thickness equal to 6 *cm* only.
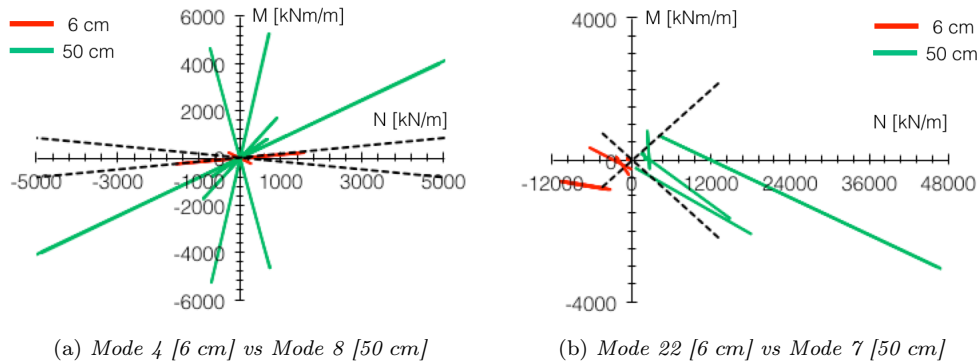
(a) *Mode 4 [6 cm] vs Mode 8 [50 cm]*   (b) *Mode 22 [6 cm] vs Mode 7 [50 cm]*

Figure 6.4: Modal Funicularity of the nodes shown in Fig. 6.2 - 6 *cm* thick shell vs 50 *cm* thick shell with positive Gaussian curvature

In the first instance, starting from the assumption that the modal internal forces distribution is equal to the forced internal forces distribution when the correspondent mode is excited, three periodic functions have been defined according to the first three modes that have a significant participating mass. As indicated in Table 6.3, these modes are mode 14 and 15 for the X and Y direction respectively and mode 22 for the Z direction.

Under a single frequency spectrum that excites the vertical mode (mode 22), the forced internal forces distribution is equal to the modal one. Hence the eccentricities obtained from the time-history analysis are equal to the modal analysis eccentricities and the area of the shell where the dynamic R-Funicularity is verified coincides with the area where the modal R-Funicularity is also verified (Fig. 6.3c).

In order to further investigate these results, a time-history analysis with multiple frequencies spectrum has been performed. Horizontal modes 14 and 15 have been excited in addition to the vertical one and a 5% damping has been taken into account, as usually assumed for concrete structures [84]. To evaluate the shell response to each component of the applied dynamic load and to convert the results from time-domain to frequency-domain functions, the Fast Fourier Transform (FFT) [83] is applied to the accelerations in X, Y and Z direction of the nodes of the shell.

Results are presented focusing on the shell behavior in the areas indicated by the nodes shown in Figure 6.5, as these nodes are characteristic of the different behaviors across the shell surface. For the shell geometry under study, the nodes are defined R-Funicular if located in the area of the shell where the R-Funicularity condition is verified.

In Figure 6.6, examples of the results in terms of frequency content are shown for node 61 (not R-Funicular) and node 181 (R-Funicular). For both nodes, the FFT of the X acceleration coincides with the one of the Y acceleration. Figures 6.14f and 6.14c show peaks at 10 Hz and 15 Hz, the frequency of the horizontal and vertical modes respectively and the FFT of the X and Y accelerations shows an amplitude smaller than the one of the Z acceleration (Fig. 6.14b - 6.14d).

The behavior of the R-Funicular nodes obtained exciting the vertical mode and circumscribed by the green circle as shown in Figure 6.5 can be explained as follows. Independently from the FFT of the Z acceleration, the R-Funicular nodes have a FFT of the horizontal acceleration without peak at 15 Hz (see Fig. 6.14c: node 181 is indicated as example). Otherwise, the non R-Funicular nodes always show a peak at 15 Hz in the FFT of their X or Y accelerations (see Fig. 6.14f: node 61 is indicated as example). In other words, for the case analyzed, the node is R-Funicular if, at a frequency value equal to 15 Hz, only a vertical acceleration can be observed and not a horizontal one.
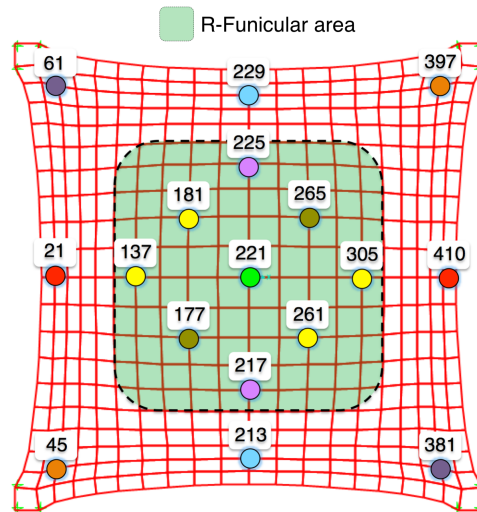
Figure 6.5: Joint position and R-Funicular area of the shell with positive Gaussian curvature
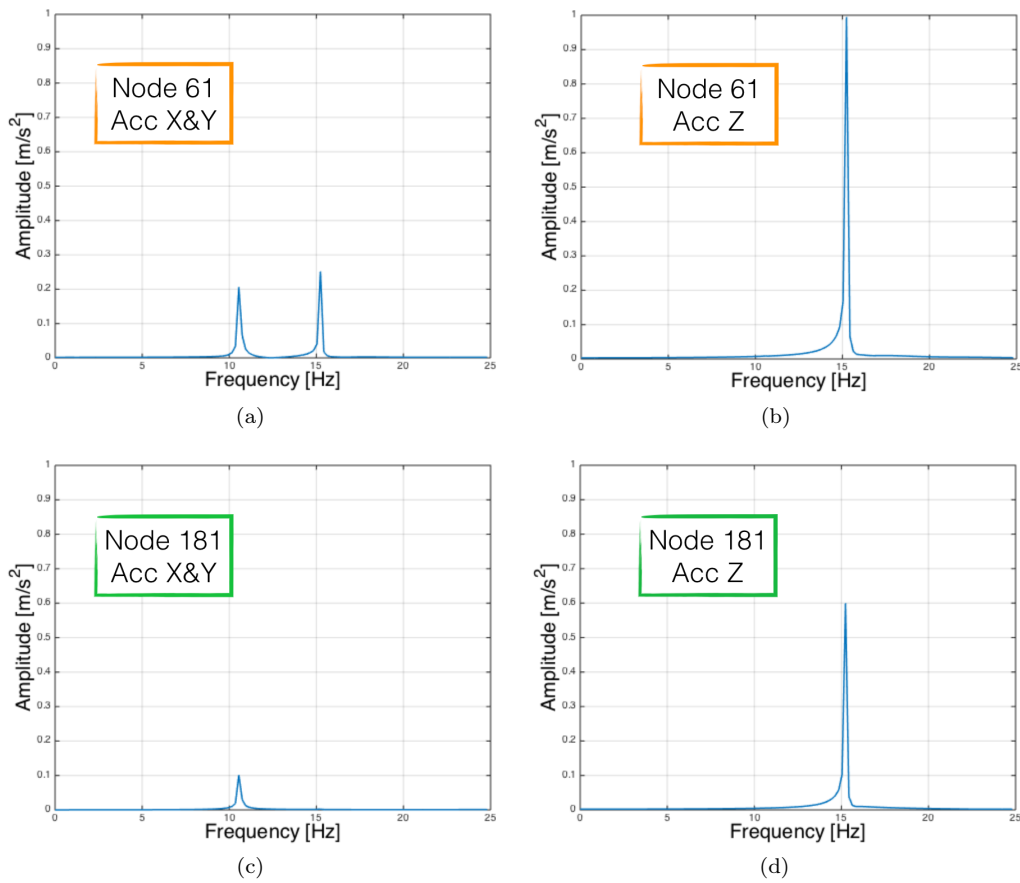

Figure 6.6: FFTs of the horizontal and vertical accelerations of two nodes of the shell with positive Gaussian curvature (node 61 is not R-Funicular, node 181 is R-Funicular)

The correlation between R-Funicularity and frequencies of the horizontal acceleration has been observed for all nodes and is represented in Figure 6.7. In the diagram the distribution of the 15 Hz frequency (the frequency of the vertical mode) in the FFTs of the X, Y and Z accelerations is represented. The amplitude on the Y axis has been normalized dividing by the maximum amplitude value observed.
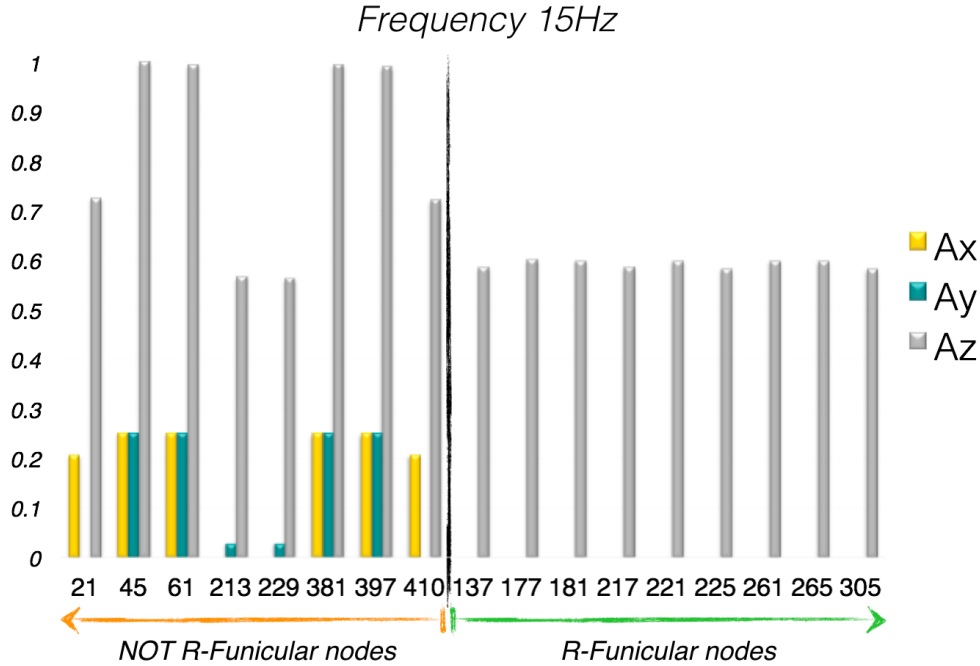

Figure 6.7: Distribution of 15 Hz frequency in the X, Y and Z acceleration FFTs of the shell with positive Gaussian curvature

6.4.2   Case study 2 - Shell with negative Gaussian curvature

Phase 1 - Modal Funicularity

The second shell analyzed is a form-found vault with positive and negative Gaussian curvature. The shell surface shown in Figure 6.8 has been obtained starting from a flat square mesh 20×20 m, supported at its four corners. Unlike the shell shape discussed in Subsection 6.4.1, diagonal elements have been added to the mesh used to perform the form finding procedure, as shown on the top right of Figure 6.8a. These elements increase the shell's stiffness and significantly alter its final shape. The shape of the vault obtained has curvatures with opposite sign and lower height. A quadrangular diagonal mesh shown in Figure 6.8b has been applied to the numerical model used in the FE analyses.

A modal analysis has been performed applying a thickness equal to 6 cm. The number of modes to be selected in order to have a participating mass larger than 90% in all three directions (X, Y and Z) is 57 modes. However a larger number equal to 300 modes has been adopted to ensure convergence of the results in the forced analyses performed in phase 2. In Table 6.5 the eigenmodes with the more significant participating mass in the X, Y and Z directions are shown.

The R-Funicularity Ellipse Method is applied to the stress distribution related to the eigenmodes in order to calculate the eccentricity in every node of the shell and verify the condition of R-Funicularity of the eigenmodes, or the so-called Modal Funicularity.
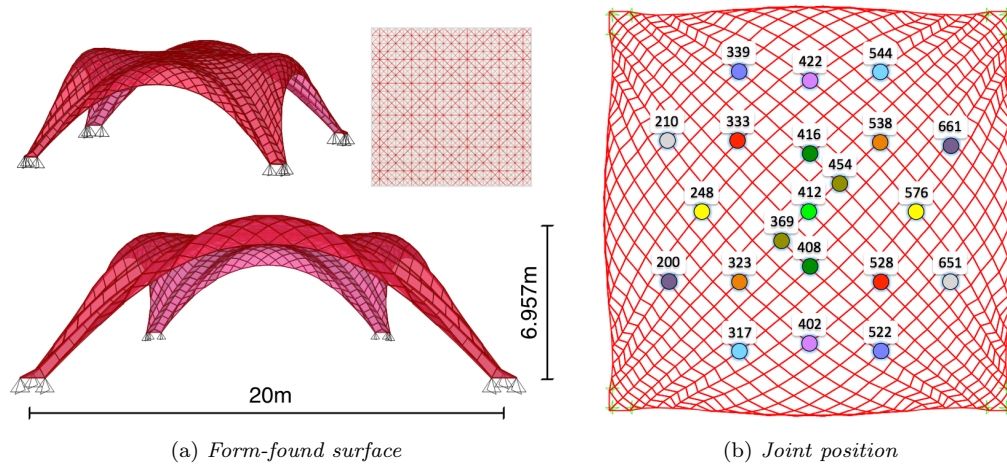
(a) *Form-found surface*

(b) *Joint position*

Figure 6.8: Shells with negative Gaussian curvature

		Shell with Negative Gaussian Curvature					
Step	**Frequency**		**Modal Participating Mass Ratios**				
	[Hz]	**UX**	**UY**	**UZ**	**SumUX**	**SumUy**	**SumUZ**
Mode 1	3.5760	**0.347**	0.194	0	0.347	0.194	0
Mode 2	3.5763	0.194	**0.347**	0	0.541	0.541	0.901
Mode 29	22.375	0	0	**0.884**	0.630	0.630	0.416
Mode 56	34.906	0.025	0.001	0	0.913	0.888	0.937
Mode 57	34.908	0.001	0.025	0	0.914	0.914	0.937

Table 6.5: Results of modal analysis performed on the shell shown in Fig. 6.8 (6 *cm* thick)

The results obtained for the modes with larger participating mass in X, Y and Z directions (i.e. Mode 1, 2 and 29 with participating mass in bold in Table 6.5) are indicated in Figure 6.9. As observed in Subection 6.4.1, the mode with the larger participating mass in Z direction (i.e. Mode 29) is the more funicular and is the one with a modal shape that less diverges from the form-found shape.
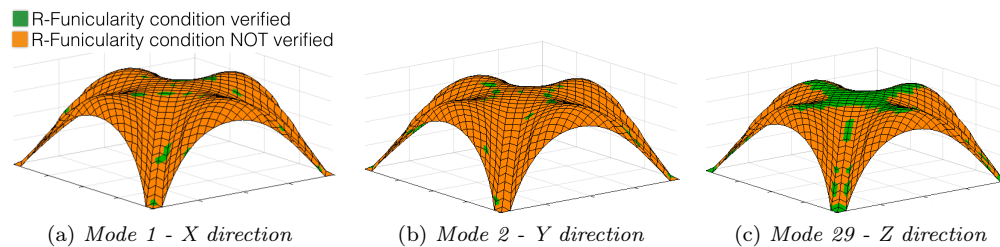

(a) *Mode 1 - X direction*

(b) *Mode 2 - Y direction*

(c) *Mode 29 - Z direction*

Figure 6.9: Modal Funicularity of the 6 *cm* thick shell shown in Fig. 6.8

Phase 2 - Dynamic Funicularity

Following the phase 1, the same steps of phase 2 discussed in Section 6.4.1 are carried out. Three periodic functions are defined according to the first three modes that have a significant participating mass. As indicated in Table 6.5, these modes are mode 1 and 2 for the X and Y direction respectively and mode 29 for the Z direction. Then a time-history analysis with multiple frequencies spectrum is performed exciting both horizontal and vertical modes and taking into account a 5% damping.

To evaluate the shell response to each component of the applied dynamic load and to convert the results from time-domain to frequency-domain functions, the FFT is applied to the accelerations in X, Y and Z direction of the nodes of the shell. Results are presented focusing on the shell behavior in a number of areas, indicated by the nodes shown in Figure 6.10, differentiating between R-Funicular nodes (if located in the area of the shell where the R-Funicularity condition is verified) and not R-Funicular nodes.

In the diagram shown in Figure 6.11, the distribution of the 22 Hz frequency (the frequency of the vertical mode) in the FFTs of the X, Y and Z accelerations are shown. The amplitude of the FFTs represented by the Y axis has been normalized dividing by the maximum amplitude value observed.
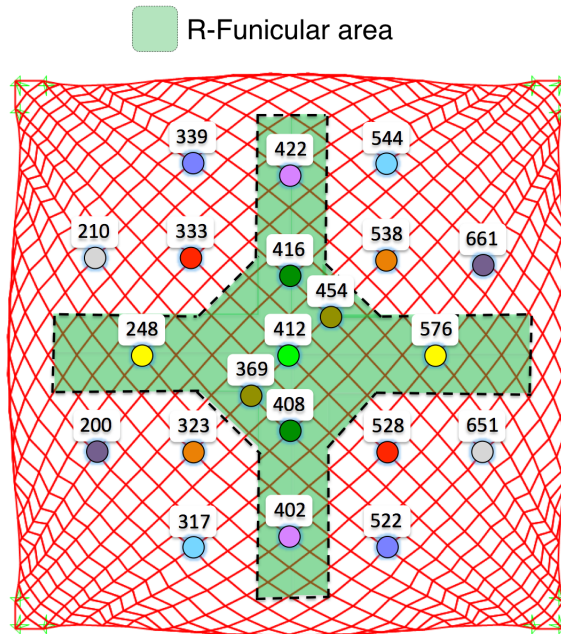
Figure 6.10: Joint position and R-Funicular area of the shell with negative Gaussian curvature

Although the difference between R-Funicular and not R-Funicular nodes is less pronounced with respect to the results obtained in Subsection 6.4.1, a similar trend can still be observed. All not R-Funicular nodes show a horizontal acceleration in X and Y direction in correspondence with a frequency equal to 22 Hz, while the R-Funicular nodes do not show such a horizontal acceleration or, if they do, the amplitude observed is much smaller.

Figure 6.11: Distribution of 22 Hz frequency in the X, Y and Z acceleration FFTs of the shell with negative Gaussian curvature

6.4.3 Earthquake response of the shell with positive Gaussian curvature

In Subections 6.4.1 and 6.4.2, the application of the proposed methodology to two different form-found shell shapes highlights how the observati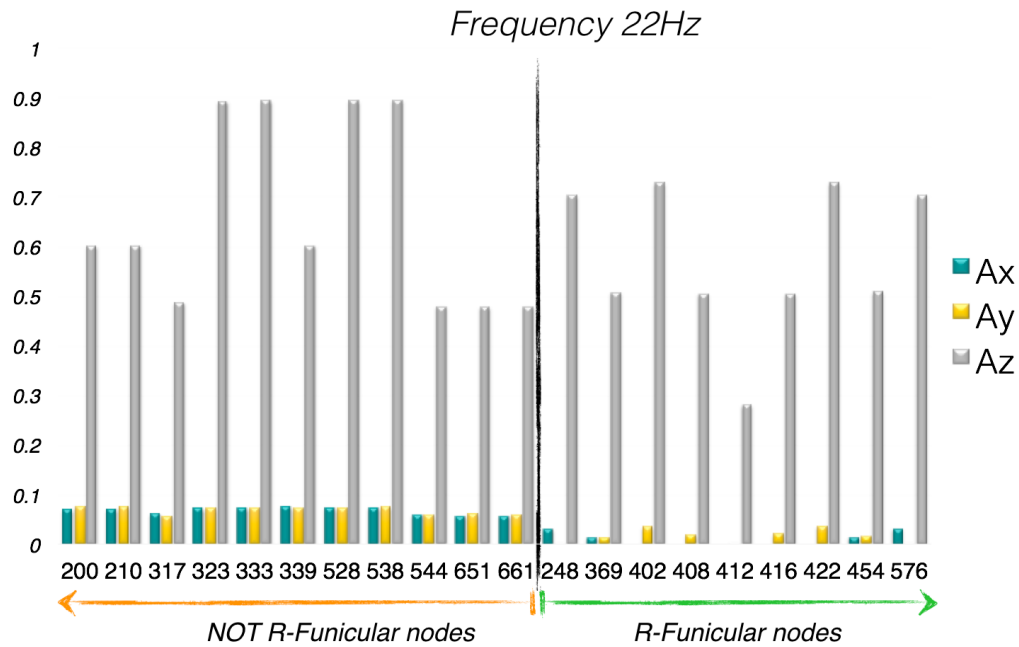on of the frequency content of the different areas of the surface can give insight on the shell's funicular behavior. Time-history analyses have been performed applying ad hoc functions able to excite specific frequency values. In this section the results obtained from a time-history analysis under the action of a real seismic event are reported and discussed.

In Subections 6.4.1 and 6.4.2, it was demonstrated that the mode exciting larger mass in vertical direction is the more funicular. This aspect of the Modal Funicularity becomes important in a real-world case. For example after the L'Aquila Earthquake (Italy, 2009), in fact in that case the vertical components of the seismic loads were exceptionally high and intense [45]. For this reason, this particular earthquake event has been chosen to perform an analysis of the 6 cm thick shell with positive Gaussian curvature presented in Subsection 6.4.1.

The three-component accelerometric waveforms of the earthquake can be found in ITACA (ITalian ACelerometric Archive, beta version), the Italian strong motion database and are represented in Figure 6.12.

The three waveform components have been combined in a linear time-history analysis. The choice of considering only the elastic range overlooking the constitutive behavior of the material is simplified but consistent with the analysis performed in Subsection 6.4.1 and with the aim to focus on the evaluation of the behavior of shell shapes.

The Relaxed Funicularity Ellipse Method has been applied to the results obtained from the time-history analysis and the evolution of the Dynamic Funicularity along the time has been observed. The extension of the funicular area changes at every step together with the dynamic input applied.
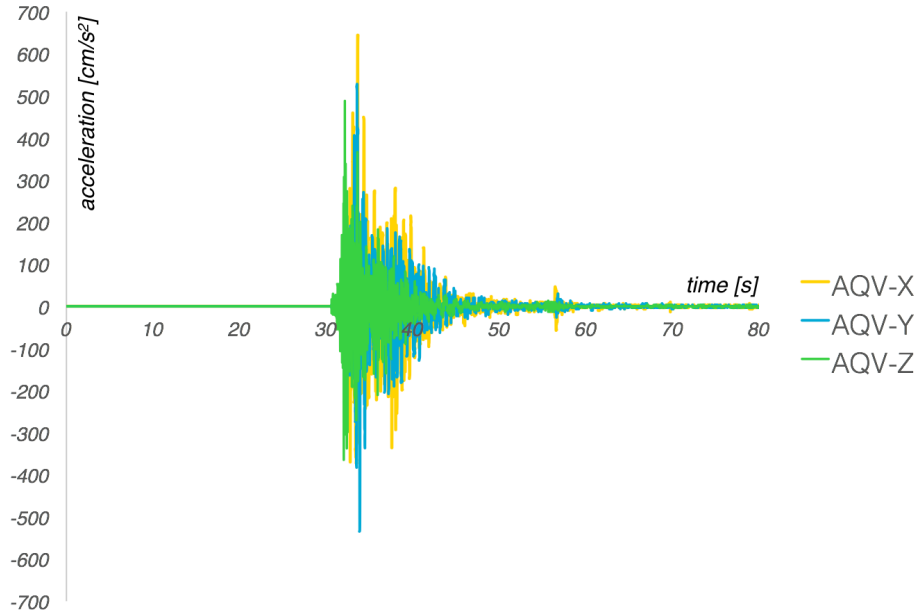
Figure 6.12: Horizontal and vertical accelerometric waveforms of the L'Aquila Earthquake Italy 2009 (ITACA)

As shown in Figure 6.13, the maximum extension of the funicular area is similar to the result of the Modal Funicularity obtained for the mode in Z direction indicated in Figure 6.3c. Differences can be observed close to the boundaries, but the nodes analyzed stayed in the R-Funicular or not R-Funicular area defined in Figure 6.5.
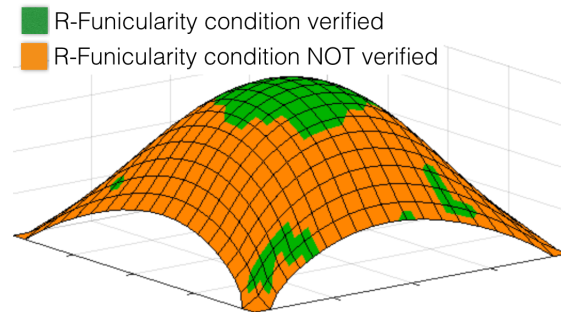
Figure 6.13: Dynamic Funicularity under L'Aquila earthquake (Italy) of the 6 cm thick shell shown in Fig. 6.2

Looking at the frequency content, performing the FFTs of the horizontal and vertical accelerations of the nodes of the shell, peaks in correspondence of the frequencies of the principal modes can be observed (around 10 Hz for the modes in X and Y directions and around 15 Hz for the mode in Z direction). It is important to highlight that these results have been obtained under a real seismic event characterized by a broad range of frequency values.

Moreover in the FFT of the horizontal accelerations, the R-Funicular nodes show an amplitude in correspondence of 15 Hz lower than the one of the non R-Funicular nodes. This tendency is less accentuated but still consistent with the observations made in Subsection

6.4.1 (see Fig. 6.14: node 61 and 181 are indicated as example). Hence a relationship between the results of the real-case study and the ones obtained from the application of the two-phased methodology may be highlighted.
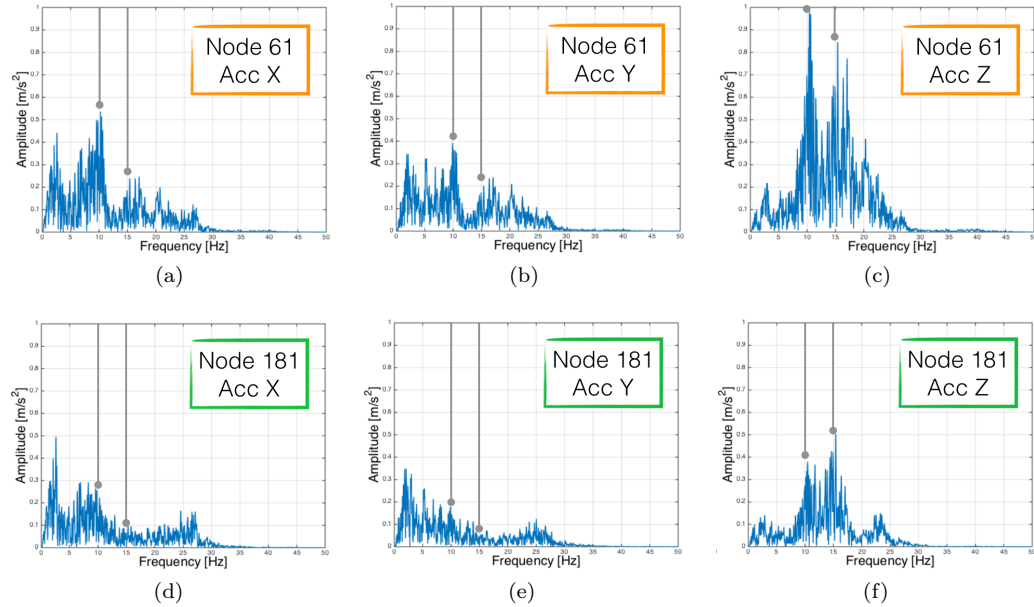
Figure 6.14: FFTs of the horizontal and vertical accelerations of two nodes of the shell with positive Gaussian curvature under L'Aquila earthquake (node 61 is not R-Funicular, node 181 is R-Funicular)

As explained in Section 6.1, the shape of shell structures are usually designed to achieve funicularity, but due to the oscillating nature of the modes, during a seismic event, the Dynamic Funicularity could reveal itself in dramatic reversed traction components. Hence the new methodology proposed can help to identify the vulnerable area of a shell form-found under gravity loading when it is subject to a seismic event.

Chapter 7

r-Fun

The Relaxed Funicularity Ellipse Method illustrated in Chapter 5 has been introduced to quantify the funicularity of a shell structure. The method has been implemented in a Matlab-based software environment integrated with a Finite Element analysis package. The proposed software is named r-Fun. The system environment and architecture are presented in Section 7.1. Section 7.2 shows the results obtained applying r-Fun to a form-found shell.

7.1 System architecture and FE software interaction

The Relaxed Funicularity Ellipse Method has been developed to evaluate the R-Funicularity of a shell structure and return a graphical feedback of the results. To allow a quick and accessible application of the method, a new software has been implemented. The principal objective is to provide an easy-to-use tool that simplifies the implementation of the steps illustrated in Chapter 5.

The algorithm of the proposed software environment named r-Fun is developed in Matlab [67]. r-Fun is able to "communicate" with the commercial software SAP2000 using the analysis results of a shell structure analyzed in the FE software package.

The Application Programming Interface (API) of SAP2000 is used to provide access during run-time, between the third-party application (i.e. Matlab) and the analysis software itself [23]. The API is activated within the Matlab script (.m file) in order to gain access to an extensive collection of objects and functions. Hence the operations of SAP2000 are entirely controlled in the background, completely overriding the standard point-and-click procedure.

The overall system architecture is illustrated in Figure 7.1.

As explained in Chapter 5, the calculation of the values of the internal forces (N and M) is preliminary to the application of the RF-Ellipse Method. The FE software SAP2000 is employed for this purpose. The shell surface can be modeled directly in SAP2000, or imported in the software using a graphic image format (typically .dxf or .igs). The boundary conditions, section properties and acting loads may be defined. Finally the shell structure is analyzed to compute the values of internal forces under the given load case or load combination.

Successively, the RF-Ellipse Method can be applied. From this point, the user is expected to interact entirely with r-Fun, while SAP2000 runs silently in the background of the operating system's desktop. The analysis flow is controlled through an interactive Graphical user interface (GUI), which consists of a main window that contains all the components necessary to define and review the analysis procedure.
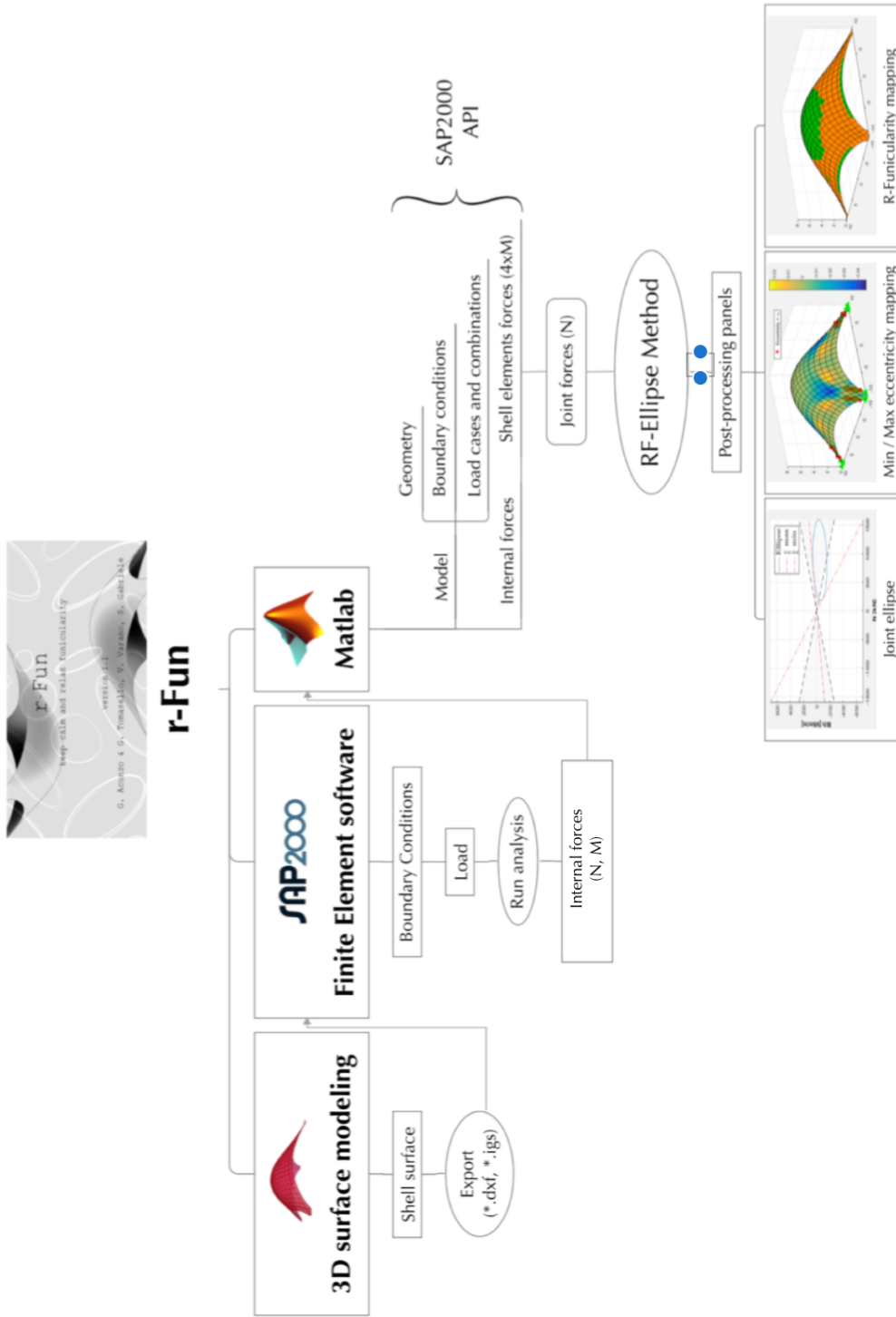
83

Figure 7.1: r-Fun System architecture

7.2 Software results and application to a case study

The operation of r-Fun and the results that can be visualized are detailed applying the proposed software to a case study. The shell with positive Gaussian curvature introduced in Chapters 5 and 6 has been analyzed with the support of r-Fun. The related GUI is shown in Figure 7.5.

The "Settings" pane is located on the left. Clicking on "Import load cases/combos", the load cases or combinations defined in SAP2000 are displayed. r-Fun is able to apply the RF-Ellipse Method to shells analyzed performing linear static, modal or time-history analyses. Following the case studies seen in Chapters 5 and 6, the Relaxed Funicularity, Modal Funicularity and Dynamic Funicularity can be studied using the proposed software environment. In Figure 7.2, the "Settings" panes for a static analysis (Dead Load case) and a modal analysis (Modal - Mode 2 Load case) are compared.
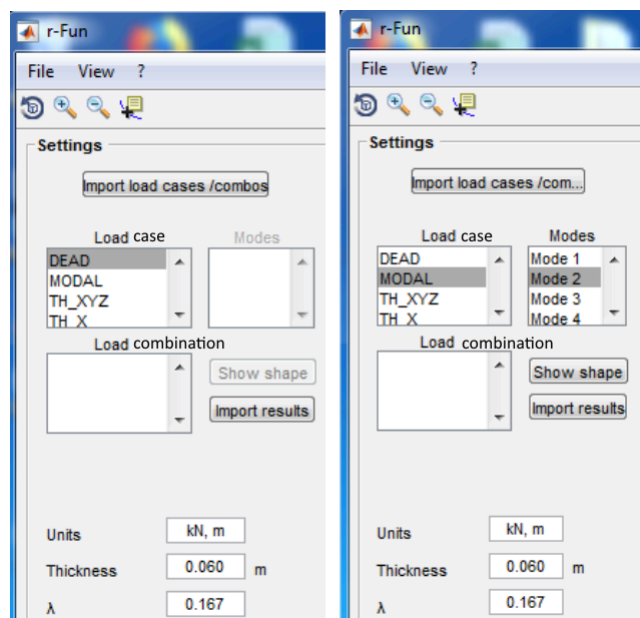

Figure 7.2: r-Fun Settings pane

In Figure 7.3, the "Settings" pane for a time-history analysis (TH XYZ load case) is shown; the time steps to include can be defined by the user.

Once selected the load case or combination desired, the user can click "Import results". In the first pane (top left), the surface geometry with the applied constraints is visualized. In the "Settings" pane, the units and the shell thickness are shown; this information is acquired from the FE software. The admissibility coefficient λ (refer to Section 5.2) is set equal to $1/6$ by default but can be adjusted by the user.

The RF-Ellipse Method is implemented acquiring the values of the internal forces from SAP2000. For every node of the surface, the FE software returns as many values of the selected internal force as the total number of the shell elements connected to the node. An average value for each node is calculated in r-Fun.

Selecting a single node (or multiple nodes) on the shell surface, the RF-ellipse or ellipses are shown in the second pane (bottom left) (Fig. 7.4). In the third pane (top right), a mapping of the minimum or maximum eccentricities is shown. In the last pane (bottom right), r-Fun shows a mapping of the shell areas where the R-Funicularity condition is or is not verified (green and orange areas respectively).
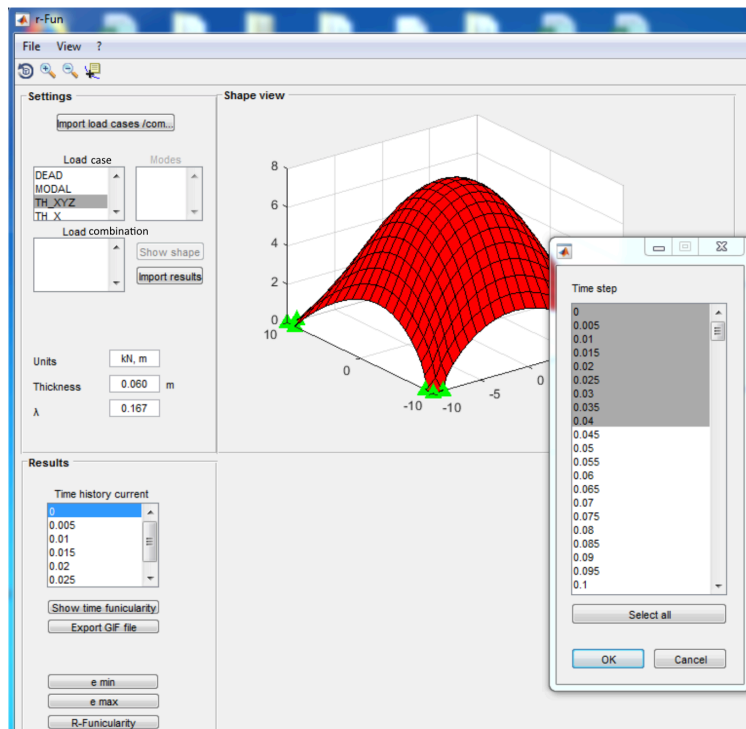
Figure 7.3: r-Fun Time-history analysis settings pane

If a time-history analysis is selected, the evolution of the Dynamic Funicularity along the time can be visualized in the last pane and exported in a bitmap image format (.GIF).
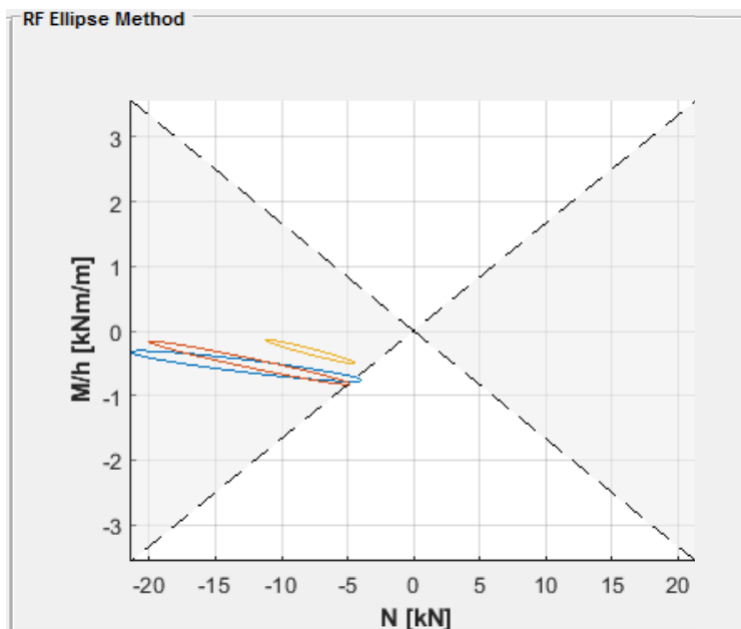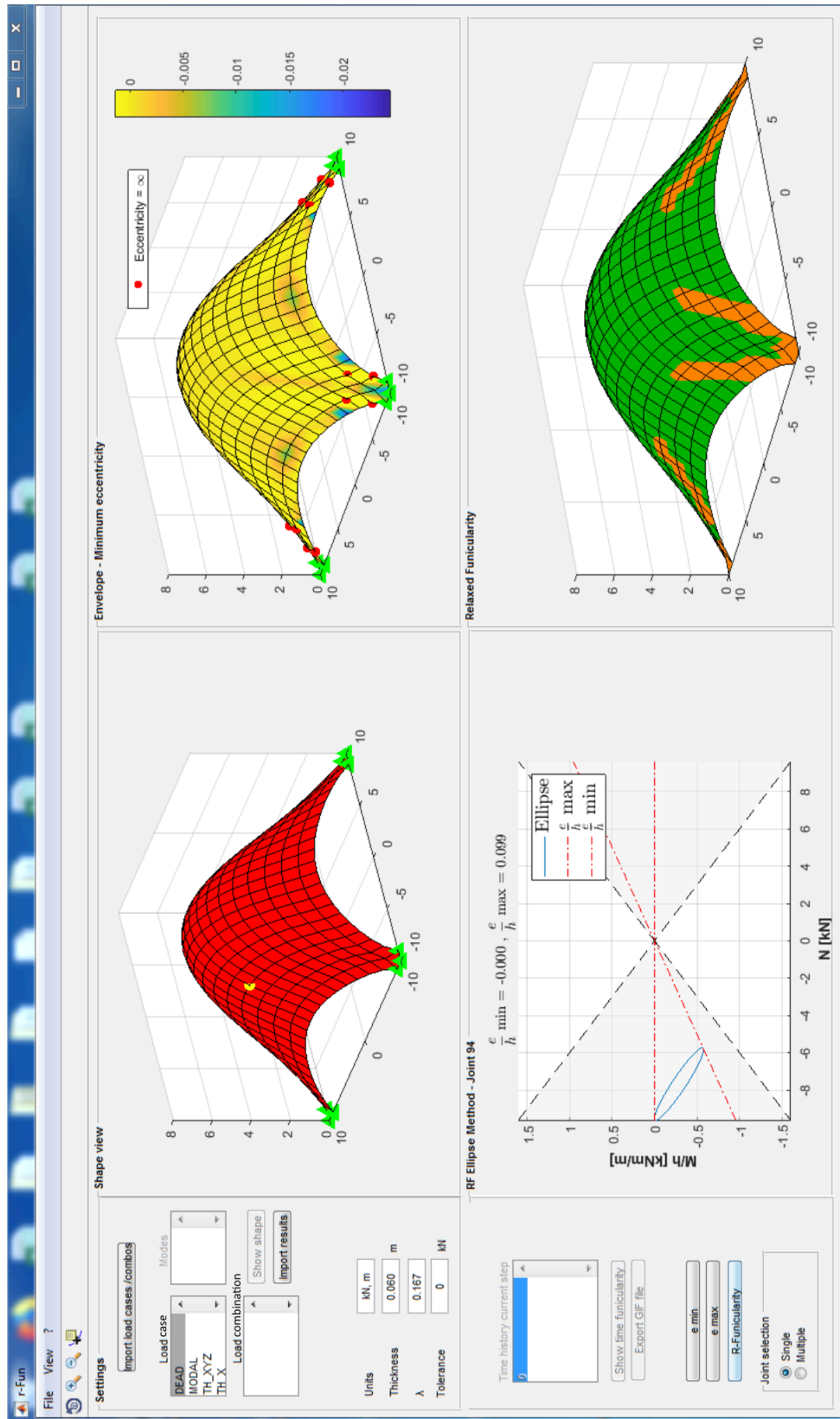

Figure 7.4: r-Fun RF-ellipses

Figure 7.5: r-Fun Graphical user interface and results

Chapter 8

Conclusions

The final chapter intends to draw conclusions. Section 8.1 summarizes the key contributions of the study undertaken in this dissertation. Section 8.2 is devoted to analyze the limitations of the developed approaches and present directions for future work.

8.1 Contributions

> "Shells play a special, singular role for engineers. Their shape directly derives from their flow of forces, and defines their load-bearing behaviour and lightness, saving material by creating local employment, their social aspect." (J. Schlaich, 2014) [1]

When designing shell structures, architects and engineers have the opportunity to create eye-catching complex forms exploring many different solutions. The choice of an appropriate shape is fundamental for designing efficient structures pursuing the criterion of minimization of the material used. Due to multiple design constraints, the objective to achieve an ideal membrane behavior cannot be always satisfied. An ideal funicular behavior is only valid under two assumptions: the boundary conditions are congruent with the given shape and loading, and the ratio between membrane stiffness and flexural stiffness tends to infinity. When this is not the case and bending moments cannot be avoided, it is crucial to quantify the funicularity. In fact this information can help the designer to review and select the most appropriate shell shape to adopt.

This dissertation gives a contribution in this direction introducing the concept of Relaxed Funicularity and the related R-Funicularity Ellipse Method. The classical definition of funicularity is extended to 2D structures with the support of a proper mathematical formulation. The new method is employed to quantify whether a shell is more or less funicular using a generalized definition of the eccentricity that is computed in every point of the given surface as the ratio between bending moment M and normal force N acting along a specific direction.

The generalized eccentricity has the graphical representation of an ellipse in the (N, M) plane, here called RF-ellipse. It has been stated that if, for every node of the shell, the RF-ellipse is included in fixed admissibility limits, then the shell can be considered R-Funicular.

The proposed method has been validated applying it to different case studies. The first one is represented by a catenary vault, while the second example is represented by a synclastic shell structure. A parametric analysis of the latter vault has been performed, varying thickness, loading and boundary conditions. Some interesting observations have been illustrated. When the applied loads are those used in the form finding process, the thinner the shell the more it is R-Funicular. On the contrary, when the load condition changes (e.g. horizontal load

added), increasing the shell thickness improves the shell R-Funicularity. Furthermore when the loading and the boundary conditions are both different from those used in the form finding process, increasing the shell thickness improves the shell R-Funicularity.

During the shell form finding process, gravity loads are considered, while the role of horizontal loading is ignored. Today shells with complex geometries are being designed and built, and are used to shelter people during extreme events such as earthquakes, but the dynamic behavior of civil thin shells has always been subjected to limited research. This dissertation investigates the effects of dynamic loading on the behavior of civil thin shells form-found under gravity loads.

A two-phased methodology to study the dynamic behavior of shell structures is presented. The R-Funicularity Ellipse Method is applied to results obtained from modal analysis and time-history analyses of a form-found shell and the Modal and Dynamic Funicularity are compared.

Time-history analyses have been performed applying ad hoc functions able to excite specific frequency values. More specifically the dynamic forces generated and applied are chosen to highlight how the behavior in the forced analysis is related to the results of the modal analysis.

Two case studies of axisymmetric shells with positive and negative Gaussian curvature form-found under self-weight are presented to explain how observations of the frequency content might offer insights into funicularity of shells under dynamic loading.

In addition the first shell presented has been analyzed under the action of a real seismic event. Since the modes exciting larger mass in vertical direction are the more funicular, the L'Aquila Earthquake (Italy, 2009) characterized by high vertical component has been selected. The R-Funicularity Ellipse Method is applied using the internal forces of the L'Aquila time-history analysis and how the results of the real-case study are related to the ones obtained from the application of the two-phased methodology proposed is highlighted.

Due to the oscillating nature of any seismic event, the R-Funicular area of the shell could reveal itself in reversed traction components and become a vulnerable area of the shell. Hence the presented two-phased methodology could be implemented to evaluate the behavior of a shell form under dynamic loading, to select the better performing option between all feasible considered shapes and, even more, to review the form-found shape in order to have an improved performance not only under gravity loading but also under dynamic loading.

Finally, a new software named r-Fun has been implemented to allow a quick and accessible application of the RF-Ellipse Method and consequently of the proposed two-phased methodology. The algorithm of the proposed software is developed in Matlab and is able to "communicate" with the commercial software SAP2000 using the so-called Application Programming Interface (API) of SAP2000. An interactive graphical user interface has been developed. The operation of r-Fun and the results that may be compute by the user are detailed applying the software to a case study.

8.2   Future research

There are many opportunities to apply the Relaxed Funicularity Ellipse Method and the presented two-phased methodology that studies the dynamic behavior of shell structures, making further contributions to the specific topics of this dissertations. This section describes potential areas for research exploration that extend the work presented.

Firstly, the RF-Ellipse Method could be applied to explore the structural performance of difference shell shapes under multiple boundary and loading conditions. It could be equally employed to study free-form, mathematical or form-found geometries of new or existing shells offering insights into their structural efficiency.

The case studies illustrated in this dissertation are represented by continuous form-found surfaces. However the proposed method could be applied to shells made of discrete elements, in other words to gridshells.

Furthermore the definition of Relaxed Funicularity can be used as objective function to perform structural shape optimization. This approach may represent the most challenging and interesting future application of the method. Different design solutions may be explored with an iterative approach. In fact following the application of one of the form finding technique presented, an initial shell shape is obtained. The geometry can then be adjusted and refined to verify the R-Funicular condition in every node of the shell under multiple design constraints.

Moreover, with reference to the dynamic and seismic behavior of shell structures, further investigations on different shell shapes can be undertaken applying the proposed two-phase methodology. When performing the time-history analyses, different spectra can be considered defining ad hoc functions or applying the accelerometric waveforms of various seismic events. The performance under earthquakes with high and low vertical components can be examined.

In conclusion, this dissertation presents a new approach to study the behavior of form-found shells. The idea inspiring this study is that, when designing a structure, the structural performance should always be taken into consideration from the early design stages. The developed approach is not meant to be an end result, but may open debate about the potential of form-found shapes and funicularity evaluation in the contemporary building practice. Such debate can be even more fruitful if located at the *intersection* between architecture and structural engineering.

Bibliography

[1] Adriaenssens S., Block P., Veenendaal D., Williams C., Shells structures for architecture: form finding and optimization, Routledge, London, 2014.

[2] Adriaenssens S., Gabriele S., Varano V., Tomasello G., Magrone P., Revisiting the form finding techniques of Sergio Musmeci: the bridge over the Basento river, in ICSA2016 Portugal, Structures and Architecture Beyond their limits, Taylor&Francis Group, London, 2016.

[3] Allemang R.J., The Modal Assurance Criterion (MAC): Twenty years of Use and Abuse, Sound & Vibration, 37(8), 14-21, 2003.

[4] Anderson S., Eladio Dieste: innovation in structural art, Princeton Architectural Press, New York, 2004.

[5] Arnold R.N., Warburton G.B., Flexural vibrations of the walls of thin cylindrical shells having freely supported ends, Proceedings of the Royal Society of London, Mathematical and Physical Sciences, 197(1049), 238-256, 1949.

[6] Belluzzi O., Scienza delle costruzioni, Zanichelli, Bologna, 1982.

[7] Billington D. P., Thin Shell Concrete Structures, McGraw Hill, New York, 1982.

[8] Bletzinger K. U., Ramm E., Form finding of shells by structural optimization, Engineering with Computers, 9, 27- 35, 1993.

[9] Bletzinger K.U., Wüchner R., Daoud F., Camprubí N., Computational methods for form finding and optimization of shells and membranes, Computer methods in applied mechanics and engineering, 194, 3438-3452, 2005.

[10] Block P., Thrust network analysis, Ph.D. dissertation, Department of Architecture, Massachusetts Institute of Technology, 2009.

[11] Block P., DeJong M., Ochsendorf J., As Hangs the Flexible Line: Equilibrium of Masonry Arches, Nexus Network Journal, 8(2), 9-19, 2006.

[12] Block P., Ochsendorf J., Thrust network analysis: a new methodology for three-dimensional equilibrium, Journal of the international association for shell and spatial structures, 48(3), 1-8, 2007.

[13] Bradshaw R., Campbell D., Gargari M., Mirmiran A., Tripeny P., Special Structures: Past, Present, and Future, Journal of Structural Engineering, 691-709, 2002.

[14] Calladine C.R., Theory of shell structures, Cambridge University Press, New York, 1983.

[15] Capanna A., Sergio Musmeci, Biographical Dictionary of Italy, 77, 2012.

[16] Capanna A., Sergio Musmeci's forms with no name and anti-polyhedrons, Journal of Applied Mathematics, V(I), 31-35, 2012.

[17] Capomolla R., Il ponte sul Basento, ovvero l'invenzione di una forma ancora senza nome, Casabella, 739-740, 12-19, 2006.

[18] Capomolla R., Structure and form: the theory of Minimal Surfaces and the bridge over the Basento River by Sergio Musmeci, Docomomo Journal, 45, 46-51, 2011.

[19] Chilton J., Form finding and fabric forming in the work of Heinz Isler, Proceedings of the Second International Conference of Flexible Formwork, University of Bath, UK, 84-91, 2012.

[20] Chopra A.K., Dynamic of structures: Theory and applications to earthquake engineering, 5th Edition, Pearson Education, 2017.

[21] Clough R.W., Penzien J., Dynamic of structures, Computer & Structures, Inc., Berkeley, California, 2003.

[22] Computer & Structures, Inc., SAP2000 Version 18, Analysis Reference Manual, Berkeley, California, 2016.

[23] Computer & Structures, Inc., SAP2000 Version 18, API Documentation, Berkeley, California.

[24] Conversano E., Francaviglia M., Lorenzi M.G., Tedeschini Lalli L., Persistence of form in art and architecture: catenaries, helicoids and sinusoids. Aplimat Journal of Applied Mathematics, 101-112, IV, 2011.

[25] Crane K., Discrete differential geometry: an applied introduction, Notes of a course at the California Institute of Technology (Caltech), Pasadena, CA, 2013 (Last updated 2018).

[26] Culmann K., Die graphische Statik, Meyer und Zeller, Zurich, 1866.

[27] Day A.S., An introduction to Dynamic Relaxation, The Engineer, 219, 1965.

[28] De Honnecourt, V., Album de dessins et croquis, Bibliothèque nationale de France, Paris, 1300.

[29] De Wolf C., Low Carbon Pathways for Structural Design: Embodied Life Cycle Impacts of Building Structures, Ph.D. dissertation, Department of Architecture, Massachusetts Institute of Technology, 2017.

[30] De Wolf C., Pomponi F., Moncaster A., Measuring embodied carbon dioxide equivalent of buildings: A review and critique of current industry practice, Energy and Buildings, 140, 68-80, 2017.

[31] Ebner F., Volte e cupole, Published by the Author, Rome, Italy, 2011.

[32] Gabriele S., Adriaenssens S., Varano V., Tomasello G., Alfonsi D., Modal Funicularity of form-found shell structures, in Proceedings of the International Association for Shell and Spatial Structures (IASS) symposium 2017: Interfaces, Hamburg, Germany, September 25-28, 2017.

[33] Gabriele S., Varano V., Tomasello G., Alfonsi D., R-Funicularity of form-found shell structures, Engineering Structures, 157, 157-69, 2018.

[34] Galasso D., Villard de Honnecourt: La rivoluzione strutturale del medioevo, ArchigraficA, 2008.

[35] Galilei G., Discorsi e dimostrazioni matematiche intorno a due nuove scienze attenenti alla meccanica e i movimenti locali (Discourses and Mathematical Demonstrations Relating to Two New Sciences), In Leida: Appresso gli Elsevirii, 1638.

[36] Gauss K.F., General investigations of curved surfaces, Presented to the Royal Society of London, 1827, translated by Morehead J.C., Hiltebeitel A.M., The Princeton University Library, 1902.

[37] Giovannardi F., Sergio Musmeci Strutture fuori dal coro, Giovannardierontini, 2010.

[38] Glancey J., Genius expressed in nuts and bolts: Peter Rice is an engineer revered by the world's top architects, Indipendent, UK, 1992.

[39] Green A.E., Zerna W., Theoretical Elasticity, Oxford University Press, UK, 1968.

[40] Gregory D., Catenaria, Philosophical Transaction of the Royal Society of London, 19, 637-652, 1697.

[41] Guidi M., Fregolent A., Ruta G., Curvature effects on the eigenproperties of axisymmetric thin shells, Thin-Walled Structures, 119, 224-34, 2017.

[42] Haber R.B., Abel J.F., Initial equilibrium solution methods for cable reinforced membranes, Part I - Formulations, Computer Methods in Applied Mechanics and Engineering, 30, 263-284, 1982.

[43] Heyman J., Poleni's problem, Proceedings of the Institution of Civil Engineers, 84(1), 737-759, 1988.

[44] Heyman J., The stone skeleton, Cambridge University Press, 1997.

[45] Indirli M., Kouris L., Formisano A., Borg R.P., Mazzolani F.M., Seismic Damage Assessment of Unreinforced Masonry Structures After The Abruzzo 2009 Earthquake: The Case Study of the Historical Centers of L'Aquila and Castelvecchio Subequo, International Journal of Architectural Heritage, 7(5), 536-578, 2012.

[46] Ingold L., Rinke M., Sergio Musmeci's search for new forms of concrete structures, in Proceedings of the 5th International Congress on Construction History, Chicago, Illinois, 2015.

[47] Iori T., Poretti S., SIXXI 2 Storia dell'ingegneria strutturale in Italia, Gangemi, Rome, 2015.

[48] Iori T., Poretti S., The Golden Age of Italian Style Engineering, Proceedings of the Third International Congress on Construction History, Cottbus, 2009.

[49] Intergovernmental Panel on Climate Change, Sources of CO2: IPCC Special Report on Carbon Dioxide Capture and Storage, 2005.

[50] Jiashen F., Lei F., Closed form solution for non-linear dynamic response in shallow shells, Applied Mathematical Modelling, 73, 416-424, 1991.

[51] Kawaguchi K., A report on large roof structures damaged by the great Hanshin-Awaji Earthquake, International Journal of Space Structures, 12, 135-147, 1997.

[52] Kilian A., Ochsendorf J., Particle-spring system for structural form finding, Journal-international association for shell and spatial structures 148(77) 30, 2005.

[53] Kraus H., Thin Elastic Shells: An introduction to the theoretical foundations and the analysis of their static and dynamic behavior, John Wiley & Sons, Inc., New York, 1967.

[54] Kunieda H., Earthquake response of roof shells, International Journal of Space Structures, 12, 149-159, 1997.

[55] Kurrer K., The History of the Theory of Structures: From Arch Analysis to Computational Mechanics, Ernst&Sohn, Berlin, 2008.

[56] Lambert S., Italy and the history of preventative conservation, Conservation, Exposition, Restauration D'Objects D'Art EGG-2010-Horizons, 2010.

[57] Lancaster L. C., Concrete Vaulted Construction in Imperial Rome: Innovations in Context, Cambridge University Press, Cambridge, UK, 2005.

[58] Leissa A.W., Vibration of shells, NASA SP-288, U.S. Government Printing Office, 1973.

[59] Leissa A.W., Kadi A.S., Curvature Effects on Shallow Shell Vibrations, Journal of Sound and Vibration, 16(2), 173-187, 1971.

[60] Leissa A.W., Qatu M.S., Vibration of continuous systems, McGraw Hill, USA, 2011.

[61] Lenci S., Consolini L., Percorsi per un metodo progettuale tra forma e struttura, ARACNE editrice S.r.l., Roma, 2007.

[62] Liew K.M., Vibration of doubly-curved shallow shells, Acta Mechanica, 114, 95-119, 1996.

[63] Lucchesi M., Padovani C., Pasquinelli G., Zani N., Masonry constructions: mechanical models and numerical applications, Springer, 2008.

[64] Lucchesi M., Padovani C., Pasquinelli G., Zani N., The maximum modulus eccentricities surface for masonry vaults and limit analysis, Mathematics and Mechanics of Solids, 4, 71-87, 1999.

[65] Marino E., Salvatori L., Orlando M., Borri C., Two shape parametrizations for structural optimization of triangular shells, Computer and Structures, 166, 1-10, 2015.

[66] Marmo F., Rosati L., Reformulation and extension of the thrust network analysis, Computers and Structures, 182, 104-118, 2018.

[67] Mathworks, Inc., MATLAB: The language of technical computing, Natick, Massachusetts, USA.

[68] Meyer C., Sheer M.H., Do concrete shells deserve another look?, Concrete International, 43-50, 2005.

[69] Michiels T., Form finding of arches and shell structures subjected to seismic loading, Ph.D. dissertation, Department of Civil and Environmental Engineering, Princeton University, 2018.

[70] Michiels T., Adriaenssens S., Form finding algorithm for masonry arches subjected to in-plane earthquake loading Computers and Structures, 195, 85-98, 2018.

[71] Michiels T., Adriaenssens S., Identification of key design parameters for earthquake resistance of reinforced concrete shell structures, Engineering Structures, 153, 411-420, 2017.

[72] Mikhasev G.I., Free and parametric vibrations of cylindrical shells under static and periodic axial loads, Technische Mechanik, 17(3), 209-216, 1997.

[73] Moghaddam H.A., Seismic Behaviour of Space Structures, International Journal of Space Structures, 15, 2, 119-135, 2000

[74] Musmeci P., email correspondence.

[75] Musmeci S., La statica e le strutture, Cremonese, Rome, 1971.

[76] Musmeci S., Ponte sul Basento a Potenza. L'Industria Italiana del Cemento (2), 77-98, 1977.

[77] Musmeci S., Struttura ed architettura. L'Industria Italiana del Cemento, 10, 771-786, 1980.

[78] Nervi P.L., Scienza o arte del costruire? Caratteristiche e possibilità del cemento armato, Città Studi Edizioni, New Edition, 2014.

[79] Nordenson G. (editor), Seven Structural Engineers: The Felix Candela Lectures, The Museum of Modern Art, New York, 2008.

[80] Ochsendorf J., Guastavino vaulting: the art of structural tile, Princeton architectural press, New York, 2010.

[81] Odifreddi P., Una parabola sulle catene, Le scienze, 573, 18, 2016.

[82] O'Neill B., Elementary Differential Geometry, Revised Second Ed., Elsevier, Inc., 2006.

[83] Oppenheim A.V., Schafer R.W., Discrete-time signal processing, Pearson Higher Education, Inc., NJ, USA, 2010.

[84] Ostovari-Dailamani S., Behavior of cylindrical and doubly-curved shell roofs under earthquake, Ph.D. dissertation, Department of Civil Environmental and Geomatic Engineering, University College London, 2010.

[85] Pedreschi R., The engineer's contribution to contemporary architecture: Eladio Dieste, Thomas Telford Ltd, 2000.

[86] Petrizzi C., Sergio Musmeci a Potenza: Il ponte e la città, Basilicata Regione Notizie, 17-24.

[87] Pizzetti G., Zorgno Trisciuoglio A.M., Principi statici e forme strutturali, UTET, Torino, 1980.

[88] Qatu M.S., Recent research advances in the dynamic behavior of shells: 1989-2000, Part 1: Laminated composite shells, Applied Mechanics Reviews, 55(7), 2002.

[89] Qatu M.S., Recent research advances in the dynamic behavior of shells: 1989-2000, Part 2: Homogeneus shells, Applied Mechanics Reviews, 55, 415-434, 2002.

[90] Qatu M.S., Vibration of doubly-curved shallow shells with arbitrary boundaries, Applied Acoustics, 15, 21-27, 2012.

[91] Reitherman R., The Aesthetics of Structures, Consortium of Universites for Research on the Engineered Environment (CUREE), Richmond, California, 2015.

[92] Rice P., An engineer Imagines, Batsford, London, 1994, Reissue 2017.

[93] Rippmann M., Funicular Shell Design: Geometric approaches to form finding and fabrication of discrete funicular structures, Ph.D. dissertation, Institute of Technology in Architecture, ETH Zurich, 2016.

[94] Saggio A., I Nervi di Morandi o le reti di Musmeci, Domus 815-116, 1999.

[95] Saka T., Taniguchi Y., Damage to spatial structures by the 1995 Hyogoken-Nanbu Earthquake in Japan, International Journal of Space Structures, 12, 125-133, 1997.

[96] Schek H.J., The force density method for form finding and computation of general networks, Computer methods in applied mechanics and engineering, 3, 115-134, 1974.

[97] South A., Zweifel C., Disaster Survivability of Thin-Shell Concrete Dome Structures: Experience and Practice, presented at the IASS-SLTE 2014 symposium, Shells, Membranes and Spatial Structures: Footprints, 2014.

[98] De Souza V.C., Croll J.G., Free vibrations of orthotropic spherical shells, Engineering Structures, 3(2), 71-84, 1981.

[99] Spinelli L., When infrastructure becomes landscape, Domus, 2007.

[100] Stevin S., De Beghinselen der Weeghconst (1586), In The Principal Works of Simon Stevin, vol. 1, Leyden, 1955.

[101] Tedeschi A., AAD Algorithms-Aided Design. Parametric strategies using Grasshopper, Le Penseur, Italy, 2014.

[102] Tedesko A., Shells 1970 - History and outlook, American Concrete Institute, 28, 1-14, 1971.

[103] Todisco L., Funicularity and Equilibrium for High-Performance Conceptual Structural Design, PhD Dissertation, Technical University of Madrid, 2016.

[104] Todisco L., Corres Peiretti H., Mueller C.T., Funicularity through External Post-tensioning: Design Philosophy and Computational Tool, Journal of Structural Engineering, 142(2), 2015.

[105] Tomasello G., Gabriele S., Adriaenssens S., R-Funicularity of shell structures under dynamic load: the influence of the shape, in Proceedings of the International Association for Shell and Spatial Structures (IASS) symposium 2018: Creativity in Structural Design, MIT, Boston, USA, July 16-20, 2018.

[106] Trovalusci P., Tinelli A., The recovery of the ethic of constructions: P. L. Nervi vs. S. Musmeci, Two structural conceptions compared, Structures and Architecture: Concepts, Applications and Challenges, Cruz (ed.), Taylor & Francis group, 261-267, 2013.

[107] Varignon P., Nouvelle mécanique ou statique, Tome 1, Jombert, Paris, 1725.

[108] Veenendaal D., Block P., An overview and comparison of structural form finding methods for general networks, International Journal of Solid Structures, 49, 3741-3753, 2012.

[109] Vitruvius Pollio M., De architectura (On architecture, published as Ten Books on Architecture), ca. 15 BC.

[110] Vrachliotis G. (editor), Frei Otto. Thinking by modelling, Spector Books, Leipzig, 2016.

[111] Weingardt R.G., Anton Tedesko: Father of Thin-Shell Concrete Construction in America, Structure Magazine, 69-71, 2007